Partial-interaction behaviour of composite steel-concrete bridge beams subjected to fatigue loading

by

Rudolf Seracino
B.A.Sc. (Hons, Toronto), M.A.Sc. (Toronto)

submitted to the Department of Civil and Environmental Engineering
at The University of Adelaide
for the degree of
Doctor of Philosophy

October, 1999

PONTEM PERPETUI MANSURUM IN SAECULA

Gaius Julius Lacer, 98 AD

“I have left a bridge that shall remain forever”

This is an inscription on a bridge over the river Tagus in Spain.

The bridge, consisting of six arches, is still in use,
and carries 183 m of roadway 53 m above the river.

Statement of Originality

This work contains no material which has been accepted for the award of any other degree or diploma in any university or tertiary institution and, to the best of my knowledge and belief, contains no material previously published or written by another person, except where due reference has been made in the text.

I give consent to this copy of my thesis, when deposited in the University Library, being available for loan and photocopying.

Signature: ______________________ Date: 13/10/99

Publications

The following papers have been published, or have been submitted for publication, as a result of this research project.

Accepted for publication in refereed journals

Oehlers, D.J., Seracino, R. and Yeo, M.F. "Effect of friction on the shear connection in composite bridge beams." Accepted for publication to the *Journal of Bridge Engineering*, ASCE, 1999.

Oehlers, D.J., Seracino, R. and Yeo, M.F. "Fatigue behaviour of composite steel and concrete beams with stud shear connectors." Accepted for publication to *Progress in Structural Engineering and Materials*, 1998.

Submitted to refereed journals

Seracino, R., Oehlers, D.J. and Yeo, M.F. "Partial-interaction in composite bridge beams. Part 1: Generic model and shear flow." Submitted to the *Journal of Bridge Engineering*, ASCE.

Seracino, R., Oehlers, D.J. and Yeo, M.F. "Partial-interaction in composite bridge beams. Part 2: Flexural stresses and application." Submitted to the *Journal of Bridge Engineering*, ASCE.

Discussions in refereed journals

Seracino, R. and Oehlers, D.J. (1999) Discussion to "Fatigue of welded stud shear connectors in steel-concrete-steel sandwich beams." *Journal of Constructional Steel Research*, 49(3), 315-316.

Oehlers, D.J. and Seracino, R. (1998) Discussion to "Low-cycle fatigue test on stud shear connectors." *Journal of Structural Engineering*, ASCE, 124(5), 599-600.

Refereed conference papers

Seracino, R., Oehlers, D.J. and Yeo, M.F. "Reverse-cycle testing of stud shear connectors." *Proceedings of the 16th Australasian Conference on the Mechanics of Structures and Materials*, Sydney, Australia, December 8-10, 1999.

Seracino, R., Oehlers, D.J. and Yeo, M.F. "The effect of friction on the longitudinal shear force distribution along the steel-concrete interface of composite bridge beams." *The 6th East Asia-Pacific Conference on Structural Engineering and Construction*, Taipei, Taiwan, January 14-16, 1998.

Seracino, R., Oehlers, D.J. and Yeo, M.F. "Beneficial effect of friction on the fatigue life of shear connectors." *Proceedings of the 15th Australasian Conference on the Mechanics of Structures and Materials*, Melbourne, Australia, December 8-10, 1997.

ACKNOWLEDGMENTS

First and foremost, I wish to extend my gratitude to my supervisors, Dr. D.J. Oehlers and Dr. M.F. Yeo. Their genuine interest in both the research project and my future is sincerely appreciated and made my work enjoyable.

I thank the Laboratory staff in the Department of Civil and Environmental Engineering at the University of Adelaide for all of their interest and assistance with the experimental component of the project. In particular, I wish to acknowledge the help of Messrs. Gregory Atkins and Jeffrey Hiorns. Thanks also go out to Mr. Bruce Lucas for his invaluable assistance with setting up the data acquisition system and Dr. Stephen Carr for providing computing assistance throughout the course of this project. The experimental work was, in part, funded by a Small Australian Research Council grant, for which I am grateful for as the experimental component of the research would not have been possible. The departmental administrative staff was also very patient and helpful when dealing with my many questions and requests, especially Mrs. Bernice Golledge and Ms. Diane Keable.

Thanks are also due to the following people who have in one way or another influenced my research: Dr. Matthew Burnet, and Messrs. M.S. Ali and Lieping Yuan.

Finally, I would like to thank my wife Joanne and step-daughters Kate and Jessica for their patients during the many stressful times encountered during the course of the project.

ABSTRACT

Most composite steel-concrete bridges are designed using full-interaction which assumes that the shear connection is infinitely stiff. The purpose of this research was to determine the effect of partial-interaction and interfacial friction on the fatigue behaviour of composite bridge beams. This has led to the development of a set of design rules for the assessment of the residual strength and performance of composite bridge beams.

A finite element computer model has been developed that allows for partial-interaction by incorporating the complex load-slip characteristics of the stud shear connectors and the frictional resistance along the interface under reverse-cyclic loading. Parametric studies showed that partial-interaction reduces the shear flow such that the connectors have a fatigue life longer than originally anticipated, however, the flexural stresses increase which has an adverse effect on the endurances of the steel and concrete components. Analyses also showed that friction affected the shear flow over the entire length of the beams even though the frictional forces are concentrated locally around the load points and supports.

Previous research has shown that partial-interaction theory is very complicated and is not suitable for direct application in design. Hence, simple mathematical models have been developed to predict the partial-interaction shear flow and partial-interaction flexural stresses directly from full-interaction analyses. These models can be used to give accurate predictions of the fatigue endurance and strength from standard full-interaction analyses.

A new type of push test for reverse-cycle fatigue loads has been developed from which the fatigue load-slip characteristics of shear connectors can be predicted for use in computer simulations. The experimental investigation has shown that for a given range of load, connectors subjected to reverse-cyclic loads last longer than connectors subjected to uni-directional cyclic loads, and has proven that current design techniques are safe as the design life is longer than anticipated. These tests also showed that the increase in slip per cycle is constant over about 3/4 of the design life after which the slip increases rapidly and, if monitored, can be used to directly predict the end of the life of a structure.

TABLE OF CONTENTS

LIST OF FIGURES

LIST OF TABLES

NOTATION

The following notation is used in this thesis. Generally, only one meaning is assigned to each symbol however, when more than one definition is possible, the correct one will be evident from the context in which it is used.

$\{\ \}$ = vector

$[\ ]$ = matrix

A = cross-sectional area of the component; residual strength constant; regression coefficient

A_{sh} = shank cross-sectional area of a stud shear connector

B = probability of occurrence for each type of fatigue vehicle; regression coefficient; strain matrix

b = width

bf = bottom flange when used as a subscript

C = constant in endurance equation; function of the composite cross-sectional stiffness and geometry (Newmark, Siess and Viest 1951); integration constant

c = concrete component or constant when used as a subscript

D = material stiffness matrix

d_c = distance between the centroids of the steel and concrete components

d_{sh} = diameter of the shank of a stud shear connector

ds/dN = rate of change in slip per cycle

ds/dx = slip strain

E = modulus of elasticity; endurance

E_a = asymptotic endurance

$(E_{au})_{avg}$ = average uni-directional asymptotic endurance

E_{mean} = mean endurance

E_{sp} = longitudinal shear spring stiffness

e = eccentricity

FIA = Full-interaction Analysis

F_C = compressive force

F_f = force constant

F_T = tensile force

F_{fr} = frictional resistance

f = frequency of a range in a shear flow influence line diagram; frictional force required for equilibrium

f_c = concrete cylinder compressive strength

fi = full-interaction when used as a subscript

fp = focal point when used as a subscript

f_t = concrete tensile strength

f_u = tensile strength of a stud shear connector

g = gradual when used as a subscript

h = depth of the component

I = moment of inertia

I_{nc} = moment of inertia of the transformed concrete section

K = integration constants; global stiffness matrix

K_{cy} = cyclic stiffness of stud shear connectors

K_f = secant stiffness due to friction alone

K_{sec} = secant stiffness of a stud shear connector alone

K_{st} = initial static stiffness of stud shear connectors

K_t = total horizontal connection stiffness

k = connector shear stiffness

k_{el} = four-noded element stiffness matrix

k_{sp} = spring element stiffness matrix

k_t = foundation modulus (Adekola 1968)

L = length of a simply supported beam

LVDT = Linear Variable Displacement Transducer

L_f = load constant

L_{sp} = length of a shear span

l = distance of the concentrated load from the left support; length of shear span

l_c = distance from support where RF_R becomes constant

M = bending moment

MF_ϕ = curvature multiplication factor

m = exponent in endurance equation; mid-span when used as a subscript

N = number of cycles; axial force; normal force across the interface

N^* = number of cycles prior to overload

N_{exp} = number of cycles to cause fatigue failure experimentally

N_r = number of cycles when slip begins to increase rapidly

n = modular ratio; number of connectors to fail as a group

P = concentrated load; peak uni-directional shear flow force

PIA = Partial-interaction Analysis

PIFP = Partial-interaction Focal Point

P_{max} = peak applied load

P_r = residual strength of a stud shear connector

P_{st} = initial static strength of a stud shear connector

p = connector spacing

pi = partial-interaction when used as a subscript

Q = total longitudinal shear force

Q_o = static shear flow strength required

Q_{of} = shear flow strength at the start of the fatigue life

Q_{res} = residual strength of the shear connection in an existing structure

Q_{st} = shear flow strength at the start of the fatigue life

q = total longitudinal shear force per unit length; quarter-span when used as a subscript

q_{dowel} = longitudinal shear force per unit length resisted by shear connectors

q_L = shear force per unit length to the left of the concentrated load (Newmark, Siess and Viest 1951)

q^* = shear flow force

R = total range of cyclic load resisted by the shear connectors; global load vector

RF_P = reduction factor for the peak uni-directional shear flow force

RF_R = reduction factor for the total range

R_u = magnitude of the range in the positive branch of a cycle

r = vertical force across the interface; rapid when used as a subscript

S = stress
SFV = Standard Fatigue Vehicle
S_r = stress range
s = slip; steel component or support when used as a subscript
s_g = slip used to define $[ds/dN]_g$
s_i = initial slip
s_r = slip where slip begins to increase rapidly
s_u = ultimate slip at static failure
T = number of vehicles traversing a bridge; tensile force acting across the interface (Adekola 1968); transpose of a matrix
t = thickness
tf = top flange when used as a subscript
u = distance to the load from the left support (Newmark, Siess and Viest 1951); local nodal displacement in global x-direction
V = vertical shear force
V^* = vertical shear force acting at x
v = local nodal displacement in global y-direction
W = weight of a fatigue vehicle as a proportion of the SFV
w = width; web when used as a subscript
X = a parameter in the endurance equation
x = distance of the cross-section from the left support
y = distance between the centroids of the concrete component and the transformed concrete section of the composite beam; vertical deflection (Adekola 1968); distance measured from steel-concrete interface
$\bar{y}$ = centroid of component with respect to the steel-concrete interface
$\bar{y}_{nc}$ = centroid of the transformed concrete section with respect to the steel-concrete interface
z = number of cyclic range magnitudes; distance between the centroids of the steel and concrete components (Newmark, Siess and Viest 1951)

α = factor grouping together geometry, material properties, and connection stiffness

β = factor grouping together geometry, material properties, and connection stiffness

δ = displacement

δQ = resultant bearing force acting on a stud shear connector

ε = normal strain

ϕ = curvature

γ = shear strain

μ = coefficient of friction

σ = normal stress

τ = shear stress

υ = Poisson's ratio

Chapter 1

Introduction

1.1 EARLY HISTORY OF COMPOSITE STEEL-CONCRETE BEAMS

Probably the first time the term *composite beam* was recorded was in a report by the Dominion Bridge Company of Canada in 1922 that presented the results of tests on two floor panels, each of which contained two steel I-sections encased in concrete. The excerpt, which is taken from a paper written by Viest on a review of research on composite steel-concrete beams (Viest 1960), is as follows:

> "...While such beams have hitherto been designed on the assumption that the entire load ... is carried by the steel, it was thought that the steel and concrete might really act together so as to form a composite beam ..."

At about the same time, similar tests were being undertaken in the United States and the United Kingdom, and tests on composite steel-concrete beams have been carried out ever since.

The early tests were all on steel sections encased in concrete such that the entire interaction was a result of the bond between the steel and concrete. In the 1930s, researchers were beginning to realize that unless the steel sections were fully encased in concrete and there was no fluctuation in load, bond alone could not be relied upon to provide the interaction required and, hence, the first forms of mechanical shear connectors were used.

The first tests in Switzerland in 1933 used spiral connectors made by forming round bars into a helix and used what are now commonly referred to as push-out specimens. European researchers then moved from spirals to hooks or loops in the early 1940s that were made by bending reinforcing bars. While European practice tended towards using stiff connectors, American researchers preferred using more flexible connectors requiring less fabrication.

The first extensive tests undertaken in the United States, commencing in 1942 at the University of Illinois and Lehigh University, used flexible angle and channel connectors, which showed that flexible connectors are also suitable to provide adequate shear connection. The first test using stud shear connectors, which are the common form of shear connection today, took place in 1954.

As the experimental tests showed that slip is inherent in composite steel-concrete beams, several theories considering slip on stresses and deflections were being developed. The first theory was developed in 1951 by Newmark, Siess and Viest and remains the basis for most partial-interaction theory today.

1.2 PURPOSE OF THE RESEARCH

The cross-section of a typical composite steel-concrete bridge beam is shown in Fig. 1.1 where a series of parallel, longitudinal, steel I-sections, support a concrete deck, which acts as the running surface. The two components are mechanically fastened together along the steel-concrete interface with a distribution of stud shear connectors that are welded to the top of the steel flange and embedded in the concrete. The shear connection makes the steel and concrete components act as one improving the efficiency of the cross-section. These types of bridges are commonly used today as they are a competitive design option for both simply supported and continuous spans ranging from 20 to 100 meters (Hayward 1987).

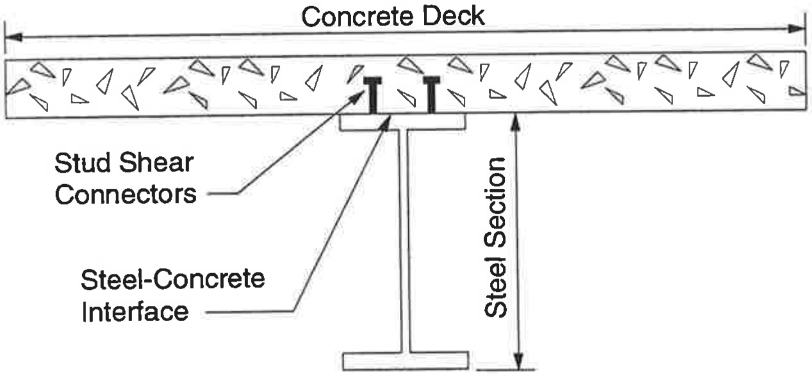

Figure 1.1: Typical composite steel-concrete bridge beam cross-section.

The aim of this research project was to investigate the partial-interaction behavior of composite steel-concrete bridge beams subjected to fatigue loading so that the remaining strength and remaining endurance of these structures can be more accurately predicted. Current design/assessment procedures assume that the shear connection is infinitely stiff so that there is no relative displacement of the components along the interface that is slip. This results in a continuous strain distribution throughout the depth of the section, as shown in Fig. 1.2a, which simplifies the design/assessment procedure. However, the connectors are not infinitely stiff and slip along the interface occurs as vertical vehicle loads are applied, which is known as partial-interaction. Consequently, the strain distribution at a section is discontinuous at the interface level as shown in Fig. 1.2b, where the magnitude of the discontinuity is a measure of the slip, known as the slip strain.

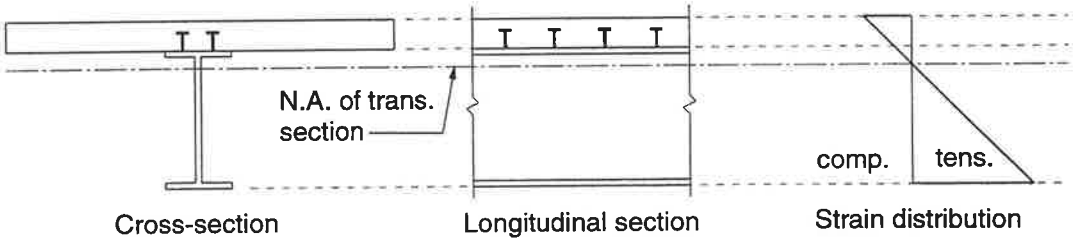

a) Full-interaction

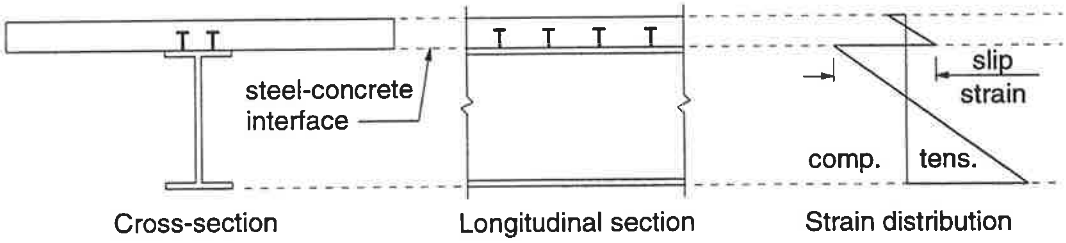

b) Partial-interaction

Figure 1.2: Full- and partial-interaction strain distributions.

Hence, partial-interaction affects all aspects of composite steel-concrete bridge beams and the following two points were focused on in this research:

1) the reduction in the longitudinal shear force along the steel-concrete interface, which influences the fatigue life of the shear connection; and
2) the increase in the flexural stresses in the steel and concrete components that are required in order to maintain equilibrium.

In addition to the two points listed above, the complex interaction between friction along the steel-concrete interface and the non-linear load-slip behavior of the stud shear connectors was also investigated. Finally, an experimental programme was undertaken to investigate the fatigue behavior of stud shear connectors subjected to reverse-cyclic loading. As it will be shown in Chapter 2, very little work has been done in this area, even though the shear connection is subjected to reverse loading in most regions of the span.

The need for improved and reliable assessment techniques becomes clear when one realizes that in the United States, for example, there are approximately 600,000 bridges, and on average, 12,000 of them reach their 50 year design life every year (Yazdani and Albrecht 1987). Furthermore, it has long been stated that general replacement of bridges after a life of about 100 years is impractical and that complete replacement could not be achieved in less than a century (Ogle 1981). The need for reliable assessment techniques in composite steel-concrete bridges is even more critical as the condition of the shear connection can, in general, not be visually inspected.

1.3 DISPOSITION OF THESIS

The thesis is divided in to 6 chapters and the contents of each chapter are summarized in the following section. It is noted that the models developed pertain to simply supported composite beams assuming unpropped construction. The implication of this being that the composite beam resists the live load due to traversal of vehicles, while the steel section on its own resists the dead load of the concrete component.

Chapter 2 is the literature review and contains all of the information that the remainder of the thesis references.

The third chapter develops the linear partial-interaction models, where simple techniques based on common full-interaction analysis are derived to predict the partial-interaction range resisted by the shear connection and the partial-interaction flexural stresses. An example is solved to show the use of the techniques developed by solving an illustrative problem.

Chapter 4 deals with the non-linear behavior of the shear connection when the complex interaction between friction along the interface and the non-linear load-slip behavior of the stud shear connectors are considered. A finite element procedure is developed that can model the non-linear behavior and a comparison is made between the results of the computer simulations and a simple hand analysis technique.

Chapter 5 deals with the experimental programme that was undertaken as part of this research project. The details of the specimens are given as well as the experimental data and an analysis of the results is made.

Finally, Chapter 6 summarizes the conclusions that have been drawn from this research and suggestions are given for future research in the area, which have been identified but time has restricted from pursuing.

Chapter 2

Literature Review

2.1 INTRODUCTION

This chapter presents all of the information that is referenced in the remainder of the thesis. The classical partial-interaction theory is discussed first, as it forms the basis for this research. The current analysis and assessment techniques are then described, followed by a review of research directions, primarily pertaining to experimental investigations. Finally, details of the core finite element program that was used to perform the computer simulations are given.

2.2 CLASSICAL PARTIAL-INTERACTION THEORY

The first partial-interaction theory, or incomplete-interaction as it was then called, was developed in 1943 by Newmark, Siess and Viest (1951) after carrying out a series of tests on small-scale composite T-beams at the University of Illinois. Channel connectors were used at the time, and it was stated that no rational means of predicting the stiffness of the connectors exists, hence, the stiffness was determined experimentally by measuring the slip. Since then, however, relationships have been developed, as discussed in Section 2.5, that can predict the stiffness of the most common form of shear connection that is stud shear connectors. Slip measurements on large-scale composite T-beams showed that for simply supported beams with a uniform distribution of shear connectors, the slip near a concentrated load is very nearly zero and increases towards the support. It was suggested that the low values of slip near the loads are, in part, a result of the increased friction along the steel-concrete interface. Consequently, Newmark, Siess and Viest were the first to acknowledge the presence of friction, however, results of this research (Chapter 4) suggest that although the frictional forces are high in the vicinity of concentrated loads, the effect on the horizontal shear is distributed over the full length of the beam.

The classical theory that was developed, which remains the foundation for most of the partial-interaction theory used today, is based on the following four assumptions.

1. The shear connection is continuous and uniform along the length of the beam, which is a reasonable assumption to make particularly when dealing with simply supported beams.
2. The slip is directly proportional to the shear load, which simply means that the connector stiffness is constant. This was a valid assumption to make as it was demonstrated that for the loads used in the tests, the load-slip relationship was linear.
3. The distribution of strain is linear throughout the depth of each component of the section, which is consistent with beam theory where it is stated that plane sections remain plane.
4. The concrete slab and steel beam deflect the same amount at all points along the beam at all times, which implies that the curvature in both components is the same. This is a valid assumption as long as there is no separation of the components along the steel-concrete interface. As stud shear connectors have heads that are designed to resist uplift forces, it is reasonable to assume that there is no separation along the interface, especially under serviceability fatigue loading.

The theory was developed for a simply supported beam with a single concentrated load acting anywhere along the beam, and relationships were explicitly derived to predict the following properties at any section: axial force acting on the steel and concrete components; horizontal shear force acting along the steel-concrete interface; slip, which is the horizontal shear force multiplied by the stiffness of the shear connection; strain distribution in the steel and concrete; and deflection. The derivation of the equations as given by Newmark, Siess and Viest will not be reproduced here. Instead, the derivation presented by Johnson

(Johnson 1994), which is also based on the work by Newmark et al and was used in the development of this research, is summarized in Section 2.2.1. However, for comparison with the model developed as part of this research in Chapter 3, the expression given by Newmark et al to predict the horizontal shear force for the portion of the beam to the left of the concentrated load is

$$q_L = \frac{\overline{EA}z}{\overline{EI}}P\left\{\left(1-\frac{u}{L}\right)-\frac{\sinh\left[\frac{\pi}{\sqrt{C}}\left(1-\frac{u}{L}\right)\right]}{\sinh\left(\frac{\pi}{\sqrt{C}}\right)}\cosh\left(\frac{\pi}{\sqrt{C}}\frac{x}{L}\right)\right\} \tag{2.1}$$

where q_L is the shear force per unit length along the interface to the left of the concentrated load, the parameters $\overline{EA}$, $\overline{EI}$ and C are functions of the composite cross-sectional stiffness and geometry of the beam, z is the distance between the centroids of the steel and concrete components, P is the concentrated load, u is the distance to the load from the left support, L is the length of the simply supported beam and x is the distance of the cross-section from the left support.

As a result of the investigation carried out by Newmark et al, it was concluded that the slip is negligible for a properly designed composite beam and, hence, assuming full-interaction is satisfactory. Based on this conclusion and the obvious complexity of the partial-interaction equations (Eq. 2.1 for example), partial-interaction theory was never embraced in the design of new or the assessment of existing composite beams. It is noted, however, that the significance of the range of load on the fatigue life of shear connectors was not realized at the time when partial-interaction theory was first being developed. Up until the mid 1950s, when the first cyclic tests were carried out (Sinclair 1956), only static tests were performed and, hence, it was not determined that even a small change in the longitudinal shear force due to slip would have a significant effect on the fatigue life of the shear connection as is shown in Chapter 3.

2.2.1 Development of linear-elastic partial-interaction theory

As it is crucial to the understanding of the models developed in this research project, the linear-elastic partial-interaction theory that was presented by Johnson (Johnson 1994) is reworked in detail in this section.

2.2.1.1 *Parameters*

Figures 2.1 and 2.2 define the basic variables used in the derivation of the model. The location of the concentrated load P and the design point are given by l and x respectively in Fig. 2.1 where the origin is defined at the left support. The total length of the beam is given by L and p is the connector spacing. As shown in Fig. 2.2, the depths of the steel and concrete components are given by h_s and h_c respectively, and d_c is the distance between the centroid of the steel component and the centroid of the concrete component.

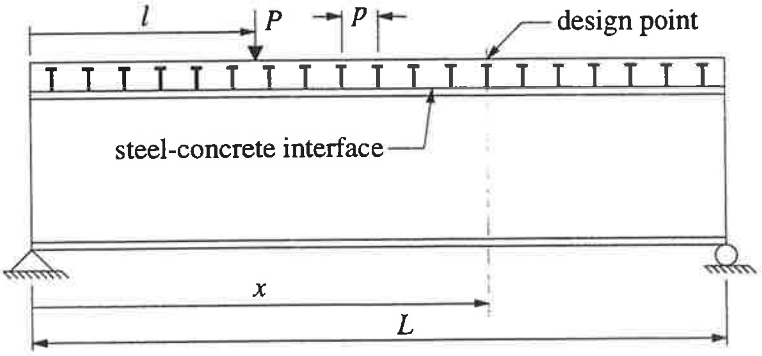

Figure 2.1: Longitudinal section of theoretical composite beam.

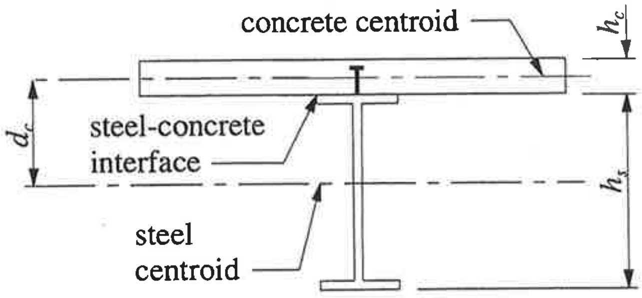

Figure 2.2: Cross-section of theoretical composite beam.

Figure 2.3 shows the forces acting on a small length of the beam *dx* located at a design point *x* from the left support. The steel and concrete components are separated to show the forces acting along the steel-concrete interface, and the deformation is greatly exaggerated for clarity. The stress resultants *M*, *F* and *V* represent the moment, axial and shear force respectively acting on the components, where the subscripts *s* and *c* are used to define the steel and concrete components respectively. The superscript + is used to denote forces on the right hand side of the element.

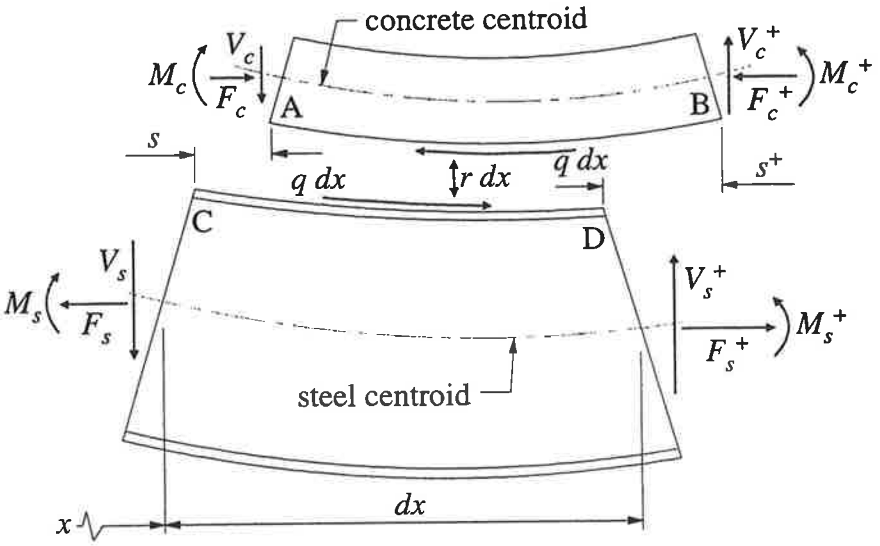

Figure 2.3: Forces acting on element *dx*.

The slip s in Fig. 2.3 increases to s^+ along dx and is defined by the following equation

$$s^+ = s + \left(\frac{ds}{dx}\right)dx \tag{2.2}$$

where ds/dx is known as the slip strain. Using the same superscript notation +, the following terms are defined

$$M_s^+ = M_s + \left(\frac{dM_s}{dx}\right)dx \tag{2.3}$$

and

$$M_c^+ = M_c + \left(\frac{dM_c}{dx}\right)dx \tag{2.4}$$

The longitudinal shear flow force, or longitudinal shear force per unit length, is defined as q so that qdx is the longitudinal shear force acting on each component. The vertical force across the interface is given by rdx and the force acting on each connector is equal to pq and can be defined as

$$pq = ks \tag{2.5}$$

where k is the connector stiffness, assumed to be constant.

From vertical equilibrium of the element in Fig. 2.3

$$V_s^+ = V_s + rdx \tag{2.6}$$

and

$$V_c^+ = V_c - rdx \tag{2.7}$$

and from longitudinal equilibrium

$$F = F_s = F_c \tag{2.8}$$

2.2.1.2 *Equilibrium*

To eliminate F, the summation of moments about the centroid of the steel component at x from the left support can be made, resulting in the following equation

$$M_s = M_s^+ + V_s^+ dx - qdx\frac{h_s}{2} - rdx\frac{dx}{2} \tag{2.9}$$

As the last term of the right hand side of Eq. 2.9 is of second order, it can be ignored. Substituting Eqs 2.3 and 2.6 into Eq. 2.9 and rearranging yields the following expression

$$\frac{dM_s}{dx} + V_s + rdx = \frac{1}{2}qh_s \tag{2.10}$$

Similarly for the concrete component

$$\frac{dM_c}{dx} + V_c - rdx = \frac{1}{2}qh_c \tag{2.11}$$

By defining the vertical shear at x as V^*, the following equation is defined

$$V_s + V_c = V^* \tag{2.12}$$

and by substituting Eqs 2.10 and 2.11 into Eq. 2.12, the following is obtained

$$q\frac{1}{2}(h_s + h_c) - \frac{dM_s}{dx} - \frac{dM_c}{dx} = V^* \tag{2.13}$$

As $d_c=1/2(h_s+h_c)$ for symmetrical sections, Eq. 2.13 can be simplified and rearranged to give

$$\frac{dM_s}{dx} + \frac{dM_c}{dx} + V^* = qd_c \tag{2.14}$$

2.2.1.3 *Elasticity*

As any uplift forces are small within the elastic range, and the commonly used stud shear connectors are designed to resist tensile forces across the interface, it can be assumed that there is no separation of the steel and concrete components along the interface, so that the curvatures ϕ in both components are the same. The modular ratio n is defined as

$$n = \frac{E_s}{E_c} \tag{2.15}$$

and, hence, the curvature is given by

$$\phi = \frac{M_s}{E_s I_s} = \frac{nM_c}{E_s I_c} \tag{2.16}$$

The longitudinal strain on the concrete side of the interface along A-B in Fig. 2.3 is given by the following expression where positive is taken as tension

$$\varepsilon_{AB} = \frac{1}{2} h_c \phi - \frac{nF}{E_s A_c} \tag{2.17}$$

where the first term of the right hand side represents the portion of the strain resulting from the bending of the component and the second term represents the strain due to the axial compressive force acting on the component. Similarly, the expression for the longitudinal strain along the interface C-D in Fig. 2.3 is defined as follows

$$\varepsilon_{CD} = -\frac{1}{2} h_s \phi + \frac{F}{E_s A_s} \tag{2.18}$$

2.2.1.4 *Compatibility*

The difference between the longitudinal strain along A-B and C-D in Fig. 2.3, given by Eqs 2.17 and 2.18 respectively, is called the slip strain *ds/dx* which can now be defined as

$$\frac{ds}{dx} = \frac{1}{2} h_c \phi - \frac{nF}{E_s A_c} + \frac{1}{2} h_s \phi - \frac{F}{E_s A_s} \tag{2.19}$$

Simplifying Eq. 2.19 and using the definition of $d_c = 1/2(h_s + h_c)$, the expression for the slip strain becomes

$$\frac{ds}{dx} = \phi d_c - \frac{F}{E_s}\left(\frac{n}{A_c} + \frac{1}{A_s}\right) \tag{2.20}$$

2.2.1.5 *The differential equation*

Equation 2.16 can be differentiated with respect to x to give

$$\frac{dM_s}{dx} = E_s I_s \frac{d\phi}{dx} \tag{2.21}$$

and

$$\frac{dM_c}{dx} = \frac{E_s I_c}{n}\frac{d\phi}{dx} \tag{2.22}$$

that can be substituted into Eq. 2.14 to eliminate M_s and M_c, giving the following expression

$$E_s\left(I_s + \frac{I_c}{n}\right)\frac{d\phi}{dx} + V^* = qd_c \tag{2.23}$$

By defining

$$I_o = I_s + \frac{I_c}{n} \tag{2.24}$$

and substituting Eqs 2.5 and 2.24 into Eq. 2.23, the following expression is obtained after simplification

$$\frac{d\phi}{dx} = \frac{(ks/p)d_c - V^*}{E_s I_o} \tag{2.25}$$

Differentiating Eq. 2.20 with respect to x gives

$$\frac{d^2s}{dx^2}=\frac{d\phi}{dx}d_c-\frac{dF}{dx}\frac{1}{E_s}\left(\frac{n}{A_c}+\frac{1}{A_s}\right) \tag{2.26}$$

where by defining

$$\frac{1}{A_o}=\frac{n}{A_c}+\frac{1}{A_s} \tag{2.27}$$

Eq. 2.26 can be simplified by substituting Eqs 2.25 and 2.27, and $dF/dx=-q=-ks/p$ to give

$$\frac{d^2s}{dx^2}=\frac{ks}{pE_sI_o}\left(d_c^{\,2}+\frac{I_o}{A_o}\right)-V^*\frac{d_c}{E_sI_o} \tag{2.28}$$

and by defining

$$\frac{1}{A'}=d_c^{\,2}+\frac{I_o}{A_o} \tag{2.29}$$

Eq. 2.28 becomes

$$\frac{d^2s}{dx^2}=\frac{ks}{pE_sI_oA'}-V^*\frac{d_c}{E_sI_o} \tag{2.30}$$

Finally, by defining the following parameters

$$\alpha^2=\frac{k}{pE_sI_oA'} \tag{2.31}$$

and

$$\beta=\frac{d_cpA'}{k} \tag{2.32}$$

Equation 2.30 can be expressed as the following differential equation

$$\frac{d^2s}{dx} - \alpha^2 s = V^* \alpha^2 \beta \tag{2.33}$$

A solution to the differential equation given by Eq. 2.33 is

$$s = K_1 \, sinh(\alpha x) + K_2 \, cosh(\alpha x) + \beta V^* \tag{2.34}$$

where K_1 and K_2 are integration constants, and α and β are functions of the cross-section of the composite beam and the stiffness of the shear connection as given by Eqs 2.31 and 2.32 respectively.

As Eq. 2.34 is a function of the shear force in the shear span V^*, the distribution of slip along the entire span must be defined using two equations as V^* is different in each shear span. Consequently, four boundary conditions must be defined in order to solve for the four integration constants. As this part of the development is the start of the original component of this research project, the derivation of the mathematical model is continued in Chapter 3.

2.3 OTHER LINEAR-ELASTIC PARTIAL-INTERACTION THEORIES

Not long after the presentation of Newmark, Siess and Viest's theory in 1951, other researchers began developing various partial-interaction theories based on slightly differing assumptions. The most interesting variation did not assume that the curvature in the steel and concrete components is the same (Adekola 1968), hence, separation between the components along the interface is permitted by modeling the axial stiffness, or foundation modulus k_t, of the shear connection. An additional assumption that was made, however, is that the uplift force is directly proportional to the differential deflection, which means that the axial stiffness remains linear-elastic. The difficulty with this theory arises from the necessity of two foundation moduli depending on the orientation of the uplift force. The foundation modulus for positive uplift, in regions where separation occurs, can be readily obtained from pull-out tests of shear connectors. However, in regions of negative uplift, where the concrete bears against the steel along the interface, no experimental values exist and furthermore, it is not initially known over what regions of the beam negative uplift exists.

The fundamental difference between this theory and that developed by Newmark et al can be illustrated by referring to Fig. 2.3 where a tensile force T, given by the following equation,

$$T = k_t(y_s - y_c) \tag{2.35}$$

must be added to the steel and concrete components along the interface where the term $(y_s\text{-}y_c)$ is the differential deflection, or separation, of the components along the interface. The derivation leads to two differential equations; one fourth order differential equation relating to the uplift force, and one second order differential equation relating to the axial force acting on the components. In regions of negative uplift, not all of the axial force from the steel component is transferred to the concrete component as the resulting frictional force F_{fr}, acting along the interface, will resist some of the load acting on the shear connection. Consequently, the differential equation relating to the axial force has an additional term, in regions of negative uplift, which accounts for friction and is given by the following expression

$$F_{fr} = \mu \frac{dT}{dx} \tag{2.36}$$

where μ is the coefficient of friction and dT/dx is the magnitude of the negative uplift force per unit length.

The solution to the two differential equations is not simple and is treated as a two-point boundary value problem that is solved using finite differences. The solution is further complicated by the fact that it is not initially known where negative uplift occurs, hence, an iterative procedure was adopted. The initial assumption was that the coefficient of friction is zero to indicate regions of negative uplift. Subsequent iterations incorporated a suitable coefficient of friction in the negative uplift regions until convergence was achieved. Singleton carried out a series of tests in 1985 to determine the coefficient of friction between steel and concrete under cyclic loading, which is briefly summarized in Section 2.4.

Adekola analyzed a simply supported composite beam with a single concentrated load and in which it was assumed that the coefficient of friction was zero, hence, the effect of friction was not being considered. A comparison between the partial-interaction stresses of the bottom flange of the steel component and the full-interaction stresses of the bottom flange was made. It was found that even for high degrees of interaction, in fact, higher than that expected in practice, the partial-interaction bottom flange stresses were at least 20% higher than the full-interaction stresses. The implication of this being that current full-interaction analyses are significantly overestimating the fatigue life of the steel component.

More recently, another research group (Robinson and Naraine 1987) solved the theoretical model developed by Adekola for the case of a simply supported beam with a single concentrated load and performed additional analyses. Included in the paper, however, was an interesting comparison with the theory developed by Newmark et al where it was assumed that there is no separation of the components. The conclusion that was made was that the difference in the shear force distribution along the interface is negligible regardless of which theory is used. It could be said, therefore, that it would be wiser to adopt the theory developed by Newmark et al, which is simpler because it assumes equal curvature and the resulting loss of accuracy is negligible. A significant observation was made, however, which could not have been predicted by a theory assuming equal curvatures. It was found that the moment induced in the slab in the vicinity of a concentrated load is considerably larger than that predicted by the equal curvature theory due to the high negative uplift forces in the area. The high negative uplift forces induce large vertical shear forces in the concrete slab. It was stated that the concrete deck resists approximately 77% of the vertical shear under a concentrated load. Such a high proportion of shear and correspondingly large moment in the concrete deck may result in tensile stresses near the bottom of the deck that may not have been accounted for in the design and, hence, could result in premature cracking of the concrete.

2.4 Cyclic coefficient of friction

Singleton investigated the variation of the coefficient of friction between steel and concrete under cyclic loading experimentally at the National University of Ireland (Singleton 1985). The tests consisted of applying up to 4 million cyclic displacements to a steel plate sandwiched between two blocks of concrete. The normal compressive force was applied through large springs.

It was found that the coefficient of friction fluctuated during the tests, consisting of a repetitive series of peaks and troughs ranging from 0.70 to 0.95. An initial increase was due to the wearing away of the weaker surface of the concrete block exposing the coarse, harder concrete. Additional cycles gradually wears away and polishes the surface causing a reduction in the coefficient of friction, until the coarse aggregate is once again exposed resulting in another increase in the coefficient of friction.

2.5 FATIGUE BEHAVIOR OF COMPOSITE BEAMS WITH STUD SHEAR CONNECTORS

The fatigue behavior of composite beams with stud shear connectors is unusual because the mechanical properties of the connectors are continually changing under the application of cyclic loads. This section describes the changes in the properties of stud shear connectors that occur due to cyclic loading and presents mathematical models that have been developed to predict the remaining strength and endurance of composite beams.

2.5.1 Fatigue behavior of stud shear connectors

Sinclair carried out one of the earliest fatigue tests performed on stud shear connectors at the University of Illinois (Sinclair 1956). The tests consisted of a ¾ inch (19 mm) stud, welded onto a steel plate, which was cyclically loaded to failure under varying stress ranges so that an S-N curve could be produced. The studs were loaded directly, as they were not encased in concrete, which is not a realistic approximation as the interaction between the stud and surrounding concrete is not present. Subsequent fatigue tests used more realistic and complex specimens where the studs were encased in concrete so that they were loaded indirectly, examples of which are shown in Section 2.6.

A typical example of the fatigue failure of a stud shear connector is shown in Fig. 2.4 where the crack front is the horizontal straight line within the shank of the stud and located axially at the interface between the shank and the weld collar. The crack front started at the lower end of the shank immediately cyclic loads were applied and gradually progressed up the shank at a fairly uniform rate as shown by the light zone within the area of the shank (Oehlers and Bradford 1995). The crack continued to propagate until the remaining or residual strength was equal to the peak uni-directional load after which fracture occurred as can be seen by the darker area within the shank above the crack front. The residual strength just prior to fracture, as a proportion of the initial static strength, is roughly equal to the area of the dark fracture zone, as a proportion of the area of the shank of the stud shear connector.

Figure 2.4: Fatigue failure of a stud shear connector.

An oblique view of a stud shear connector after fatigue failure is shown in Fig. 2.5. In this case, crack propagation can be seen to have occurred at the flange/weld-collar interface, that has the same effect as at the weld-collar/shank interface in Fig. 2.4, and also the crack propagation has occurred well above the weld collar (Oehlers and Bradford 1995). The latter fatigue failure zone that commonly occurs in practice is extremely important because it allows the stud shear connector to fail in a ductile manner once fracture occurs (Oehlers 1990a).

Figure 2.5: Fatigue deformation of a stud shear connector.

2.5.2 Cyclic load-slip characteristics of stud shear connectors

Tests have shown (Oehlers and Coughlan 1986) that the cyclic behavior of stud shear connectors can be represented by the load-slip characteristics shown in Fig. 2.6. The general shape of the load-slip curve, however, was already determined experimentally by 1959 from tests carried out at Lehigh University (Thurlimann 1959), however, no attempt to quantify the curve was made for some time. The following sections quantify the load-slip curve shown in Fig. 2.6.

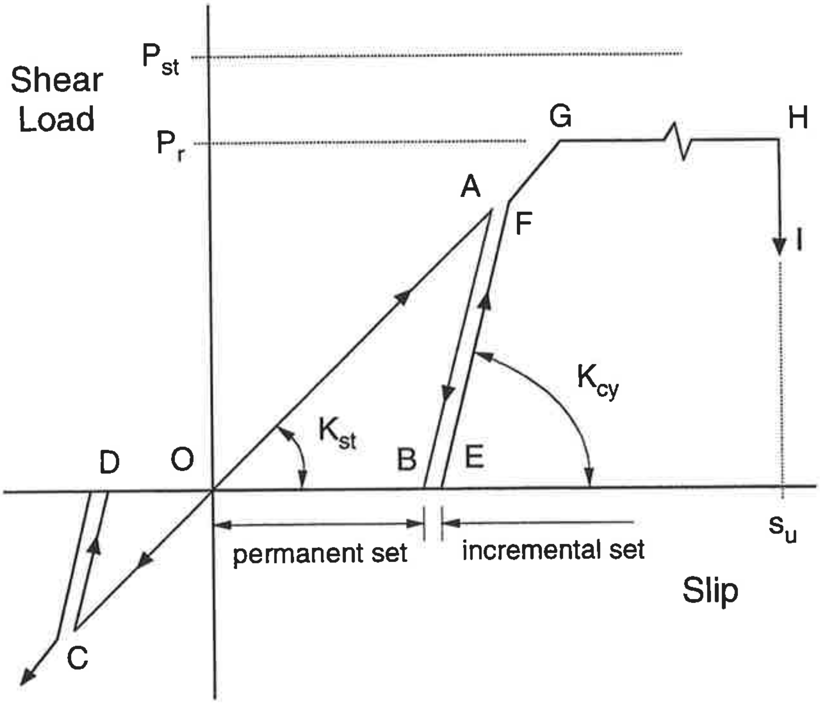

Figure 2.6: Cyclic load-slip behavior of stud shear connectors.

On the initial application up to the peak of the cyclic load, the connector follows the path O-A of initial static stiffness K_{st} given by the following equation (Oehlers and Bradford 1995)

$$K_{st} = \frac{P_{st}}{d_{sh}(0.16 - 0.0017 f_c)} \tag{2.37}$$

where P_{st} is the static strength prior to cyclic loading, d_{sh} is the diameter of the shank of the stud, f_c is the concrete cylinder compressive strength, and the units are in N and mm. The first group to truly identify the parameters governing the static strength of stud shear connectors in standard push-out specimens (Ollgaard, Slutter and Fisher 1971) suggested the following equation

$$(P_{st})_{push} = 0.5 A_{sh} \sqrt{f_c E_c} \tag{2.38}$$

where A_{sh} is the cross-sectional area of the shank of the stud shear connector, E_c is the stiffness of the concrete and the units are again in N and mm. However, as the studs used by Ollgaard et al all had the same tensile strength f_u, and it was assumed that the stiffness of the steel E_s was constant, these parameters were not included in their equation (Eq. 2.38). Statistical analyses (Oehlers and Johnson 1987), however, modified Eq. 2.38 to include f_u and E_s to give the following relationship

$$(P_{st})_{push} = \left(5.3 - \frac{1.3}{\sqrt{n}}\right) A_{sh} f_u^{0.65} f_c^{0.35} \left(\frac{E_c}{E_s}\right)^{0.40} \tag{2.39}$$

where n represents the number of studs that are expected to fail as a group. If the mean static strength is required, n should be taken as ∞. As it was suggested (Oehlers and Bradford 1995) that the compressive force induced across the steel-concrete interface of push-out specimens increased the apparent strength of the stud shear connectors relative to those in a composite beam by about 20%, the following equation was given to predict the static strength of the shear connection in a composite beam.

$$(P_{st})_{beam} = \left(4.3 - \frac{1.1}{\sqrt{n}}\right) A_{sh} f_u^{0.65} f_c^{0.35} \left(\frac{E_c}{E_s}\right)^{0.40} \tag{2.40}$$

If the load is then removed, path A-B of cyclic stiffness $K_{cy} = 2.8K_{st}$ (Oehlers and Coughlan 1986) will be followed in Fig. 2.6, at a permanent set O-B. If a reverse cyclic load is being applied, the connector will follow the path B-O-C-D-O. On further loading, the connector follows the path O-E-F where the cyclic load has induced a further increase of B-E in the permanent set which will be referred to as the incremental set. If an overload is now applied that is sufficient to fracture the connector, the connector will follow the path F-G-H-I where failure will occur at the residual strength P_r, which is less than the static strength of the shear connection prior to cyclic loads P_{st}, and ultimate slip (Oehlers and Coughlan 1986) given by the following equation

$$s_u = (0.48 - 0.0042 f_c) d_{sh} \tag{2.41}$$

where the units are N and mm.

2.5.2.1 *Permanent set*

Because the shear connectors in a composite beam are loaded indirectly (Toprac 1965), that is the shear force on the connector depends on its stiffness, the shear force on a connector in a composite beam depends on the permanent set. For example, it has been shown that: overloads that are applied to the beam reduce the cyclic range and, hence, increase the residual endurance and residual strength (Slutter and Fisher 1966); that the permanent set induces a fatigue limit in the beam below which fatigue damage does not occur (Oehlers and Singleton 1986); and that composite beams made using propped construction have a smaller endurance than those made using unpropped construction (Oehlers and Bradford 1995, Slutter and Fisher 1966, and Oehlers and Singleton 1986).

2.5.2.2 *Incremental set*

The incremental set in Fig. 2.6 is a loss of energy per cycle due to crack propagation within the stud and powdering of the concrete bearing against the stud (Oehlers and Foley 1985). This loss of energy has been found to occur as soon as cyclic loads are applied to stud shear connections as was first shown by Thurlimann in plots of number of cycles N against slip s (Thurlimann 1959) although no attempts were made to quantify this observation. Experimental data from other researchers also showed the existence of incremental and permanent set (Toprac 1965 and Roderick and Ansourian 1976), however, it was not until Hallam that one of the first attempts to quantify incremental set was made (Hallam 1976). Hallam first determined the slope of the s-N plot, which is referred to as ds/dN, that was found to be constant for most of the fatigue life. Hallam then plotted the load range as a percent of the static strength against ds/dN on a semi-logarithmic scale to give the following expression

$$\log\left(\frac{ds}{dN}\right) = -10.00 + 0.1299\left(\frac{R}{P_{st}} \times 100\right) \tag{2.42}$$

where R is the range of load defined as the difference between the maximum and minimum load of a cycle and the slip is measured in mm.

Subsequent research carried out by Oehlers and Foley, using an energy release per cycle approach developed another relationship for incremental set (Oehlers and Foley 1985), which is similar in form to that proposed by Hallam, and is given by the following equation

$$\frac{ds}{dN} = 1.7 \times 10^{-5}\left(\frac{R}{P_{st}}\right)^{4.5} \tag{2.43}$$

where the units are again in N and mm.

As a consequence, the residual strength of stud shear connectors after cyclic loading P_r is always less than their static strength P_{st} prior to cyclic loading (Oehlers 1990c). Furthermore, this incremental set allows the connectors to fail as group as it allows the stronger connectors to attract more load than the weaker connectors (Toprac 1965, and Mainstone and Menzies 1967), hence, design or assessment can be based on the characteristic strength or endurance of the mean of a group as opposed to the characteristic property of an individual connector (Oehlers and Johnson 1987).

2.5.3 General forms for representing the fatigue damage

It was shown in the previous section that the loss of energy associated with the incremental set represents a loss of strength of the stud shear connection. Tests have shown (Oehlers 1990c, and Oehlers and Foley 1985) that this loss of strength can be assumed to be linear as shown by line A in Fig. 2.7 which is referred to as the crack propagation approach (Oehlers and Bradford 1995, and Johnson and Oehlers 1996) where N is the number of cycles of a load that have been applied and E is the endurance. However, current design techniques assume that there is no reduction in strength whilst $N < E$ as shown by line B in Fig. 2.7 and this technique will be referred to as the standard approach.

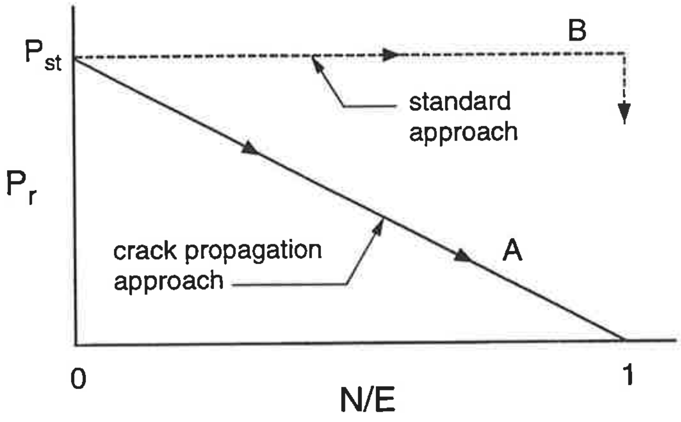

Figure 2.7: Variation of the residual strength.

2.5.3.1 *Crack propagation approach*

The variation in the residual strength P_r for the crack propagation approach in Fig. 2.7 is given by the following accumulated damage law (Oehlers and Bradford 1995, and Johnson and Oehlers 1996)

$$\sum_{k=1}^{k=z} \frac{N_k}{E_k} \le 1 - \frac{P_r}{P_{st}} \tag{2.44}$$

where there are z magnitudes of the cyclic ranges R.

2.5.3.1.1 *Asymptotic endurances*

As the number of cycles increase, the strength of the shear connection reduces as defined by the failure envelope (Oehlers and Bradford 1995) shown in Fig. 2.8 for a given range R. Failure will occur when either the peak load of a cycle P_{max} is equal to the residual strength after N cycles, or when an overload occurs at N^* cycles and the overload exceeds the residual strength.

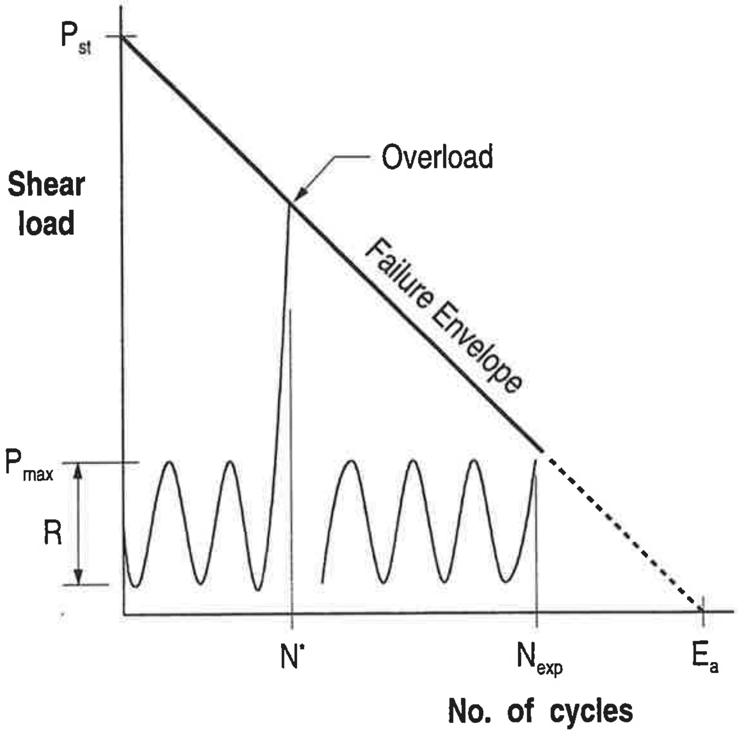

Figure 2.8: Residual strength failure envelope.

So, it becomes evident that the experimentally determined number of cycles to cause failure N_{exp}, for a given range, is inherently related to the magnitude of the peak load. To eliminate this effect, the asymptotic endurance can be calculated from the following equation (Oehlers and Bradford 1995) that was derived from a statistical analysis of fatigue data

$$E_a = 10^{\left(3.12 - \frac{0.70}{\sqrt{n}}\right)} \left(\frac{R}{P_{st}}\right)^{-5.1} \tag{2.45}$$

where E_a is the asymptotic endurance of a group of n connectors at two standard deviations.

2.5.3.2 *Standard approach*

The standard approach endurance is often assumed to depend on R/P_{st} or on R/A_{sh}. Due to variations between the restraints on push specimens and the parameters assumed to affect the fatigue endurance, several endurance equations have been proposed (Oehlers 1990b), such as the following mean endurance equation (Slutter and Fisher 1966)

$$E_{mean} = 8.08 \times 10^{15} \left(\frac{R}{A_{sh}}\right)^{-5.3} \tag{2.46}$$

where E_{mean} is the mean endurance and the units are in N and mm.

However, it has long been suggested (Hallam 1976), and statistical analyses (Oehlers 1990b) have confirmed, that the R/P_{st} parameter gives the least scatter of results, and from these statistical analyses it was found that the characteristic endurance can be given by

$$E_{ch} \quad = \quad 10^{\left(15.9 - \frac{0.7}{\sqrt{n}}\right)} \left(\frac{R}{A_{sh}}\right)^{-5.1} \tag{2.47}$$

where the units are in N and mm, or more appropriately by

$$E_{ch} \quad = \quad 10^{\left(2.27 - \frac{0.70}{\sqrt{n}}\right)} \left(\frac{R}{P_{st}}\right)^{-5.4} \tag{2.48}$$

The standard approach accumulated damage law is given by

$$\sum_{k=1}^{k=z} \frac{N_k}{E_k} \leq 1 \tag{2.49}$$

which is essentially Miner's cumulative damage rule (Miner 1945) that was first verified in 1976 as a suitable method of predicting the fatigue life of stud shear connectors under variable amplitude repeated loading (Hallam 1976).

2.5.4 Fatigue equations for design and assessment

General fatigue equations have been developed (Oehlers and Bradford 1995, and Oehlers, Gosh and Wahab 1995) for both the standard approach and for the crack propagation approach of the general forms of the fatigue damage described previously.

2.5.4.1 *Generic fatigue equation*

The fatigue material properties of Eqs. 2.44 to 2.49 can be represented by the following generic forms

$$\sum \frac{N}{E} = A \tag{2.50}$$

where A is the residual strength constant and

$$E = C\left(\frac{R}{X}\right)^{-m} \tag{2.51}$$

where C is a constant, m is the exponent in the residual strength equation and X can be any parameter such as P_{st}.

The types of vehicles that traverse a bridge throughout its life are numerous, and it is necessary to calculate the magnitude and frequency of the range of cyclic forces applied to the shear connection in order to determine the fatigue damage caused by each vehicle. In practice, a Standard Fatigue Vehicle (SFV) is used as it is not feasible to determine the stress range caused by each vehicle expected to traverse a bridge. A typical fatigue vehicle is shown in Fig.

2.9 (BS5400 1980) and the variation in the fatigue vehicle weights is represented as a proportion of the weight of the SFV, *W*, as shown in the second column of Table 2.1 known as the load spectrum. The probability of occurrence of each fatigue vehicle, *B*, is also given in Table 2.1 where the summation of the probabilities must equal unity.

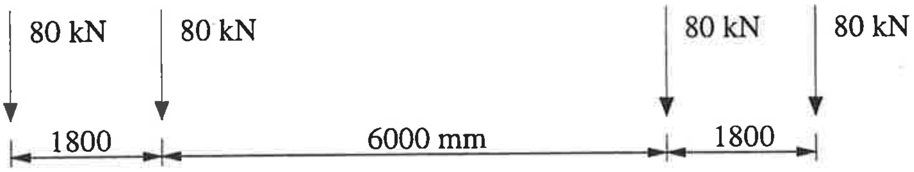

Figure 2.9: Standard Fatigue Vehicle (BS5400 1980).

Table 2.1: Load spectrum.

Fatigue Vehicle	Weight (W)	Probability (B)	BW^m
1	W_1	B_1	$B_1W_1^m$
2	W_2	B_2	$B_2W_2^m$
...	...	...	...
Y	W_y	B_y	$B_yW_y^m$
		$\Sigma = 1.0$	$L_f = \Sigma BW^m$

The distribution of force in a shear flow influence line diagram, at a given design point along the steel-concrete interface, for the traversal of a particular fatigue vehicle must be converted to a set of equivalent cyclic forces that produce the same fatigue damage. One method of doing this is known as the reservoir method of cyclic counting (BS5400 1980), which assumes that the influence line diagram is the cross-section of a reservoir that is to be emptied from the lowest point.

The cross-section of the reservoir is obtained by drawing two shear flow influence line diagrams adjacent to each other as shown in Fig 2.10, where the distance from the top of the reservoir to the lowest point, denoted by R_1, is one equivalent cyclic range. Any other remaining pockets must be drained from their lowest points until there are no more pockets remaining. Each of the remaining pockets that are drained represents an additional equivalent cyclic range. For the example shown in Fig. 2.10, there is only one more cyclic range, R_2.

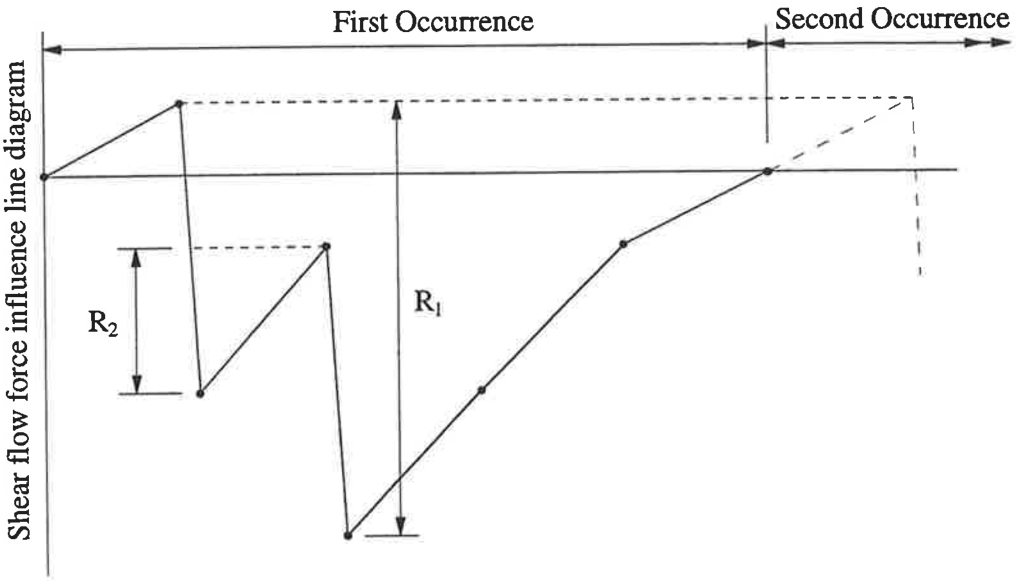

Figure 2.10: Reservoir method.

The equivalent cyclic forces are recorded in tabular form, known as the force spectrum shown in Table 2.2. The frequency f is the number of times the range R appears in the influence line diagram for the design point.

Table 2.2: Force spectrum.

Range number	Range (R)	Frequency (f)	fR^m
1	R_1	f_1	$f_1R_1^m$
2	R_2	f_2	$f_2R_2^m$
...	...	...	...
Y	R_y	f_y	$f_yR_y^m$
			$F_f = \Sigma fR^m$

The magnitude of the range for a given fatigue vehicle is therefore equal to W_kR_k where substitution into Eq. 2.51 gives

$$E_k = C\left(\frac{W_k R_k}{X}\right)^{-m} \tag{2.52}$$

and the number of times the range will occur during the life of the bridge is

no. of occurrence

$$N_k = B_k T_k f_k \tag{2.53}$$

where T_k is the total number of fatigue vehicle traversals. Substituting Eqs 2.52 and 2.53 into Eq. 2.50 and rearranging gives the following expression

$$\frac{\sum_{k=1}^{k=y}(B_k T_k f_k)(W_k R_k)^m}{CX^m} = A \tag{2.54}$$

Defining the following two terms

$$\left(L_f\right)_k = \sum_{k=1}^{k=y} B_k W_k^m \quad C \tag{2.55}$$

where L_f is called the load factor and is given by the sum of the last column in the load spectrum (Table 2.1), and

$$\left(F_f\right)_k = \sum_{k=1}^{k=y} f_k R_k^m \tag{2.56}$$

where F_f is called the force factor and is given by the sum of the last column in the force spectrum (Table 2.2). Equations 2.55 and 2.56 can be substituted into Eq. 2.54 and rearranged to give the following generic fatigue equation (Oehlers 1992 and Oehlers and Bradford 1995)

$$X^{-m} = \frac{AC}{\sum_{k=1}^{k=y}\left(TF_f L_f\right)_k} \tag{2.57}$$

where there are y fatigue zones and a fatigue zone is defined as a period of T_y fatigue vehicle traversals where both F_f and L_f are constant.

2.5.4.2 *Crack propagation design equation for stud shear connectors*

Using the crack propagation fatigue material properties in Eqs. 2.44 and 2.45, the generic fatigue equation (Eq. 2.57) can be written in the following form (Oehlers and Bradford 1995)

$$Q_{of} = \left[\frac{1318\left(1-\dfrac{Q_o}{Q_{of}}\right)}{T_1(F_f)_1(L_f)_1 + T_2(F_f)_2(L_f)_2 + \ldots\ldots + T_y(F_f)_y(L_f)_y} \right]^{\frac{1}{5.1}} \qquad (2.58)$$

where Q_o is the static shear flow strength required, such as the strength required to resist the maximum overload and Q_{of} is the shear flow strength when the structure is first built.

The application of the crack propagation approach to design is illustrated in Fig. 2.11 where Q_o is the known static strength requirement and Q_{of} can be derived from Eq. 2.58 and is a function of Q_o. The increase in strength at a design point in the beam *(Q_{of} - Q_o)* is the additional static strength required to cope with the reduction in strength due to fatigue damage and occurs along the length of the beam.

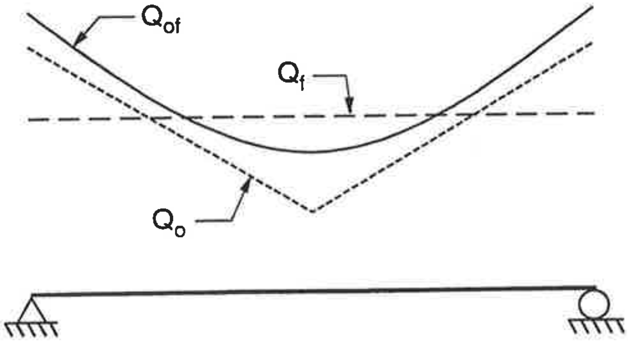

Figure 2.11: Fatigue analysis procedures.

The standard approach is also illustrated in Fig. 2.11 where separate calculations are used to derive the static requirement Q_o and the endurance requirement Q_f from which the upper bound of the two separate approaches are used in the design. It can be seen that the crack propagation approach is a fundamentally new approach in design.

2.5.4.3 *Crack propagation assessment equation for stud shear connectors*

Equation 2.58 can be written in the following form for the assessment of the residual strength of the stud shear connectors Q_{res} of an existing structure

$$Q_{res} = Q_{st}\left[1 - \frac{Q_{st}^{-5.1}\sum_{k=1}^{k=y}\left(TF_f L_f\right)_k}{1318}\right] \qquad (2.59)$$

where Q_{st} is the shear flow strength of the stud shear connectors prior to fatigue loading. Equation 2.59 can be rearranged in the following form in order to determine the residual endurance T_y when a residual strength Q_{res} is required.

$$T_y = \frac{1318 Q_{st}^{5.1}\left(1 - \frac{Q_{res}}{Q_{st}}\right) - \sum_{k=1}^{k=y-1}\left(TF_f L_f\right)_k}{\left(F_f L_f\right)_y} \qquad (2.60)$$

2.5.5 Fatigue behavior of composite beams

Computer simulations of composite beams that incorporate the stud shear connector load-slip characteristics in Fig. 2.6 have been used to illustrate the general fatigue behavior of composite beams.

2.5.5.1 *Longitudinally stationary loads*

The results (Oehlers and Singleton 1986) from a computer simulation of a simply supported composite beam with a uniform distribution of stud shear connectors that is subjected to cyclic loads at the mid-span are shown in Fig. 2.12. The line marked A is the distribution of the shear flow forces along the beam when the beam is first loaded so that the connectors are still following the linear partial-interaction path such as O-A-G in Fig. 2.6. The line marked B is the distribution just prior to fatigue failure where the connectors are following path O-B-A in Fig. 2.6 and the difference between lines A and B in Fig. 2.12 is caused by the gradual reduction in stiffness due to the incremental set. It can be seen that the incremental set has the beneficial effects of both reducing the shear flow forces, so that both the residual strength and endurance will be greater than originally anticipated, and in redistributing them more uniformly, so that the connectors can fail as a group close to their mean properties.

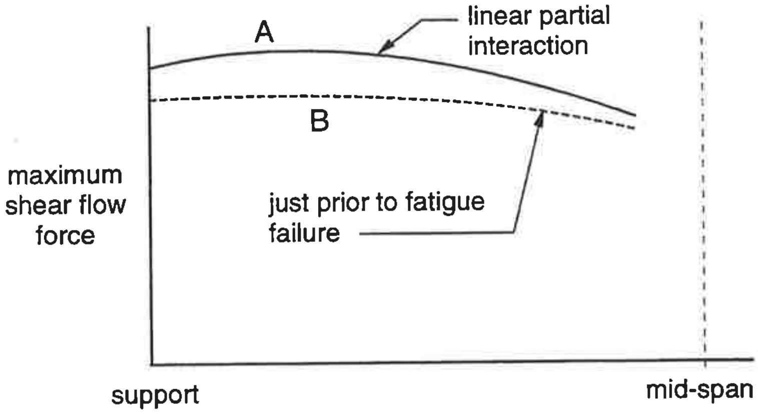

Figure 2.12: Redistribution of shear flow through incremental set.

2.5.5.2 ***Longitudinally moving loads***

The effect of longitudinally moving loads (Oehlers and Carroll 1987) on the fatigue behavior of a composite beam is illustrated in Fig. 2.13 where q^* is the shear flow force. The envelope marked A was derived from a full-interaction analysis and would be used in most standard procedures for fatigue design and, hence, will be used as the benchmark. The envelope marked B was derived from a linear partial-interaction analysis. It can be seen that partial-interaction can considerably reduce the shear flow forces and, hence, considerably increase the residual endurance and the residual strength. However, the reduction in the shear flow due to partial-interaction depends on the span of the beam; the reduction decreases as the span increases. The envelope marked C is a partial-interaction analysis that allows for incremental set and it can be seen that the incremental set redistributes the shear load. It is also worth noting that partial-interaction reduces the region of the beam that is subjected to reverse cyclic loading so that there is a tendency for the connectors to be loaded uni-directionally.

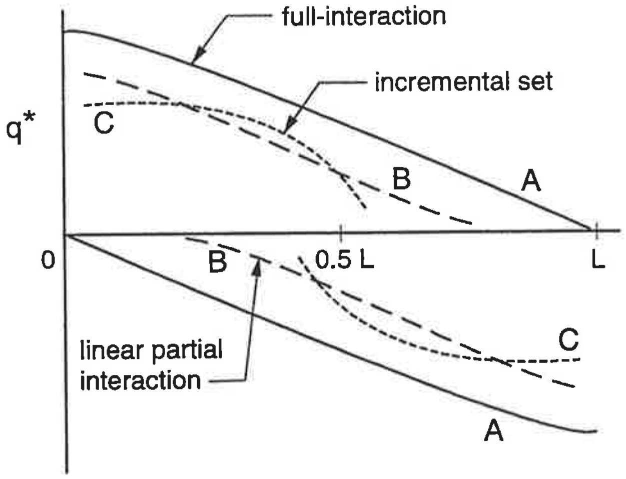

Figure 2.13: Shear flow envelopes induced by longitudinally moving loads.

2.5.6 Beneficial effects of interface friction

The beneficial effect of interface friction is illustrated in Fig. 2.14 for the case of a single point load moving across a composite beam (Oehlers and Bradford 1995, and Oehlers and Bradford 1999). The shear flow force envelope is marked A. The shear flow frictional resistance is marked B and tends to infinity at the supports. The hatched region is the shear flow force resisted by the stud shear connectors. It can be seen that friction reduces both the range and peak of the shear flow force resisted by the stud shear connectors and, hence, both increases the residual endurance and residual strength above that anticipated in the original design. Furthermore, the beneficial effect of friction is greatest at the supports.

Procedures for incorporating the beneficial effect of friction into assessment equations such as Eqs 2.59 and 2.60 have been determined (Oehlers and Bradford 1995) and have the following form

$$q = \frac{VA_c y}{I_{nc}} - \frac{V\mu}{L_{sp}} \tag{2.61}$$

where $VA_c y/I_{nc}$ is the well known equation for the shear flow force, and the term $V\mu/L_{sp}$ is the shear flow force resisted by friction in which V is the shear force acting at the design point, L_{sp} is the length of the shear span that includes the design point, μ is the coefficient of friction at the interface between the concrete slab and steel beam of the composite beam, A_c is the cross-sectional area of the concrete element, y is the distance between the centroid of the concrete element and the centroid of the transformed concrete section of the composite beam and I_{nc} is the second moment of area of the transformed concrete section.

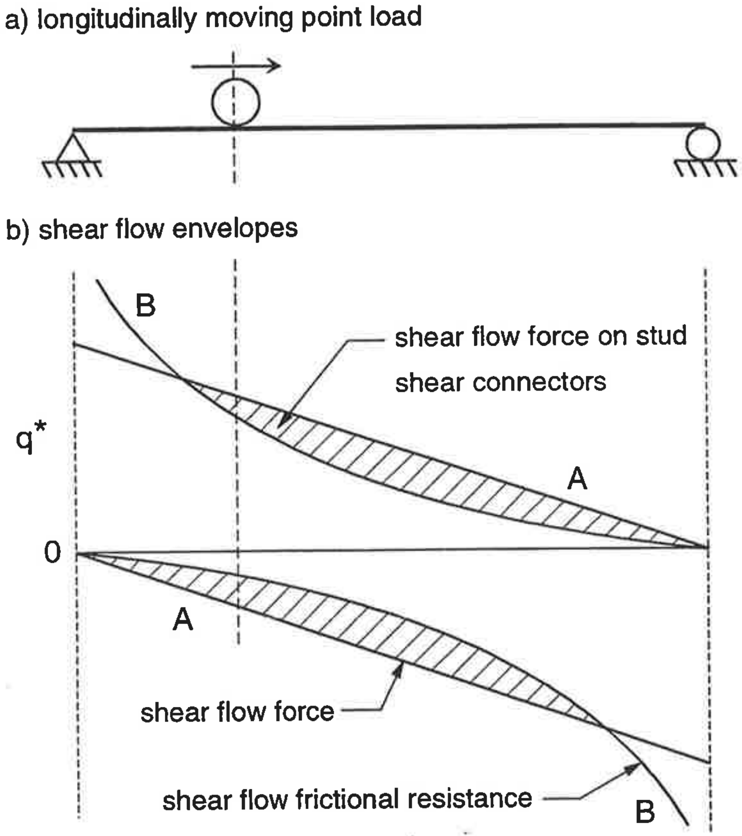

Figure 2.14: Beneficial effect of friction.

2.6 REVERSE-CYCLIC TESTS ON STUD SHEAR CONNECTORS

Numerous tests by researchers worldwide have investigated the fatigue behavior of stud shear connectors experimentally (Slutter and Fisher 1966, Mainstone and Menzies 1967, Oehlers and Foley 1985, and Gattesco and Giuriani 1996). The vast majority of the classical push-out tests subjected the specimens to either monotonically increasing static loads or uni-directional fatigue loads.

It is known, however, that the shear connection in composite beams is subjected to reverse-cycle loading for at least part of the fatigue life, if not all of it, as can be seen in Fig. 2.13. Even though the total range tends towards a uni-directional one in simply supported composite beams due to incremental set (Oehlers and Bradford 1995), the connectors within the mid-span region of the beam are subjected to reverse-cyclic loads over a large portion of their fatigue lives. Unfortunately, very little reverse-cycle fatigue tests on stud shear connectors have been undertaken, furthermore, little analysis of the results was made.

2.6.1 Early reverse-cycle tests

The initial reverse-cycle tests (Slutter and Fisher 1966, and Mainstone and Menzies 1967) formed only a small part of extensive experimental programmes. The specimens used in the reverse-cycle tests were essentially the same as those of the uni-directional tests with slight variations to permit application of the load in the reverse, or opposite, direction. Details of these early reverse-cycle tests are given in the following two sections.

2.6.1.1 *Slutter and Fisher*

The experimental investigation was to determine the fatigue strength of stud shear connectors and channel connectors in order to optimize their use in composite highway bridges. The tests were performed at Lehigh University, Pennsylvania, where 35 fatigue tests were carried out on specimens containing ¾ inch (19 mm) stud shear connectors, nine of which were reverse-cycle, and 9 fatigue tests used 7/8 inch (22 mm) stud shear connectors, three of which were reverse-cycle.

Each of the specimens had four studs welded onto the top flange of a standard I-section and embedded in reinforced concrete as shown in Fig. 2.15. These tests were unusual in the sense that the load was applied through the edge of the concrete slab, where traditional push-out tests were loaded through the steel section. The load was simply applied to both sides of the concrete slab for the reverse-cycle tests and load cycles were applied at a frequency of 4 Hz.

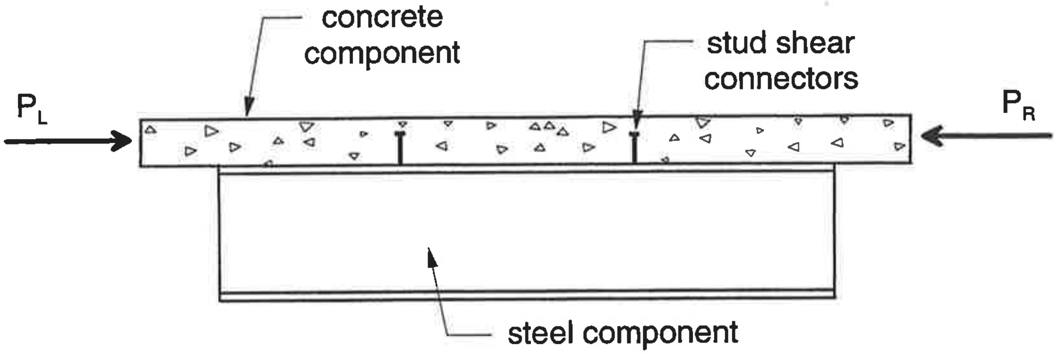

Figure 2.15: Experimental set-up (Slutter and Fisher 1966).

The results for the relevant tests are summarized in Table 2.3 where the maximum load is the peak load of the load cycle, and the range is the difference between the maximum and minimum loads of the cycle.

Table 2.3: Summary of results (Slutter and Fisher 1966).

Specimen	Load type[1]	Stud Diameter [mm]	Maximum Load [kN]	Range [kN]	No. of cycles to failure ($x10^3$)
a1A	R	19	78.8	125.8	1587.4
b1A	R	19	78.8	125.8	1975.2
c1A	R	19	78.8	125.8	2557.5
a2A	R	19	110.4	157.4	104.6
b2A	R	19	110.4	157.4	104.8
c2A	R	19	110.4	157.4	171.1
a3B	U	19	141.5	125.8	139.4
b3B	U	19	141.5	125.8	114.7
c3B	U	19	141.5	125.8	199.5
a4B	U	19	173.1	157.4	41.5
b4B	U	19	173.1	157.4	50.7
c4B	U	19	173.1	157.4	58.7
e1G	R	22	106.8	170.9	1056.4
e2G	R	22	150.0	214.0	218.6
e3H	U	22	192.2	170.9	112.5
e4H	U	22	235.4	214.0	33.0

1 U - uni-directional cyclic loading
R - reverse-cyclic loading

All of the specimens failed in fatigue where cracking initiated at the weld and propagated through the flange of the steel section. However, in cases where the weld penetration was not complete, the fatigue crack propagated through the weld. The results were plotted on an S_r-N curve and expressed by the following mathematical model

$$S_r = AN^{-B} \tag{2.62}$$

where A and B are regression coefficients and S_r is the stress range. However, as it was realized that for the same total range, the fatigue life of a shear connection subjected to reverse-cyclic loading was longer than the fatigue life of a connection under uni-directional loading, the reverse-cycle tests were not included in the analysis. Furthermore, as the fatigue life prediction for reverse-cycle loading would be conservative when using the relationships from uni-directional tests, no further investigations or analyses were carried out on reverse-cycle tests.

2.6.1.2 *Mainstone and Menzies*

A series of 83 push-out tests were carried out at the Building Research Station (Mainstone and Menzies1967) in parallel with the drafting of the then new British Code (CP117: Part 2 1967) in order to provide additional data with regards to the design of stud shear connectors. The tests were carried out on ¾ inch (19 mm) stud shear connectors, channel connectors and hoop connectors, and the loading rate varied from 0.25 Hz to 4 Hz depending on the anticipated length of the fatigue life.

Eleven of the specimens containing the stud shear connectors, each of which contained four studs, were tested statically, and of the 23 fatigue tests, seven of them were reverse-cycle tests. A traditional type of push-out specimen was used in these tests where the load was applied through the steel section as shown in Fig. 2.16. A set of four springs, where one end of the spring was fastened to the steel section and the other end to the concrete block, were tensioned prior to the reverse-cycle tests in order to induce the force in the opposite direction.

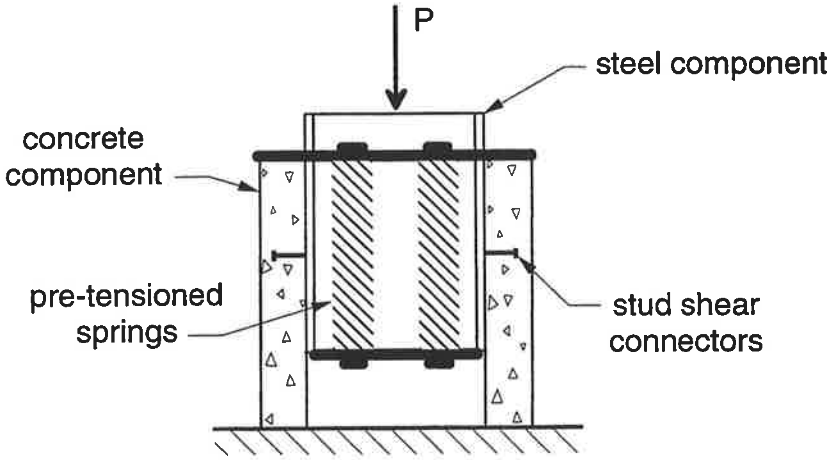

Figure 2.16: Experimental set-up (Mainstone and Menzies 1967).

Based on the results of nine static tests, the average static strength of the specimens was found to be 427 kN. The results of the relevant fatigue tests are given in Table 2.4.

Table 2.4: Summary of results (Mainstone and Menzies 1967).

Specimen	Load type[1]	Maximum Load [kN]	Range [kN]	No. of cycles to failure ($x10^3$)
S10	U	267.2	133.6	1700.0
S12	U	298.8	149.6	679.0
S13	R	79.6	159.6	630.0
S14	R	99.6	199.2	200.0
S15	R	49.6	159.6	481.0
S17	R	69.6	139.6	2200.0
S18	R	109.6	219.2	101.0
S20	U	328.8	165.6	669.0
S21	R	139.6	278.8	21.0
S23	U	338.8	84.8	657.0
S24	U	348.8	87.2	9.2
S25	U	368.8	92.0	13.3
S27	U	348.8	174.4	8.97
S28	U	348.8	174.4	6.0
S30	U	348.8	174.4	13.1
S31	U	338.8	169.2	8.6
S32	U	368.8	92.0	165.0
S33	U	394.8	89.6	106.0
S34	R	129.6	243.6	16.5

[1] U - uni-directional cyclic loading
R - reverse-cyclic loading

The goal of the tests was to establish relationships between the maximum load and the fatigue life of the shear connection at different minimum to maximum load ratios. Although it was again evident that the fatigue life of stud shear connectors with the same total range is longer under reverse-cyclic loading compared to the fatigue life of connectors under uni-directional loading, no additional comparison or analysis was suggested.

An additional feature that was monitored in this investigation was the slip, and it was plotted against the number of cycles elapsed as a percent of the estimated fatigue life of the connectors. It was shown that for the uni-directional specimens, the rate of increase in slip per cycle, *ds/dN*, remains constant until approximately 20% of the fatigue life remains at which time it increases rapidly. A similar observation was made for the reverse-cycle specimens. This is significant as it indicates that if the slip was monitored on an existing bridge, the remaining life of the shear connection could be predicted.

2.6.2 Recent reverse-cycle tests

Up until recently, there appears to have been little, if any, research carried out on the reverse-cycle behavior of stud shear connectors. This is most probably because it is felt that it is not necessary to refine the understanding of reverse-cycle loading as the results are conservative when compared to uni-directional cyclic loading with the same total range.

It was realized, however, that detailed experimental results are required to more accurately carry out numerical analyses and refine computer simulations of composite beams subjected to cyclic loading (Gattesco and Giuriani 1996). In addition, it was also stated (Gattesco, Giuriani and Gubana 1997) that for long span composite beams, if the connection is not stiff enough, the slip may be in excess of approximately 1 mm which would load the shear connectors beyond the linear-elastic range while the rest of the structure remains linear-elastic. As a result, a force in the opposite direction occurs as the loads are removed and the beam returns to its original configuration due to the inelastic unloading deformations of the connectors.

A test specimen was designed, which is suitable for static, uni-directional cyclic and reverse-cyclic loading. The specimen is considerably more sophisticated than the classical push-test specimen as it was designed to more accurately simulate the stress conditions surrounding a stud shear connector in a composite beam. A pilot investigation consisting of four tests; two static tests and two cyclic tests (Gattesco and Giuriani 1996), was performed where the viability of the specimen was confirmed. The cyclic tests were of the high-amplitude, low-cycle type such that failure occurs after a relatively small number of cycles. The cyclic load was applied in blocks of increasing total range by both increasing maximum load and decreasing the minimum load, where a new block was applied after the incremental set of the previous block settled to a constant rate. As a result of the large total range and high peak load, failure occurred after only 1223 and 625 cycles in the two cyclic tests.

Due to the small number of tests, the conclusions (Gattesco and Giuriani 1996) could only be qualitative, however, an interesting observation was made in that the increment of slip becomes very nearly constant after the first few initial cycles which implies that there is a progressive accumulation of damage and no shakedown. The fact that the damage is progressive is a key point which was first noted in the 1960s (Toprac 1965), however, it is still generally assumed that there is no reduction in strength and stiffness of the shear connection until failure, as shown previously in Fig. 2.7.

A further eight tests were performed (Gattesco, Giuriani and Gubana 1997) which, in addition to reversal of the shear load, looked into the reduction in the range as the number of cycles increases due to the redistribution of the longitudinal shear forces along the length of the beam. The research methodology adopted was a unique one in that a strain-life approach was used, where the maximum slip is kept constant, opposed to the load-life approach typically used where the range is kept constant. This approach was taken because the slip of the shear connection in a structure is governed by the global behavior and, hence, tends to remain constant and the range reduces as a result of the redistribution of the shear load. The maximum slip was varied in all of the tests and it was determined that for slips of 1 mm, which can occur in long composite beams, the fatigue life can be less than ten thousand cycles.

Further experimental work is needed using the strain-life approach as the outcome would be useful by improving future computer simulations which may lead to simplified mathematical models that can account for this type of inelastic behavior.

2.7 FINITE ELEMENT FOMULATION

This section briefly describes the details of the finite element program (Cheung and Yeo 1975) adopted for the computer simulations forming part of this research work.

2.7.1 Finite element selection

The program uses standard four-noded isoparametric plane stress elements to model the steel and concrete components of the composite beam, which means that the same shape functions are used to define both the geometry and displacement of the elements. There are two orthogonal translational degrees of freedom per node as shown in Fig. 2.17a. An orthogonal set of springs, shown in Fig. 2.17b, is used to model the stiffness of the shear connection along the steel-concrete interface.

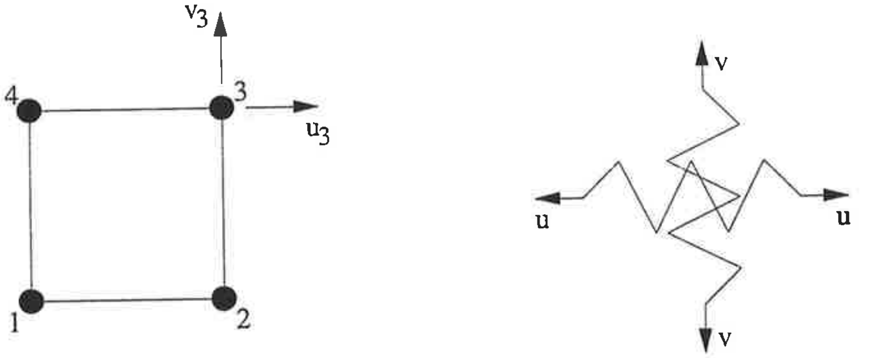

a) four-noded element b) orthogonal spring element

Figure 2.17: Finite elements.

The springs are connected to each corresponding concrete element node and steel element node across the interface as shown in Fig. 2.18, which illustrates a portion of a typical finite element mesh used in the simulations. The vertical spring models the stiffness of the connectors in the direction normal to the interface, while the horizontal spring models the longitudinal shear stiffness of the connectors. As the model of the non-linear behavior of the connection stiffness forms an original development of this research project, the details are given in Chapter 4.

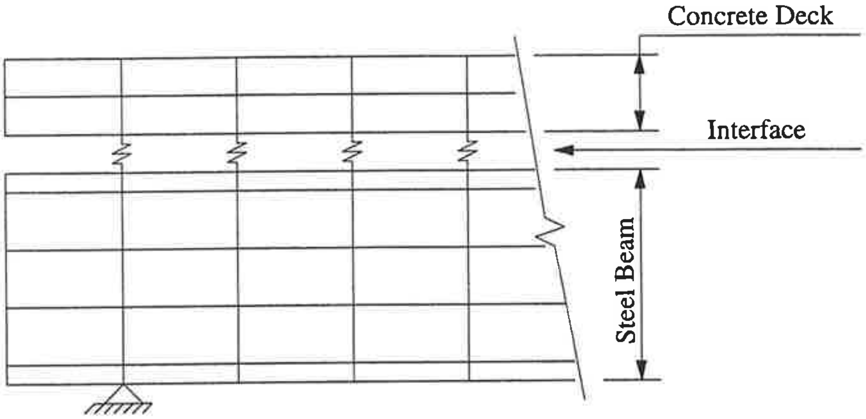

Figure 2.18: Typical finite element mesh.

Proof that the developed finite element program gives realistic results is shown in Chapter 3. Computer simulations are compared with theoretical partial-interaction analyses and very good correlation is obtained.

2.7.2 Component stiffnesses

As it is assumed that the steel and concrete components remain linear-elastic when subjected to fatigue loading, the stiffness of the steel and concrete remains constant throughout the analysis procedure. The stiffness of the steel E_s is user defined and is typically equal to 200000 MPa. The stiffness of the concrete is calculated from the following equation

$$E_c = 5000\sqrt{f_c} \tag{2.63}$$

where f_c is defined by the user in MPa.

The longitudinal shear stiffness of the connectors is calculated using Eq. 2.37 where the parameters required are input by the user. The iterative secant stiffness approach adopted when the non-linear behavior of the shear connection is modeled is discussed in Chapter 4.

2.7.3 Stresses and strains

The following vector defines the three independent strains

$$\{\varepsilon\}=\{\varepsilon_x \;\; \varepsilon_y \;\; \gamma_{xy}\}^T \tag{2.64}$$

where the strains are found from displacements $\{\delta\}$ by

$$\{\varepsilon\}=[B]\{\delta\} \tag{2.65}$$

where $[B]$ is the strain matrix, which is simply the partial derivatives of the shape functions.

The following vector defines the stresses

$$\{\sigma\}=\{\sigma_x \;\; \sigma_y \;\; \tau_{xy}\}^T \tag{2.66}$$

where stresses are determined from the strains by the following expression

$$\{\sigma\}=[D]\{\varepsilon\} \tag{2.67}$$

where $[D]$ is the material stiffness matrix, which for plane stress elements is defined as

$$[D]=\frac{E}{1-\upsilon^2}\begin{bmatrix} 1 & \upsilon & 0 \\ \upsilon & 1 & 0 \\ 0 & 0 & \dfrac{1-\upsilon}{2} \end{bmatrix} \tag{2.68}$$

where υ is Poisson's ratio, which is user defined but is usually taken as 0.15 for concrete and 0.3 for steel.

2.7.4 Element stiffness matrix

The element stiffness matrix for the spring elements is defined as

$$k_{sp} = \begin{bmatrix} E_{sp} & 0 & -E_{sp} & 0 \\ 0 & 1\times10^{10} & 0 & -1\times10^{10} \\ -E_{sp} & 0 & E_{sp} & 0 \\ 0 & -1\times10^{10} & 0 & 1\times10^{10} \end{bmatrix} \tag{2.69}$$

where E_{sp} is the horizontal shear stiffness, which is initially equal to K_{st} given by Eq. 2.37 but varies when a non-linear analysis is performed as, described in Chapter 4. The vertical stiffness is assumed to constant as well and is fixed at the relative large value of 1×10^{10} in order to conform with the linear-elastic partial-interaction assumption that there is no separation between the steel and concrete components.

The element stiffness matrix for the four-noded element is derived from the following integration over the area of the element

$$k_{el} = t\int [B]^{\mathrm{T}}[D][B]\mathrm{d}(area) \tag{2.70}$$

where t is the thickness of the element that is user defined and is obtained from the cross-sectional geometry of the composite beam.

As each of the four-noded and spring element stiffness matrices are determined, they are assembled into the global stiffness matrix $[K]$.

2.7.5 Loading

The current program permits only concentrated loads, which are used to represent the vehicle axle loads traversing the beam longitudinally. As these loads may only be applied at nodal points, they are assembled directly into the global load vector $\{R\}$ and are used to calculate the displacements $\{\delta\}$ given by the following relationship

$$\{R\} = [K]\{\delta\} \tag{2.71}$$

Axle loads are applied to any number of the top row of nodes along the concrete component and can simulate a moving vehicle by moving the loads to the adjacent node (on the right) after each analysis is completed. Dead loads are calculated by the user prior to the simulation and are applied to the top node of each set of spring elements along the length of the beam.

2.7.6 Solution Algorithm

A Bandsolver approach is used to solve the system of finite element equations and integration over the area of the four-noded element is performed by the use of the 2 x 2 gaussian quadrature rule. As in all finite element programs, the user must ensure that the structure is adequately restrained to ensure that rigid body motion is prevented.

Chapter 3

Linear-elastic partial-interaction theory

3.1 INTRODUCTION

Slip occurs because the connectors have a finite stiffness, hence, the connectors must deform before they can begin to carry load, this is known as partial-interaction. As a result, the total range of load resisted by the shear connectors R_{pi} must be less than that predicted from a full-interaction analysis R_{fi}. It will also be shown that computer simulations performing partial-interaction analyses also indicate that R_{fi} is reduced significantly. As the endurance, or fatigue life, of the stud connectors is highly dependent on the total range (Eq. 2.45), even a small reduction in R_{fi} results in a large increase in the fatigue life. This implies that the current design procedure is conservative with respect to the distribution of shear connectors, however, there is a trade-off. The smaller longitudinal shear force acting along the steel-concrete interface implies that the adjacent steel and concrete components are subjected to greater flexural loads than what is currently predicted in order to maintain equilibrium. The greater than anticipated flexural stresses in the steel and concrete can reduce the fatigue life of the components and may potentially result in effects occurring that have not been accounted for in the initial design.

It is, therefore, the purpose of this chapter to present the development of simple relationships that can model the partial-interaction behavior of composite beams, so that the reduction of the longitudinal shear flow resisted by the shear connectors, q_{dowel}, and the change in the steel and concrete stresses can be predicted.

3.2 PARTIAL-INTERACTION SHEAR FLOW

The effect slip has on the shear flow along the steel-concrete interface of a composite bridge beam is discussed in this section. A 50.4 m long simply supported composite beam is used in the analyses, where the cross-section is shown in Fig. 3.1. There is a single row of stud shear connectors uniformly distributed along the length of the beam where d_{sh} = 19 mm, f_u = 450 MPa, f_c = 35 MPa and E_s = 200000 MPa. Two connector distributions were used in the simulations. One is for a more realistic shear connection with one stud located every 100 mm, and the other is for a relatively flexible shear connection where the stiffness is equivalent to placing one stud every 600 mm.

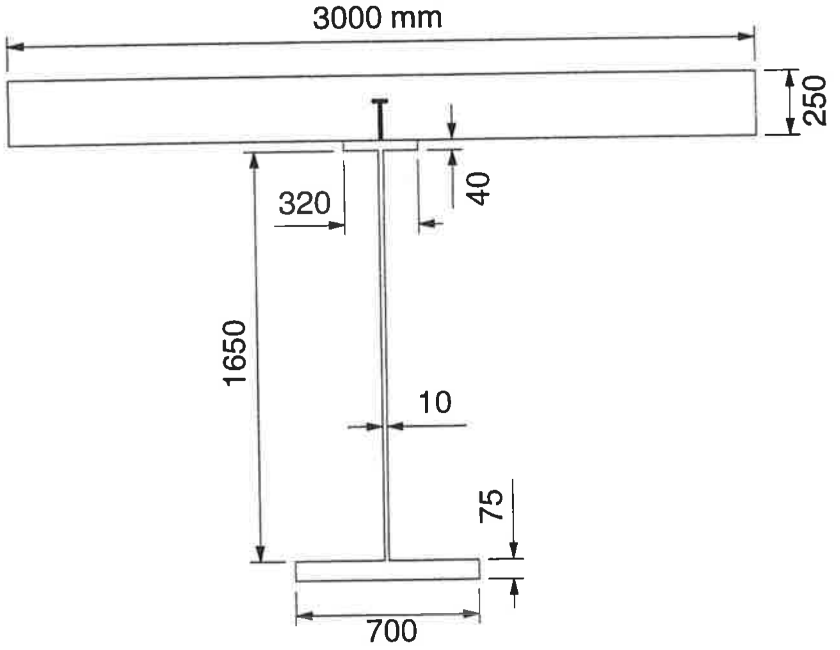

Figure 3.1: Cross-section of 50.4 m long simply supported composite beam.

3.2.1 Shear flow force distribution

Figure 3.2 shows the shear flow force distribution along the steel-concrete interface when a 320 kN concentrated load is applied at the mid-span. The theoretical full-interaction analysis (FIA) distribution is determined from the well known linear-elastic equation given by the first term on the right hand side of Eq

2.61, where, from the cross-sectional geometry of the 50.4 m long composite beam $A_c y/I_{nc}$ = 0.504 x 10^{-3} mm^{-1}. The computer simulation assuming full-interaction, which is accomplished by increasing the connector stiffness to minimize interfacial slip, predicts the shear flow force distribution very well. The discrepancy in the vicinity of the supports and the concentrated load is because a two-dimensional finite element program cannot instantly model a jump in the shear forces - the stresses must build up.

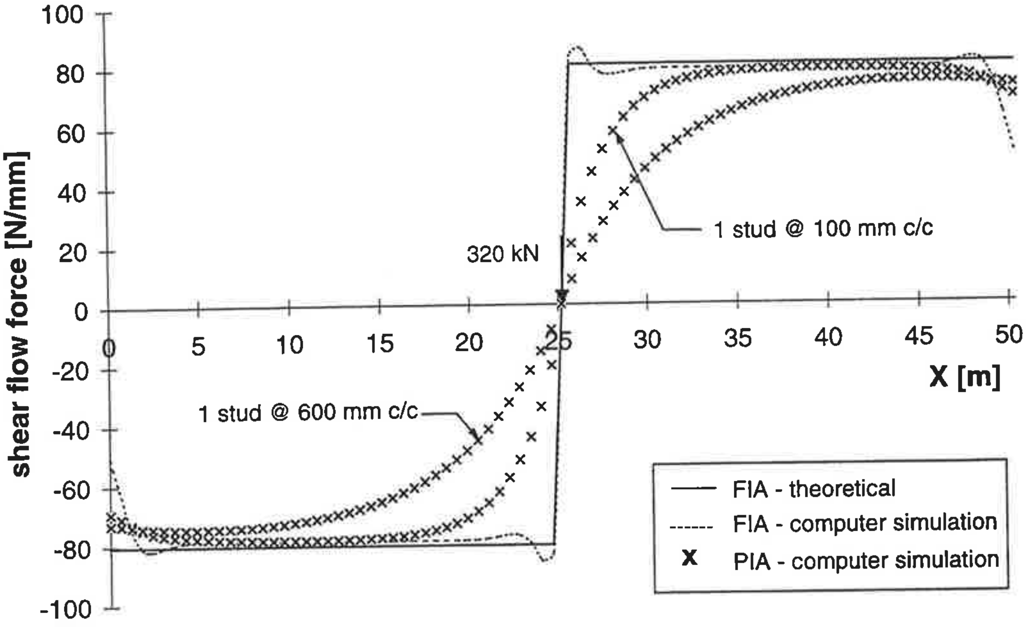

Figure 3.2: Shear flow force distribution for concentrated load at mid-span.

The results of two partial-interaction computer simulations are also shown in Fig. 3.2. As expected, the results are symmetrical, as both the beam and the loading are symmetrical about the center-line. The important observation to make here is that the shear flow force distribution is reduced along the length of the beam when a partial-interaction analysis (PIA) is performed, and that the reduction increases as the stiffness of the shear connection decreases. Reducing the stiffness of the shear connection results in an increase in the interfacial slip.

Similar distributions are obtained for any position of the concentrated load along a simply supported composite beam. Figure 3.3 shows the distribution when the 320 kN concentrated load is located at the quarter-span of the 50.4 m long composite beam. The full-interaction computer simulation distribution again models the theoretical linear-elastic shear flow distribution very well. A reduction in the shear flow force distribution is again observed when a partial-interaction computer simulation is performed, and the reduction increases as the stiffness of the shear connection reduces. As the loading is no longer symmetrically situated on the structure, the location where the shear flow force changes direction, called the transition point, is shifted towards the mid-span of the beam from the loading point as the connection stiffness reduces.

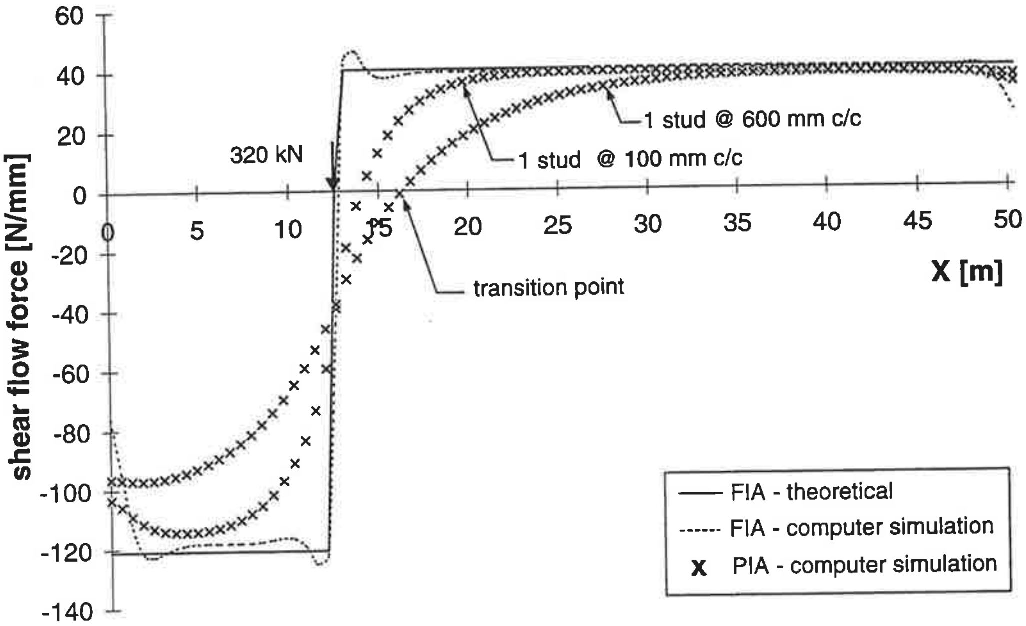

Figure 3.3: Shear flow force distribution for concentrated load at quarter-span.

It was established in Chapter 2 that the fatigue life of stud shear connectors in composite beams is highly dependent on the total range of force applied to the connectors. Hence, it follows that the effect of slip on the total range of load must be investigated in order to determine the impact on the fatigue life of the shear connectors.

Although the reduction of the shear flow force does not appear to be significant, as seen in Figs 3.2 and 3.3, the reduction of the range of load is significant, as described in the following section.

3.2.1.1 *Total range resisted by connectors*

The peak shear flow force envelope shown in Fig. 3.4 is produced by recording the peak positive (global maximum) and peak negative (global minimum) shear flow force along the simply supported composite beam for each design point, as the concentrated load is moved across the span. The total range at a design point *x* is then defined as the difference between the maximum and minimum shear flow force.

As observed in Fig. 3.4, the maximum total range R_{fi} for the case of a single point load traversing a simply supported beam is constant throughout for a full-interaction analysis using linear-elastic theory. Partial-interaction analyses using computer simulations also indicate a constant but reduced maximum total range R_{pi} along the length of the beam, where the reduction is due to the reduction in the shear flow distribution due to partial-interaction described in the previous section. It is also noted that for any location along the beam, the peak unidirectional shear flow force P_{fi} is also reduced to P_{pi} as a result of partial-interaction.

The reduction in both R_{fi} and P_{fi} when partial-interaction analyses are performed has a tremendous impact on the predicted fatigue life of stud shear connectors potentially extending the design life of the bridge.

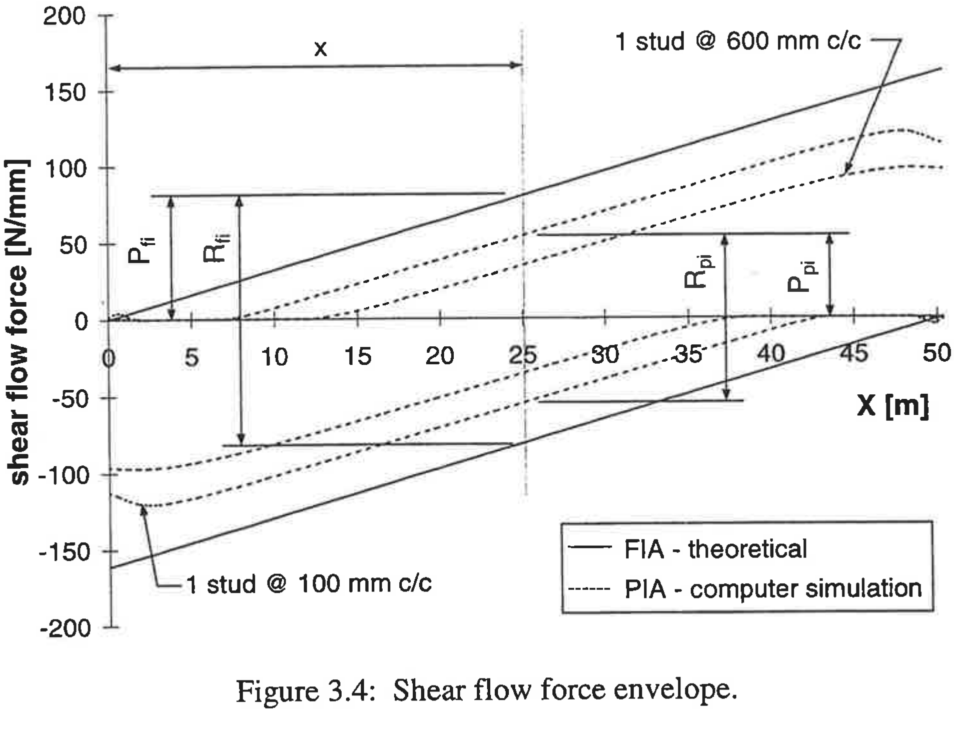

Figure 3.4: Shear flow force envelope.

3.3 SHEAR FLOW REDUCTION

The development of the linear-elastic partial-interaction theory that was started in Section 2.2.1 is now continued where the generic equations for slip and, hence, shear flow are developed in a form suitable for deriving the simplified approach in the next section.

3.3.1 Generic equations

As the slip, *s*, in Eq. 2.34 is a function of V^*, the distribution of *s* along the entire length of the composite beam must be defined by two equations, one for each shear span. As shown in Fig. 3.5, *l* and *V* define the length of the shear span and the vertical shear force in the shear span respectively, where the subscripts *1* and *2* refer to the left and right shear spans respectively.

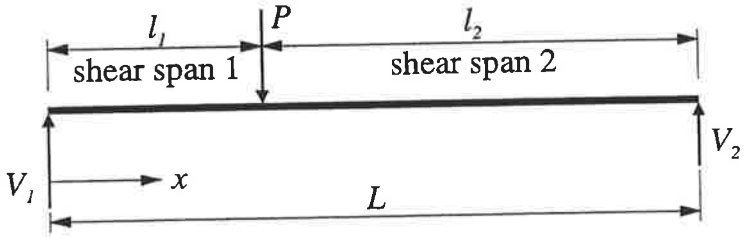

Figure 3.5: Definition of shear spans.

Four integration constants are required, two for each shear span; K_A and K_B for shear span *1*, and K_C and K_D for shear span 2. Similarly, the following four boundary conditions are necessary to solve for the four integration constants

$$\frac{ds_1}{dx} = 0, \ @ \ x = 0 \tag{3.1}$$

$$\frac{ds_2}{dx} = 0, \ @ \ x = L \tag{3.2}$$

$$\frac{ds_1}{dx} = \frac{ds_2}{dx}, \ @ \ x = l_1 \tag{3.3}$$

$$s_1 = s_2, \ @ \ x = l_1 \tag{3.4}$$

where the slip strain *ds/dx* is derived by differentiating Eq. 2.34 with respect to x to give the following

$$\frac{ds}{dx} = \alpha K_1 \cosh(\alpha x) + \alpha K_2 \sinh(\alpha x) \qquad (3.5)$$

Solving the resulting system of equations simultaneously gives the following four integration constants

$$K_A = 0 \qquad (3.6)$$

$$K_B = \beta P\left[\cosh(\alpha l_1) - \sinh(\alpha l_1)\coth(\alpha L)\right] \qquad (3.7)$$

$$K_C = \beta P \sinh(\alpha l_1) \qquad (3.8)$$

$$K_D = -\beta P \sinh(\alpha l_1)\coth(\alpha L) \qquad (3.9)$$

Substituting the four integration constants into Eq. 2.34 gives the two equations required to model the distribution of slip along the length of a simply supported composite beam for a given concentrated load located a distance l_1 from the left support

$$s_1 = \beta P\left[\cosh(\alpha l_1) - \coth(\alpha L)\sinh(\alpha l_1)\right]\cosh(\alpha x) - \beta V_1 \qquad (3.10)$$

and

$$s_2 = \beta P\left[\sinh(\alpha x) - \coth(\alpha L)\cosh(\alpha x)\right]\sinh(\alpha l_1) + \beta V_2 \qquad (3.11)$$

where s_1 and s_2 are the distributions of slip within shear spans *1* and *2* respectively, and P, V_1 and V_2 are all taken as positive.

The distribution of longitudinal shear flow force is obtained simply by substituting Eq. 2.5 into Eqs 3.10 and 3.11 to give the following

$$(q_{dowel})_1 = \frac{k}{p}\{\beta P[\cosh(\alpha l_1) - \coth(\alpha L)\sinh(\alpha l_1)]\cosh(\alpha x) - \beta V_1\} \tag{3.12}$$

and

$$(q_{dowel})_2 = \frac{k}{p}\{\beta P[\sinh(\alpha x) - \coth(\alpha L)\cosh(\alpha x)]\sinh(\alpha l_1) + \beta V_2\} \tag{3.13}$$

Figure 3.6 compares the shear flow force distribution predicted by the computer simulation, for the case where the 320 kN concentrated load is located at the quarter-span of the 50.4 m long composite beam, with the theoretical shear flow force distribution given by Eqs 3.12 and 3.13. The stiffness of the shear connection used in the analysis is such that k = 54720 Nmm^{-1} and p = 600 mm. As the force P = 320 kN is located at the quarter-span: l_1 = 12.6 m; V_1 = 240 kN; and V_2 = 80 kN as L = 50.4 m. The remaining parameters, α and β, are equal to 0.183x10^{-3} mm^{-1} and 5.53x10^{-6} mmN^{-1} respectively.

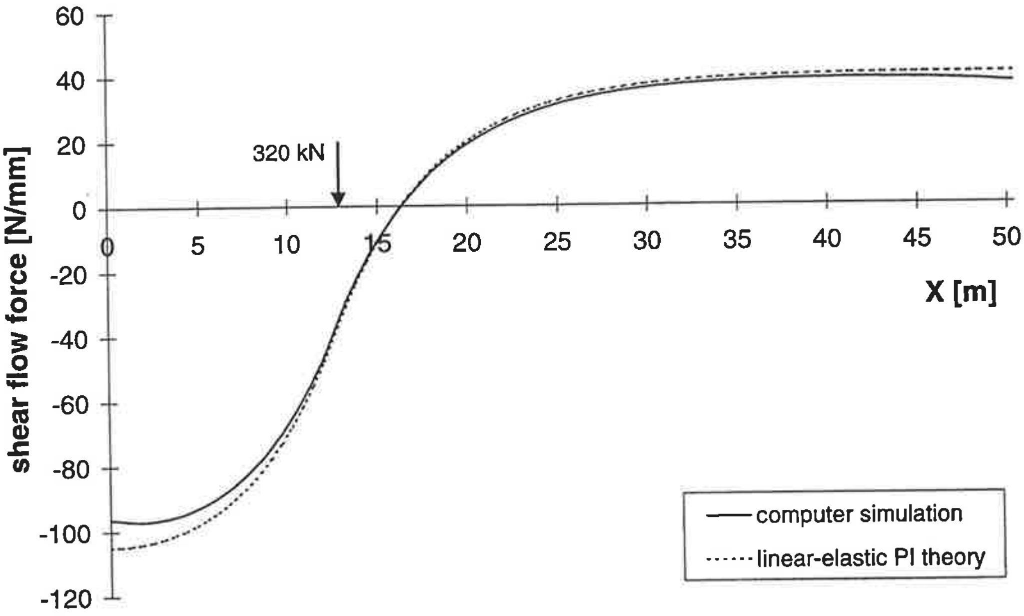

Figure 3.6: Comparison of shear flow force distributions.

Figure 3.6 shows that the agreement between the theoretical and computed partial-interaction shear flow force distributions are very good. It follows then that the next stage in the development is to quantify the reduction in the partial-interaction shear flow force distribution with respect to the full-interaction distribution.

3.3.2 Quantifying the reduction in the shear flow force distribution

It is important to be able to quantify the reduction in R_{fi} and P_{fi} due to partial-interaction so that a better estimate of the fatigue life of the shear connectors can be made. The expression for the reduction factor RF_R for R_{fi} is developed next, which is then followed by the development for the reduction factor RF_P for P_{fi}.

3.3.2.1 *Reduction of the total range*

The two locations of the traversing concentrated load that results in the maximum and minimum P_{pi} for a design point x is determined by differentiating Eqs 3.12 and 3.13 with respect to l_1 and equating to zero. The equations modeling the distribution of slip (Eqs 3.10 and 3.11) can be used instead of the equations for the distribution of the shear flow force because they only differ by the constant factor k/p and the resulting derivatives are equated to zero.

Two cases, as shown in Fig. 3.7, must be considered depending on which side of the concentrated load the design point is located. The term $(l_1)_2$ in Fig. 3.7a defines the location of P, where the subscript *2* refers to the design point being in shear span *2* to obtain the maximum positive slip $(s_2)_{max}$, hence, the maximum shear flow force at x. Similarly, $(l_1)_1$ in Fig. 3.7b defines the location of P, where the subscript *1* outside the brackets refers to the design point being in shear span *1*, to give the maximum negative slip $(s_1)_{max}$ at x.

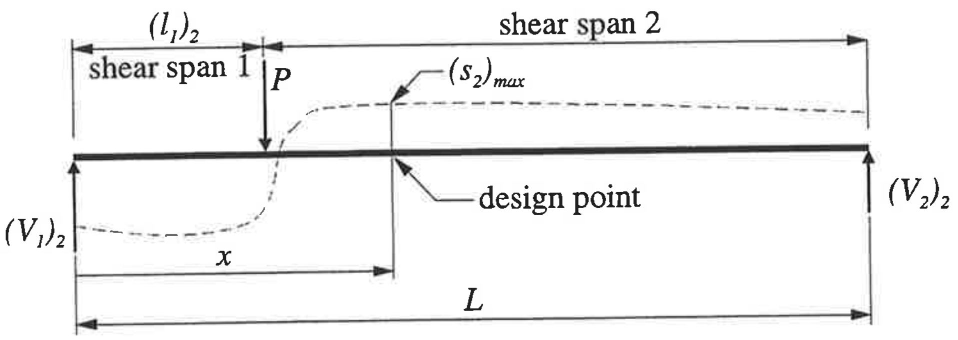

(a) CASE 1

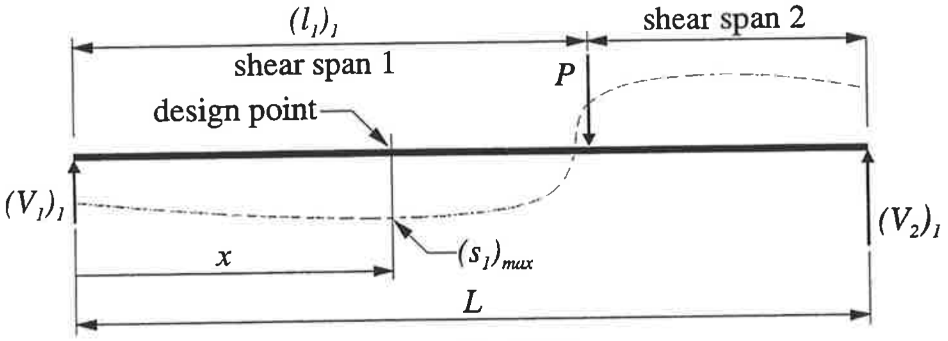

(b) CASE 2

Figure 3.7. Two cases required to develop R_{pi}.

The location $(l_1)_2$ is found by substituting

$$(V_2)_2 = \frac{(l_1)_2 P}{L} \tag{3.14}$$

obtained from equilibrium in Fig. 3.7a, into Eq. 3.11 giving

$$s_2 = \beta P[\sinh(\alpha x) - \coth(\alpha L)\cosh(\alpha x)]\sinh[\alpha(l_1)_2] + \frac{\beta(l_1)_2 P}{L} \tag{3.15}$$

and differentiating Eq. 3.15 with respect to $(l_1)_2$ to give

$$\frac{ds_2}{d(l_1)_2} = \alpha\beta P[\sinh(\alpha x) - \coth(\alpha L)\cosh(\alpha x)]\cosh[\alpha(l_1)_2] + \frac{\beta P}{L} \tag{3.16}$$

Then, equating Eq. 3.16 to zero and solving for $(l_1)_2$ gives the following expression for the location of the concentrated load that results in the maximum positive slip $(s_2)_{max}$

$$(l_1)_2 = \frac{1}{\alpha}\cosh^{-1}\left\{\frac{-1}{\alpha L\left[\sinh(\alpha x) - \coth(\alpha L)\cosh(\alpha x)\right]}\right\} \tag{3.17}$$

where $0 \le (l_1)_2 < x$.

Similarly, $(l_1)_1$ is found by substituting

$$(V_1)_1 = P - \frac{(l_1)_1 P}{L} \tag{3.18}$$

obtained from equilibrium in Fig. 3.7b, into Eq. 3.10 giving

$$s_1 = \beta P\{\cosh[\alpha(l_1)_1] - \coth(\alpha L)\sinh[\alpha(l_1)_1]\}\cosh(\alpha x) - \beta P\left[1 - \frac{(l_1)_1}{L}\right] \tag{3.19}$$

and differentiating Eq. 3.19 with respect to $(l_1)_1$ to give

$$\frac{ds_1}{d(l_1)_1} = \alpha\beta P\{\sinh[\alpha(l_1)_1] - \coth(\alpha L)\cosh[\alpha(l_1)_1]\}\cosh(\alpha x) + \frac{\beta P}{L} \tag{3.20}$$

where the term $(l_1)_1$ cannot be isolated when Eq. 3.20 is equated to zero because of the $\coth(\alpha L)$ term. However, if we assume that $\coth(\alpha L)$ is equal to unity, which will be justified subsequently, the following expression for $(l_1)_1$ is found which locates the position of the concentrated load to give the maximum negative slip $(s_1)_{max}$

$$(l_1)_1 \approx \frac{-1}{\alpha}\ln\left[\frac{1}{\alpha L\cosh(\alpha x)}\right] \tag{3.21}$$

where $x < (l_1)_1 \leq L$.

The validity of the assumption that coth(αL) = *1* is shown in Table 3.1 where the magnitude of coth(αL) for a number of beams and connector distributions is given. As αL increases, coth(αL) approaches *1* and the error resulting from the assumption made to develop Eq. 3.21 diminishes. It can be deduced that the longer the beam and/or the stiffer the shear connection, the more accurate the estimate of $(l_1)_1$ will be.

Table 3.1: Magnitude of coth(αL).

L [m]	connector distribution	α (x10^{-3}) [mm^{-1}]	αL	coth(αL)
6	1 @ 500 mm	0.537	3.222	1.003
6	1 @ 250 mm	0.759	4.554	1.0002
20	3 @ 240 mm	0.455	9.107	1.00000003
20	3 @ 120 mm	0.644	12.88	1.0
50.4	1 @ 600 mm	0.183	9.223	1.00000002
50.4	1 @ 100 mm	0.449	22.63	1.0

Now that $(l_1)_2$ and $(l_1)_1$ are known, the maximum range R_{pi} at a design point x can be determined using the following relationship

$$R_{pi} = (q_{dowel})_2 - (q_{dowel})_1 \tag{3.22}$$

where $(q_{dowel})_2$ is given by Eq 3.13 with $l_1 = (l_1)_2$, and $(q_{dowel})_1$ is given by Eq. 3.12 with $l_1 = (l_1)_1$.

As the stiffness of the connection approaches infinity, Eq. 3.22 approaches R_{fi} where the assumption is that there is no slip along the interface, so that the reduction factor RF_R at a design point x can be derived from the following

$$RF_R = \frac{(R_{pi})_k}{(R_{pi})_\infty} \tag{3.23}$$

where the numerator is obtained from Eq. 3.22 using the realistic connector stiffness k, and the denominator is also derived from Eq. 3.22 by taking the limit as $k \rightarrow \infty$. As k approaches ∞, α in Eq. 2.31 also approaches ∞, and both $(l_1)_2$ and $(l_1)_1$ approach x. When there is full-interaction, the maximum shear flow at a design point x occurs when the load is applied at the design point so that taking the limit of Eq. 3.22 as $k \rightarrow \infty$ yields the following

$$\left(R_{pi}\right)_\infty \propto P \tag{3.24}$$

Substituting Eqs 3.22 and 3.24 into Eq. 3.23 gives the following expression for the reduction factor after simplification

$$\begin{aligned} RF_R = {} & [\sinh(\alpha x) - \coth(\alpha L)\cosh(\alpha x)]\sinh[\alpha(l_1)_2] - \\ & \{\cosh[\alpha(l_1)_1] - \coth(\alpha L)\sinh[\alpha(l_1)_1]\}\cosh(\alpha x) + \frac{(l_1)_2 - (l_1)_1}{L} + 1 \end{aligned} \tag{3.25}$$

where $(l_1)_1$ is given by Eq. 3.21 and $(l_1)_2$ by Eq. 3.17.

The distribution of RF_R from the mathematical model of Eq. 3.25 is shown in Fig. 3.8 for two distributions of shear connectors along the 50.4 m long composite beam. The reduction in R_{fi} from computer simulations is also shown in order to validate the mathematical model. The agreement is very good and the mathematical model is slightly conservative throughout.

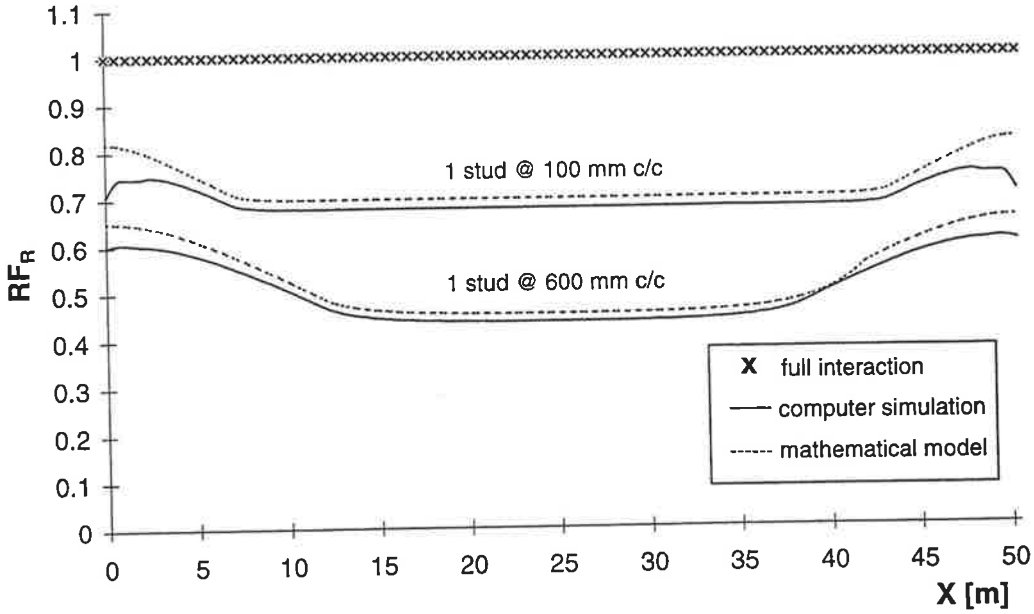

Figure 3.8: Distribution of RF_R.

3.3.2.2 *Reduction of the peak unidirectional shear flow force*

As the maximum unidirectional shear flow force is also required to assess fatigue damage (Eq. 2.60), the reduction of P_{fi} due to partial-interaction must also be considered. As before, the two cases in Fig. 3.7 must be accounted for depending on the direction of the shear flow.

Considering Case 1 first in Fig. 3.7a, the reduction factor can be defined as

$$(RF_P)_2 = \frac{(q_{dowel})_{2,k}}{(q_{dowel})_{2,\infty}} \tag{3.26}$$

where $(q_{dowel})_2$ is given by Eq. 3.13 with $l_1 = (l_1)_2$. The numerator of Eq. 3.26 is obtained by using the realistic connector stiffness k, and the denominator is determined by taking the limit of Eq. 3.13 as k approaches ∞. As before, when k approaches ∞, α in Eq. 2.31 also approaches ∞, and $(l_1)_2$ approaches x for a design point at x, so that taking the limit of Eq. 3.13 as $k \rightarrow \infty$ yields the following

$$(q_{dowel})_{2,\infty} \propto \frac{xP}{L} \tag{3.27}$$

Substituting Eqs 3.13 and 3.27 into Eq. 3.26 gives the following expression for the reduction factor after simplification

$$(RF_P)_2 = \frac{L}{x}\left\{[\sinh(\alpha x)-\coth(\alpha L)\cosh(\alpha x)]\sinh[\alpha(l_1)_2]+\frac{(l_1)_2}{L}\right\} \tag{3.28}$$

Similarly for Case 2 in Fig. 3.7b, the reduction factor is defined as

$$(RF_P)_1 = \frac{(q_{dowel})_{1,k}}{(q_{dowel})_{1,\infty}} \tag{3.29}$$

where $(q_{dowel})_1$ is given by Eq. 3.12 with $l_1 = (l_1)_1$. The numerator of Eq. 3.29 is obtained by using the realistic connector stiffness k, and the denominator is found by taking the limit of Eq. 3.12 as k approaches ∞. As before, α in Eq. 2.31 approaches ∞ and $(l_1)_1$ approaches x for a design point at x so that when taking the limit of Eq. 3.12 as $k \rightarrow \infty$, the following relationship is found

$$(q_{dowel})_{1,\infty} \propto P\left(-1+\frac{x}{L}\right) \tag{3.30}$$

Substituting Eqs 3.12 and 3.30 into Eq. 3.29 gives the following expression for $(RF_P)_1$ after simplification

$$(RF_P)_1 = \frac{L}{x-L}\left\{[\cosh[\alpha(l_1)_1]-\coth(\alpha L)\sinh[\alpha(l_1)_1]]\cosh(\alpha x)-1+\frac{(l_1)_1}{L}\right\} \tag{3.31}$$

Figure 3.9 shows the distributions of $(RF_P)_2$ and $(RF_P)_1$ along the 50.4 m long composite beam resulting from the traversal of a 320 kN concentrated load. The reduction of P_{fi} from a computer simulation is also shown. The agreement between the mathematical models of Eqs 3.28 and 3.31 and the computer simulation is again very good. It is important to note that for fatigue the governing peak shear flow force at a design point is the one that results in the larger P_{pi}.

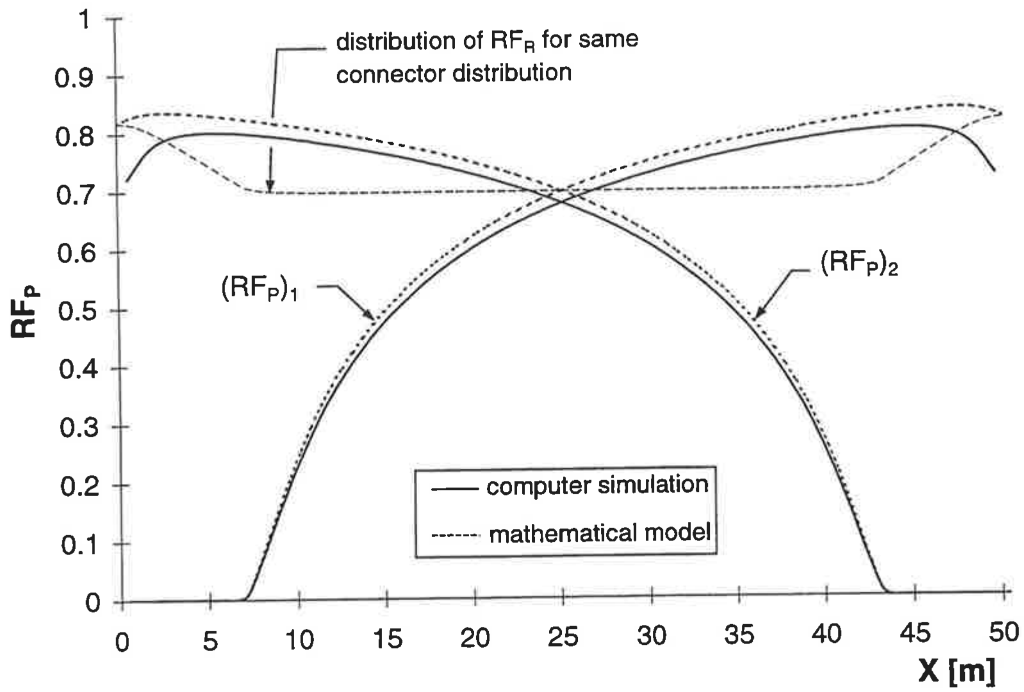

Figure 3.9: Distribution of $(RF_P)_1$ and $(RF_P)_2$.

The distribution of RF_R in Fig. 3.8 is also superimposed on Fig. 3.9 where it can be seen that the reduction factors for P_{fi} and R_{fi} intersect at the supports and at the mid-span. This is expected because when the design point is at the support R_{pi} is equal to P_{pi}, as shown in Fig. 3.4, which results in the same reduction factors at the supports. When the design point is at the mid-span, the absolute value of the positive and negative P_{pi} are equal, again seen in Fig. 3.4, which also results in the same reduction factor as for R_{pi} at the mid-span.

3.4 SIMPLIFICATION OF THE REDUCTION FACTORS

The mathematical models developed to determine the distribution of R_{pi} and P_{pi} are too involved to be used in everyday design or assessment situations. The following section proposes a set of simplified equations that have been developed by making some simplifying assumptions without significantly reducing the accuracy of the predictions.

3.4.1 Simplification of the total range reduction factor

The distribution of RF_R in Fig. 3.8 is symmetrical about the mid-span of the simply supported composite beam such that it is a maximum at the supports from where it gradually reduces until a relatively constant reduction is maintained over the mid-span of the beam. The idealization proposed determines the reduction factor at the supports $(RF_R)_s$ and the location along the beam l_c where the reduction factor becomes constant at $(RF_R)_c$. Straight line segments, as shown in Fig. 3.10, connect these points.

The simplified relationship for the peak RF_R at the left support is given by the following expression obtained by substituting $x = 0$ and $(l_1)_2 = 0$ into Eq. 3.25

$$(RF_R)_s = 1 - \frac{(l_1)_1}{L} - \{\cosh[\alpha(l_1)_1] - \coth(\alpha L)\sinh[\alpha(l_1)_1]\} \tag{3.32}$$

where by substituting $x = 0$ into Eq. 3.21, $(l_1)_1$ is given by the following

$$(l_1)_1 = \frac{-1}{\alpha}\ln\left(\frac{1}{\alpha L}\right) \tag{3.33}$$

If the assumption that $\coth(\alpha L) = 1$ is again used, the last term of Eq. 3.32 can be simplified, and by substituting Eq. 3.33 into Eq. 3.32, the following simple expression can be used to estimate RF_R at the supports

$$(RF_R)_s = 1 + \frac{1}{\alpha L}\ln\left(\frac{1}{\alpha L}\right) - \frac{2}{(\alpha L)^2 + 1} \tag{3.34}$$

which is now only a function of the parameter α (Eq. 2.31) and the total length of the beam L.

As the distribution of RF_R is constant when $(l_1)_2$ is greater the zero, the point l_c in Fig. 3.10 defines the location where RF_R first becomes constant so that substituting $(l_1)_2 = 0$ and $x = l_c$ into Eq. 3.17 yields the following equality

$$\cosh^{-1}\left\{\frac{-1}{\alpha L[\sinh(\alpha l_c)-\coth(\alpha L)\cosh(\alpha l_c)]}\right\}=0 \tag{3.35}$$

As $\cosh^{-1}(\theta) = 0$ when $\theta = 1$, and again using the assumption that $\coth(\alpha L) = 1$, l_c in Eq. 3.35 can be isolated giving the following expression

$$l_c = \frac{-1}{\alpha}\ln\left(\frac{1}{\alpha L}\right) \tag{3.36}$$

The constant magnitude of RF_R that is $(RF_R)_c$ in Fig. 3.10 is also found by substituting $x = l_c$ and $(l_1)_2 = 0$ into Eq. 3.25 giving

$$(RF_R)_c = 1-\frac{(l_1)_1}{L}-\{\cosh[\alpha(l_1)_1]-\coth(\alpha L)\sinh[\alpha(l_1)_1]\}\cosh(\alpha l_c) \tag{3.37}$$

where after substituting $x = l_c$ into Eq. 3.21, $(l_1)_1$ is given by the following

$$l_{1,1} = \frac{-1}{\alpha}\ln\left[\frac{1}{\alpha L\cosh(\alpha l_c)}\right] \tag{3.38}$$

By substituting Eqs 3.36 and 3.38 into Eq. 3.37 and by making use of the assumption that $\coth(\alpha L) = 1$, Eq. 3.37 can be simplified to yield the following simplified expression for the constant RF_R at l_c

$$(RF_R)_c = 1+\frac{1}{\alpha L}\left\{\ln\left[\frac{2}{(\alpha L)^2+1}\right]-1\right\} \tag{3.39}$$

which is also only a function of α (Eq. 2.31) and L.

The various approaches are compared in Fig. 3.10 where is can be seen that the loss of accuracy, when using the simplified model, is minimal and any differences are conservative, which is acceptable from the point of view of the fatigue life of the shear connectors.

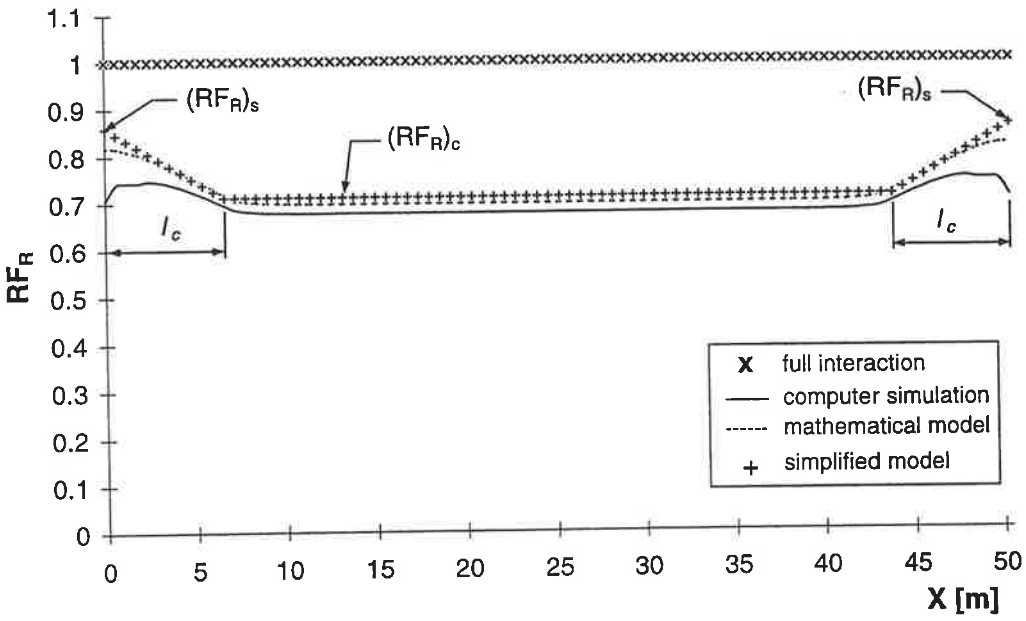

Figure 3.10: Example of simplified model of RF_R.

3.4.2 Simplification of the peak unidirectional shear flow force reduction factor

As previously illustrated in Fig. 3.9, the distribution of RF_P coincides with the distribution of RF_R at the supports and at the mid-span. Therefore, the proposed simplified model of RF_P uses $(RF_R)_s$ at the supports (Eq. 3.34) and $(RF_R)_c$ at the mid-span (Eq. 3.39) connected by straight line segments as shown in Fig. 3.11. Figure 3.11 shows the distribution of RF_P from Fig. 3.9 and superimposes the distribution of the proposed simplified model, where the critical reduction factors, at the supports and the mid-span, are determined using $(RF_R)_s$ and $(RF_R)_c$ respectively.

The reduction of P_{fi} due to partial-interaction is overestimated along some portions of the beam, such as within A-A and B-B in Fig. 3.11, resulting in a slightly unconservative estimate of P_{pi}. The effect on the fatigue life of the connectors is minimal, as will be shown in the example given in Section 3.9.

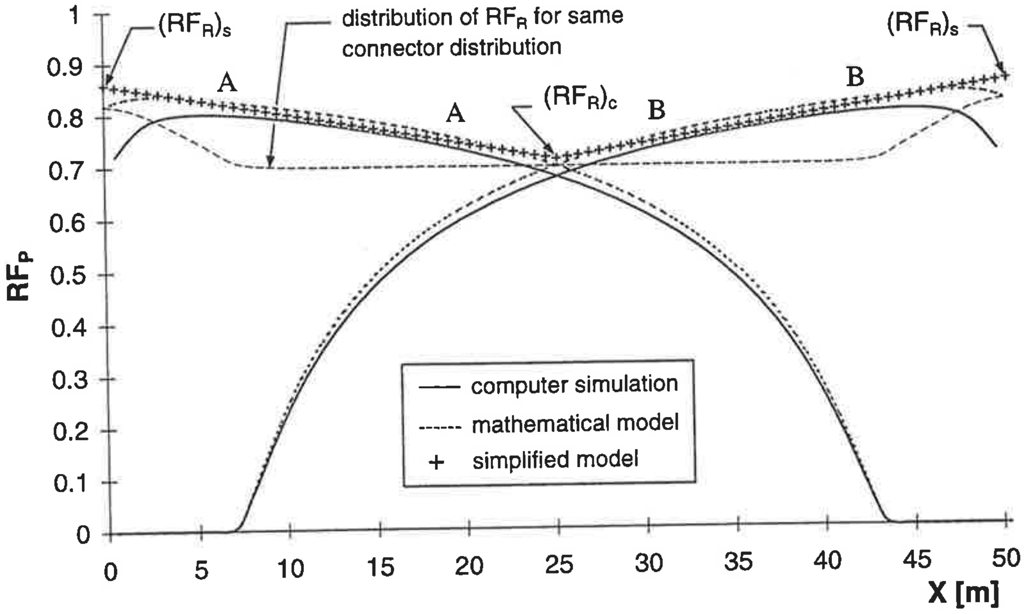

Figure 3.11: Example of simplified model of RF_P.

3.4.3 Validation of the simplified model

The preceding comparisons were limited to the 50.4 m long composite beam with a uniform distribution of connectors. The simplified model using Eqs 3.34, 3.36 and 3.39 is also compared to computer simulations for a 20 m and 6 m long simply supported composite beam.

The details of the cross-section of the 20 m long beam is shown in Fig. 3.12 where the connector distribution and the cross-sectional geometry is such that $\alpha = 0.644 \times 10^{-3}$ mm^{-1}.

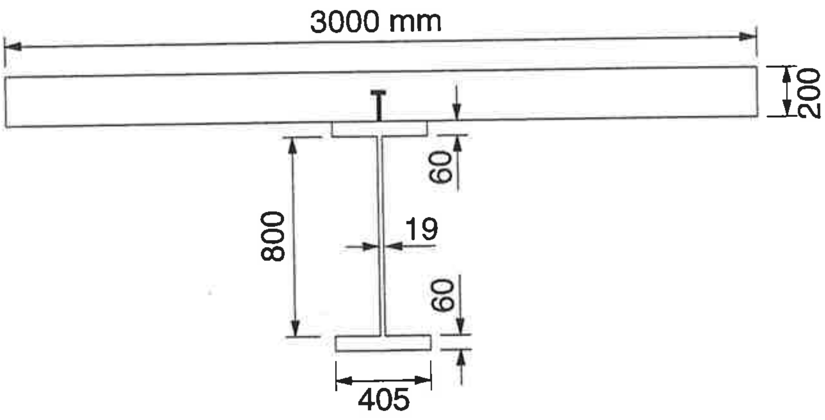

Figure 3.12: Cross-section of 20 m long simply supported composite beam.

The cross-section of the 6 m long simply supported composite beam is shown in Fig. 3.13 where the connector distribution and the cross-sectional geometry is such that $\alpha = 0.759 \times 10^{-3}$ mm^{-1}.

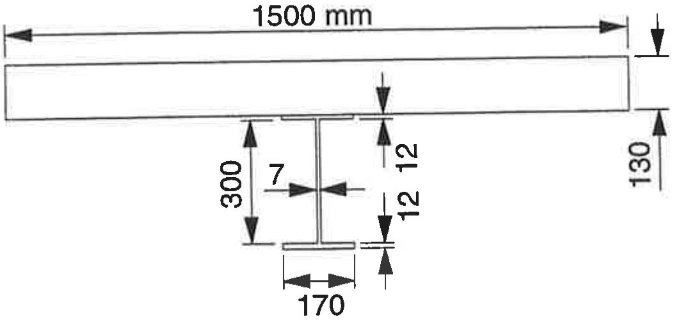

Figure 3.13: Cross-section of 6 m long simply supported composite beam.

Figure 3.14 compares the distribution of RF_R using the simplified model with that of the computer simulations and the mathematical model for the 20 m beam. As was the case with the 50.4 m beam (Fig. 3.10) the agreement between the computer simulation and the mathematical model is very good, the simplified model being conservative over the length of the beam.

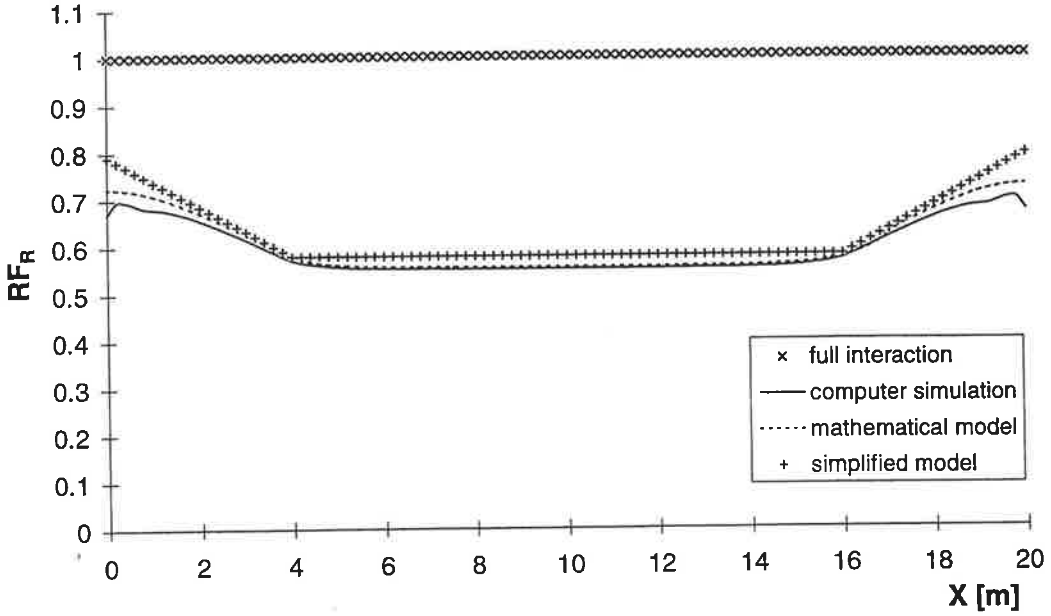

Figure 3.14: Comparison of RF_R for the 20 m beam.

Figure 3.15 compares the distribution of RF_R using the simplified model with that of the computer simulations and the mathematical model for the 6 m beam. The mathematical model again agrees very well with the results of the computer simulation, as does the simplified model. However, the discrepancy between the simplified model and the mathematical model is slightly greater for this beam, the reason being that the error resulting from the assumption that $\coth(\alpha L) = 1$ is greatest for this relatively short beam as can be seen in Table 3.1.

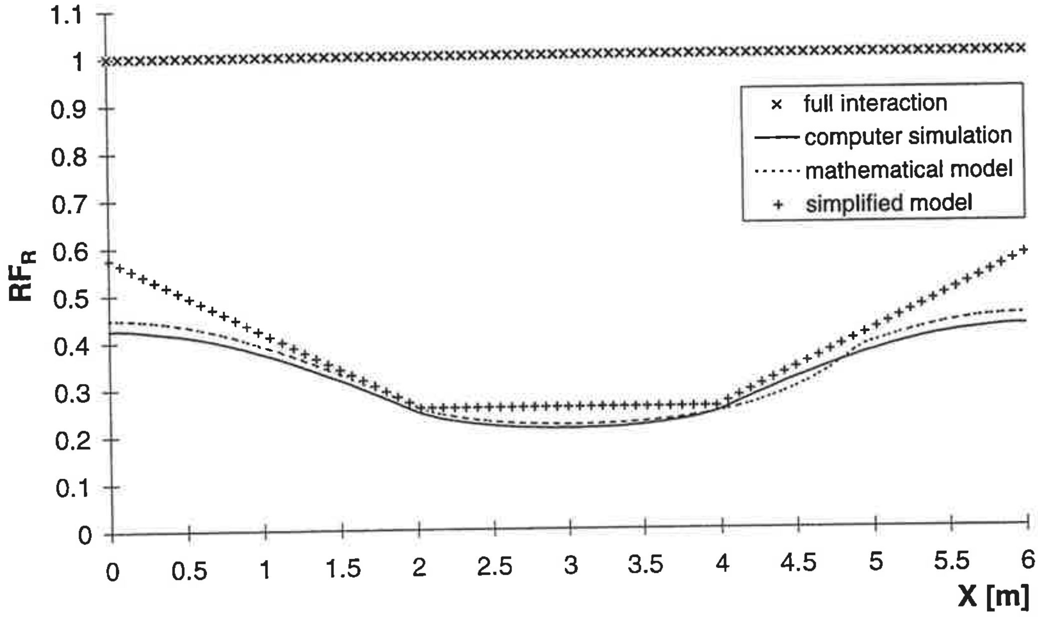

Figure 3.15: Comparison of RF_R for the 6 m beam.

Similarly, Fig. 3.16 compares the distribution of RF_P using the simplified model with that of the computer simulations and the mathematical model for the 20 m beam. The agreement between the mathematical model and the computer simulation is again very good. As was the case with the 50.4 m beam (Fig. 3.11), the simplified model is also slightly unconservative over two areas of the beam within A-A and B-B in Fig. 3.16. As before, however, the relatively small discrepancy will have a minimal effect on the change in the fatigue life of the connectors.

Finally, Fig. 3.17 compares the distribution of RF_P using the simplified model with that of the computer simulations and the mathematical model for the 6 m beam. The agreement between the mathematical model and the computer simulation is again very good. The simplified model is also acceptable, again slightly overestimating the reduction of P_{fi} within points A-A and B-B in Fig. 3.17. The error between the simplified model and the mathematical model is greater than that observed for the 20 m beam (Fig. 3.16) resulting from the greater deviation from the assumption that $\coth(\alpha L) = 1$, again due to the relatively short span length of this beam.

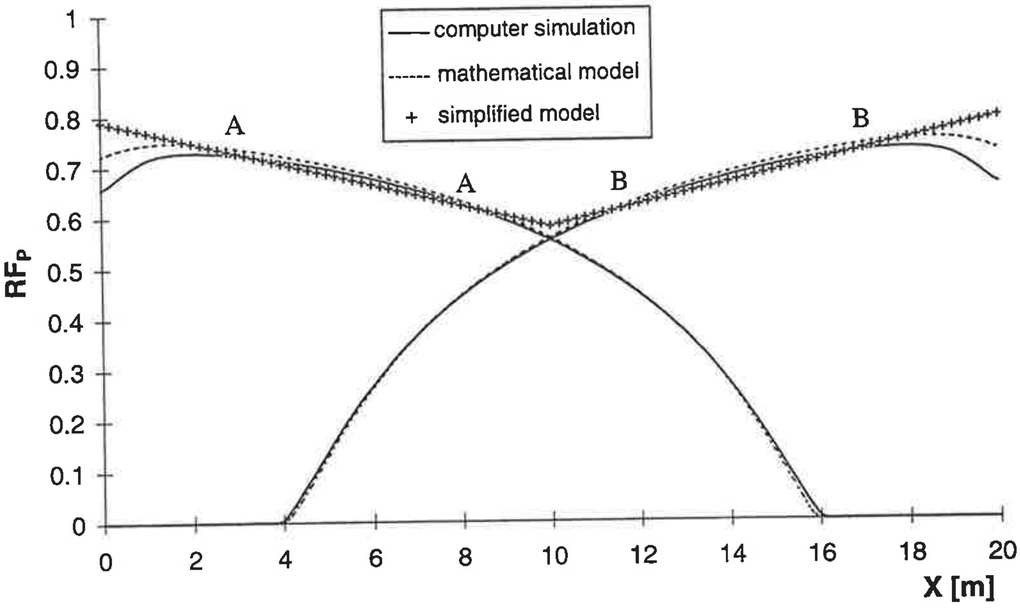

Figure 3.16: Comparison of RF_P for the 20 m beam.

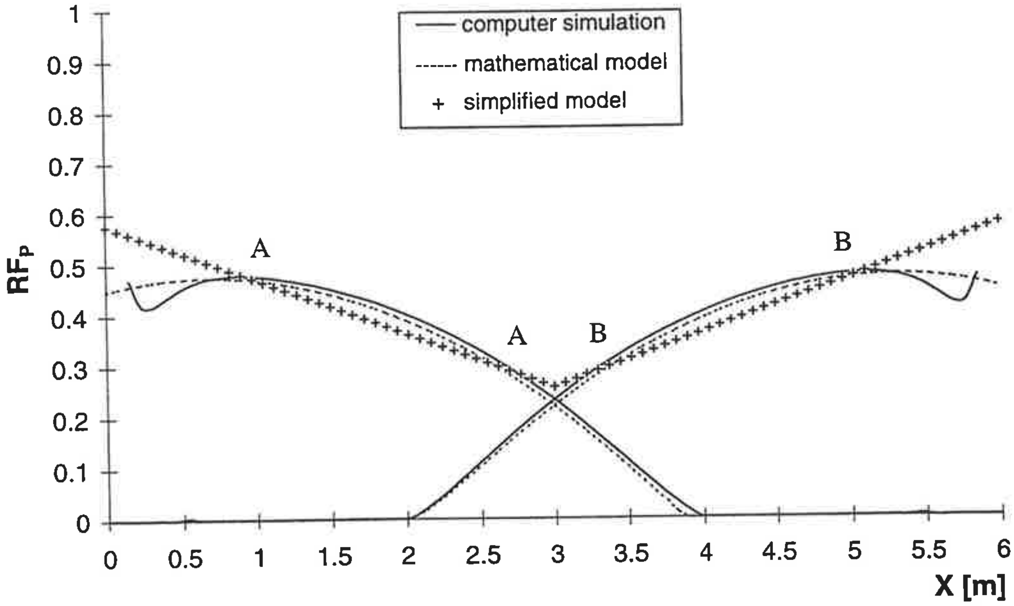

Figure 3.17: Comparison of RF_P for the 6 m beam.

3.5 STRAIN DISTRIBUTION BOUNDS

As the effect of partial-interaction on the shear flow forces has been quantified, the remainder of this chapter concentrates on the effect of partial-interaction on the flexural stresses by first investigating the change in the strain distribution at a point along the beam under a given load condition.

Two extremes or bounds exist with regards to the strain distributions at a section: one bound occurs when the connector stiffness is infinite, known as full-interaction; and the other bound results from an analysis where the connector stiffness is zero, known as no-interaction. The assumption that there is no separation between the steel and concrete components is made in both the full-interaction and no-interaction analyses, hence, the steel and concrete curvatures at a section are assumed to be the same. It follows then that the partial-interaction strain distribution, where the shear connectors have a finite stiffness, must lie between these two boundaries depending on the magnitude of the connection stiffness.

The linear-elastic strain distribution at any point along a beam can be defined by determining the curvature and the location of the centroid. The curvature ϕ can be found by using the following well known relationship

$$\phi_i = \frac{M_i}{EI} \tag{3.40}$$

where the subscript i refers to the location of the section along the beam, and EI is the flexural stiffness.

As we are dealing with composite steel and concrete beams, the flexural stiffness is dependent on the properties of both the steel and concrete such that for full-interaction $EI_{fi} = E_c I_{nc}$, and for no-interaction $EI_{ni} = (EI)_c + (EI)_s$ (Oehlers and Bradford 1995) where the subscripts c and s refer to the concrete and steel components respectively.

The 50.4 m simply supported composite beam with a uniform distribution of connectors (Fig. 3.1) is again used to illustrate the various strain distributions discussed. A single concentrated load of 320 kN is located at the mid-span, and the strain distributions shown are for a section located 24 m from the support such that the bending moment M = 3840 kNm. The material properties and cross-sectional geometry of the section are such that EI_{fi} = 26.4x10^{15} Nmm^2 and EI_{ni} = 7.60x10^{15} Nmm^2, and substitution into Eq. 3.40 yields the following curvatures at the design point; ϕ_{fi} = 0.146x10^{-6} mm^{-1} and ϕ_{ni} = 0.505x10^{-6} mm^{-1}. The centroid of the transformed concrete section for the full-interaction distribution $\bar{y}_{nc}$ is located in the steel component 474 mm below the steel-concrete interface. The no-interaction distribution passes through the centroid of each component, where $\bar{y}_c$ = 125 mm and $\bar{y}_s$ = 1290 mm, both with respect to the location of the steel-concrete interface. Having defined the curvatures and centroids for the two boundary conditions, the strain distributions can be determined as shown in Fig. 3.18 where negative is taken as compression. Figure 3.18 also shows the strain distribution obtained from a partial-interaction computer simulation for a uniform longitudinal connector distribution equivalent to 1 connector every 600 mm.

The two points where the boundary strain distributions intersect in Fig. 3.18 are of special interest as every strain distribution must theoretically pass through these points regardless of the connector stiffness. The points are defined as Partial-Interaction Focal Points and are labeled PIFP$_s$ and PIFP$_c$, where the subscripts s and c refer to the focal point in the steel and concrete components respectively. It will be shown that it is these focal points that allow the increase in the flexural stresses due to partial-interaction to be quantified.

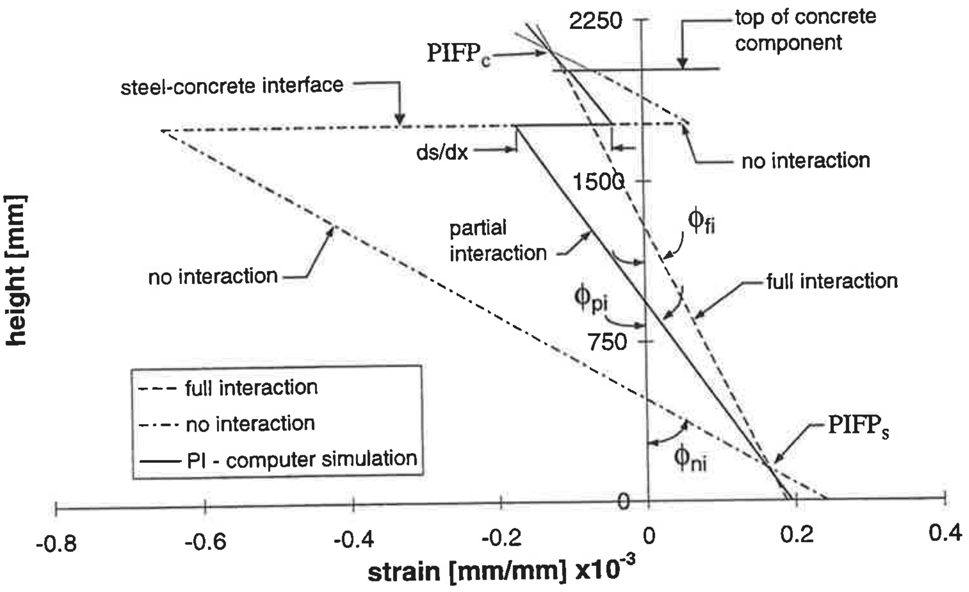

Figure 3.18: Strain distributions.

It is evident from the partial-interaction results in Fig. 3.18 that the steel and concrete stresses are greater than the full-interaction stresses currently being used. It follows then that a theoretical model must be developed to quantify the partial-interaction stresses that occur. A model is first developed in the following section to predict the partial-interaction curvature at any section along the beam. A method is presented that defines the location of the strain distribution at a section from which the corresponding flexural stresses can be calculated.

3.6 PARTIAL-INTERACTION CURVATURE

In order to develop a relationship for the curvature anywhere along a beam due to partial-interaction, Eq. 2.25 must be integrated with respect to x, the distance from the left support to the design point. By substituting Eq. 3.10 and $V^* = -V_1$ into Eq. 2.25 and then integrating with respect to x, the following mathematical expression is obtain for the curvature distribution in shear span *1*

$$\phi_1 = \frac{d_c^{\,2}A'}{E_s I_o}\left\{\frac{P}{\alpha}\left[\cosh(\alpha l_1) - \coth(\alpha L)\sinh(\alpha l_1)\right]\sinh(\alpha x) - V_1 x\right\} + \frac{V_1 x}{E_s I_o} + C_1 \qquad (3.41)$$

where the integration constant $C_1 = 0$, as the boundary condition is $\phi_1 = 0$ at $x = 0$.

Similarly, by substituting Eq. 3.11 and $V^* = V_2$ into Eq. 2.25 and integrating with respect to x, the following mathematical expression is obtained for the curvature distribution in shear span *2*

$$\phi_2 = \frac{d_c^{\,2}A'}{E_s I_o}\left\{\frac{P}{\alpha}\left[\cosh(\alpha x) - \coth(\alpha L)\sinh(\alpha x)\right]\sinh(\alpha l_1) + V_2 x\right\} + \frac{V_2 x}{E_s I_o} + C_2 \qquad (3.42)$$

where the integration constant C_2 is given by the following term using the boundary condition $\phi_2 = 0$ at $x = L$

$$C_2 = \frac{-d_c^{\,2}A'}{E_s I_o}\left\{\frac{P}{\alpha}\left[\cosh(\alpha L) - \coth(\alpha L)\sinh(\alpha L)\right]\sinh(\alpha l_1) + V_2 L\right\} + \frac{V_2 L}{E_s I_o} \qquad (3.43)$$

Figure 3.19 shows the variation of curvature along the length of the 50.4 m simply supported composite beam when the concentrated load of 320 kN is located at the quarter-span. The no-interaction and full-interaction conditions given by lines A and B respectively again define the bounds to the curvatures. Also shown is a partial-interaction curvature distribution for a constant connection stiffness under the same loading condition using both the results of a computer simulation and the theoretical model given by Eqs 3.41 and 3.42. The partial-interaction distribution lies between the two boundary conditions, as expected, and the theoretical model (line C), when compared to the predictions of the computer simulation (line D), is conservative over the length of the beam especially in the vicinity of the applied load. The discrepancy between the theoretical model and the computer simulation can be attributed to the effect of the disturbed region near the loading point on the finite element analyses.

Equation 3.41 can also be used to predict the variation of curvature in shear span 2, therefore, Eq. 3.41 is used to model the curvature along the length of the beam as it is simpler than Eq. 3.42.

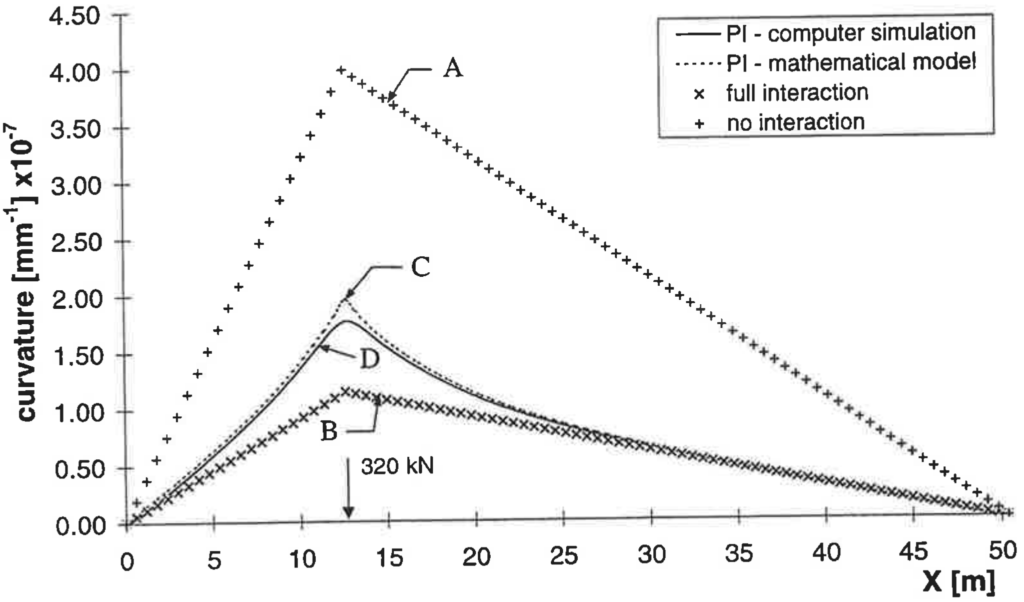

Figure 3.19: Variation of curvature.

3.6.1 Quantifying the increase in curvature

For a single concentrated load acting on a simply supported span, the maximum moment, hence curvature, at a design point occurs when the load is situated at the design point. As the maximum full-interaction curvature is readily calculable using Eq. 3.40, this section develops a multiplication factor MF_ϕ that can be applied to the full-interaction curvature ϕ_{fi} in order to determine the partial-interaction curvature ϕ_{pi}.

The multiplication factor is defined as

$$MF_\phi = \frac{\phi_k}{\phi_\infty} \tag{3.44}$$

where the numerator represents the partial-interaction curvature obtained from Eq. 3.41 when using the realistic connector stiffness k, and the denominator is the full-interaction curvature also obtained from Eq. 3.41 as the connector stiffness k approaches ∞. Hence, the full-interaction curvature is given by

$$\phi_\infty = \frac{V_1 x}{E_s I_o}\left(-d_c^{\,2} A' + 1\right) \tag{3.45}$$

As the maximum curvature occurs when $l_1 = x$, the shear force in the shear span is given by

$$V_1 = \frac{P(L-x)}{L} \tag{3.46}$$

and by substituting Eqs 3.41, 3.45 and 3.46 into Eq. 3.44, the expression for the multiplication factor becomes

$$MF_\phi = \left(-d_c^{\,2} A' + 1\right)^{-1} \times \left\{ d_c^{\,2} A' \left[\frac{L}{\alpha x (L-x)} \left(\cosh(\alpha x) - \coth(\alpha L)\sinh(\alpha x)\right)\sinh(\alpha x) - 1 \right] + 1 \right\} \tag{3.47}$$

Figure 3.20 shows the distribution of MF_ϕ using Eq. 3.47 and the results of the computer simulation for the 50.4 m composite beam where the distribution of connectors and cross-sectional geometry are such that $\alpha = 0.183\text{x}10^{-3}$ mm^{-1}, d_c = 1410 mm and $(1/A')$ = $2.80\text{x}10^6$ mm^2. The agreement is very good, and the discrepancy is again due to the disturbed effect at concentrated loads.

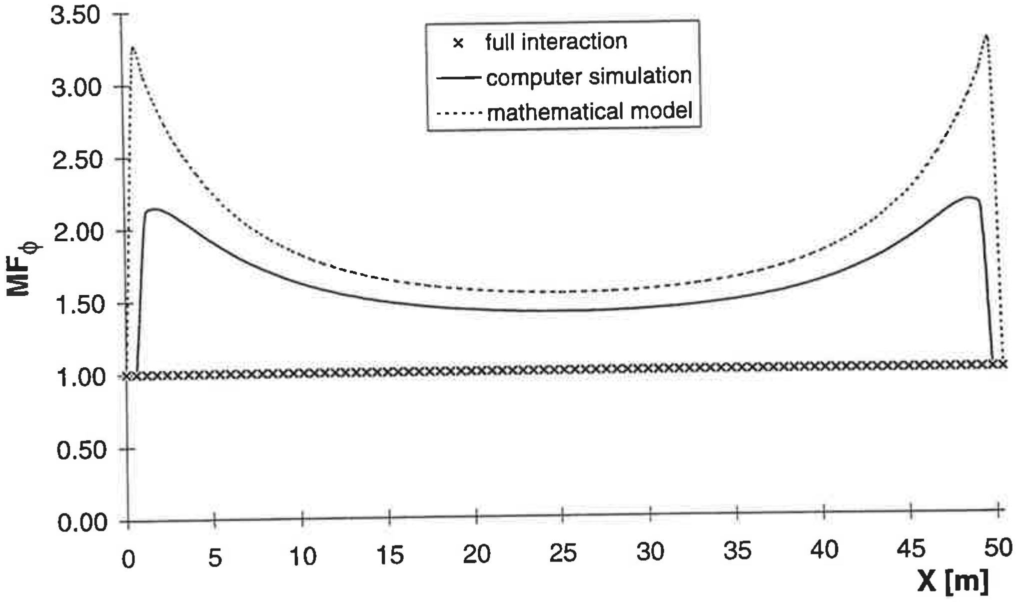

Figure 3.20: Distribution of MF_ϕ.

The relatively large multiplication factor near the supports is somewhat deceiving in that the moment, hence curvature, approaches zero at the supports resulting in only a small increase from the full-interaction curvature. The magnitude of the multiplication factor is much more significant in the middle portion of the beam where the curvatures are greatest.

3.6.2 Simplification of the multiplication factor

The mathematical model developed in Eq. 3.47 is too computationally intensive to be accepted and used in everyday design or assessment situations. Therefore, a proposed set of simplified equations is developed by making some simplifying assumptions that do not significantly reduce the accuracy of the mathematical model.

The simplified model involves estimating MF_ϕ at the supports, the quarter-span and the mid-span, and joining these points by straight line segments. As the distribution of MF_ϕ is symmetrical about the mid-span of the beam under this load condition, the multiplication factor at the support $(MF_\phi)_s$ is used at both the left and right support, and the multiplication factor at the quarter-span $(MF_\phi)_q$ is also used at the three-quarter-span.

As x approaches L (the right support) the term within the square brackets in the right hand side of Eq. 3.47 approaches zero resulting in the following simplified expression for the magnitude of the multiplication factor at the supports

$$(MF_\phi)_s = \left(-d_c^{\,2}A' + 1\right)^{-1} \tag{3.48}$$

The multiplication factor at the mid-span can be obtained by making the following assumption for the hyperbolic terms in Eq. 3.47 that is subsequently justified

$$\left(\cosh(\alpha x) - \coth(\alpha L)\sinh(\alpha x)\right)\sinh(\alpha x) \approx \frac{1}{2} \tag{3.49}$$

Hence, the expression for the magnitude of the multiplication factor at the mid-span becomes

$$(MF_\phi)_m = \left(-d_c^{\,2}A' + 1\right)^{-1}\left[d_c^{\,2}A'\left(\frac{2}{\alpha L} - 1\right) + 1\right] \tag{3.50}$$

Similarly at the quarter-span, the assumption stated in Eq. 3.49 is also made when $x = L/4$ and substitution into Eq. 3.47 yields the following magnification factor at the quarter-span

$$(MF_\phi)_q = \left(-d_c^{\,2}A' + 1\right)^{-1}\left[d_c^{\,2}A'\left(\frac{8}{3\alpha L} - 1\right) + 1\right] \tag{3.51}$$

Figure 3.21 shows the distribution of MF_ϕ from Fig. 3.20 for the 50.4 m composite beam and superimposes the distribution using the proposed simplified method where the magnification factors $(MF_\phi)_s$ in Eq. 3.48, $(MF_\phi)_m$ in Eq. 3.50 and $(MF_\phi)_q$ in Eq. 3.51 are connected with straight line segments.

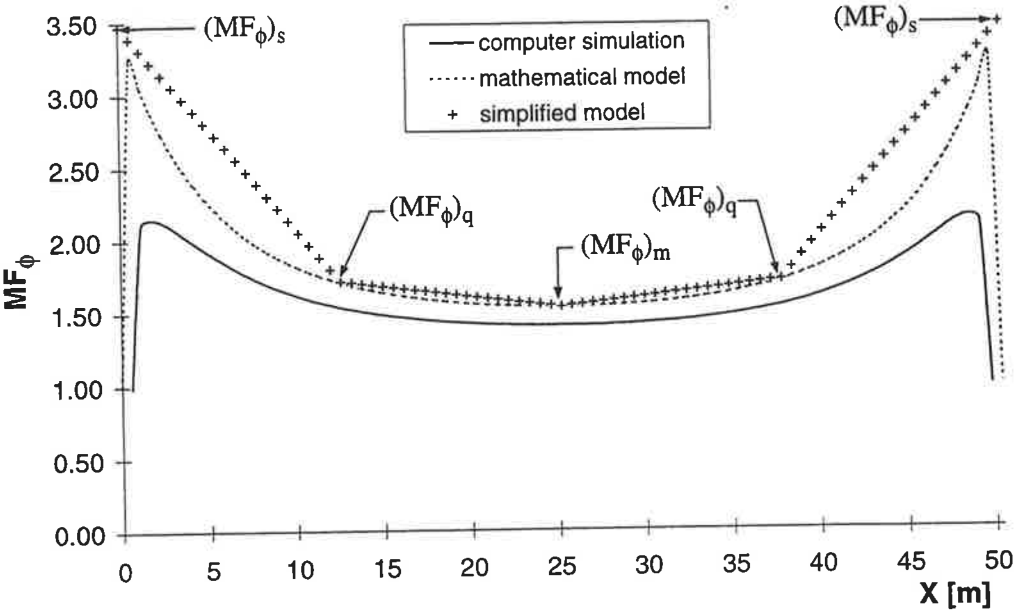

Figure 3.21: Example of simplified model of MF_ϕ.

The accuracy of the proposed simplified model compared with the mathematical model is conservative over the entire span and is a good representation of the distribution, indicating that the assumptions made while developing the simplified approach are reasonable. The agreement is exceptionally good near the mid-span where the significance of the multiplication factor is greatest as previously noted. Table 3.2 shows the actual value of Eq. 3.49 for a range of composite beams, validating the assumptions made.

Table 3.2: Validation of assumptions.

L [m]	α (x10^{-3}) [mm^{-1}]	αL	Eq. 3.49 $x = L/2$	Eq. 3.49 $x = L/4$
6	0.759	4.554	0.489585	0.448269
20	0.644	12.88	0.499997	0.499202
50	0.183	9.223	0.499901	0.495031

3.6.3 Validation of the simplified model

The preceding comparisons were limited to the 50.4 m composite beam. The simplified model of Eqs 3.48, 3.50 and 3.51 and mathematical model of Eq. 3.47 developed are now compared to computer simulations for the 20 m (Fig. 3.12) and 6 m long (Fig. 3.13) simply supported composite beams.

Figure 3.22 shows the results for the 20 m beam with a uniform distribution of connectors and cross-section such that $\alpha = 0.644\text{x}10^{-3}$ mm^{-1}, d_c = 560 mm and $(1/A')$ = $0.564\text{x}10^{6}$ mm^2. The mathematical model is again slightly greater than that predicted by the computer simulation due to the disturbed effect under the point load in the finite element analysis. The simplified model is conservative along the entire span, with very good agreement being achieved over the mid-span portion of the beam where the change in the curvature, hence flexural stresses, is most critical.

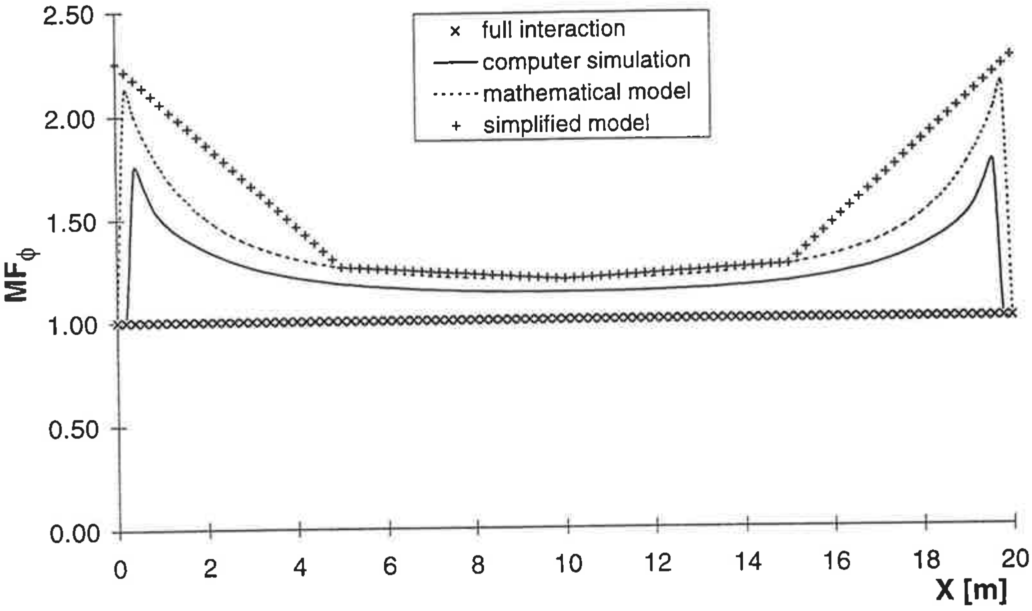

Figure 3.22: Comparison of MF_ϕ for the 20 m long beam.

Figure 3.23 shows the results for the 6 m beam with a uniform distribution of connectors and cross-section such that $\alpha = 0.759\text{x}10^{-3}$ mm^{-1}, d_c = 227 mm and $(1/A')$ = $82.0\text{x}10^{3}$ mm^2. The comparison given in Fig. 3.23 shows that the predictions are acceptable and that the simplified model is conservative over the entire span, however, the differences are greater for this relatively short 6 m beam compared to the results of the 20 m beam in Fig. 3.22 and the 50.4 m beam in Fig. 3.21. The greater discrepancy between the computer simulation and the mathematical model in Fig. 3.23 is due to the disturbed region affecting a larger proportion of the span; the discrepancy between the simplified and the mathematical model is due to the deviation from the assumption given by Eq. 3.49 that was made while developing the simplified relationships. The smaller α and/or *L*, the greater the error will be as seen in Table 3.2, however, the proposed simplified model is still useable as the error results in conservative predictions.

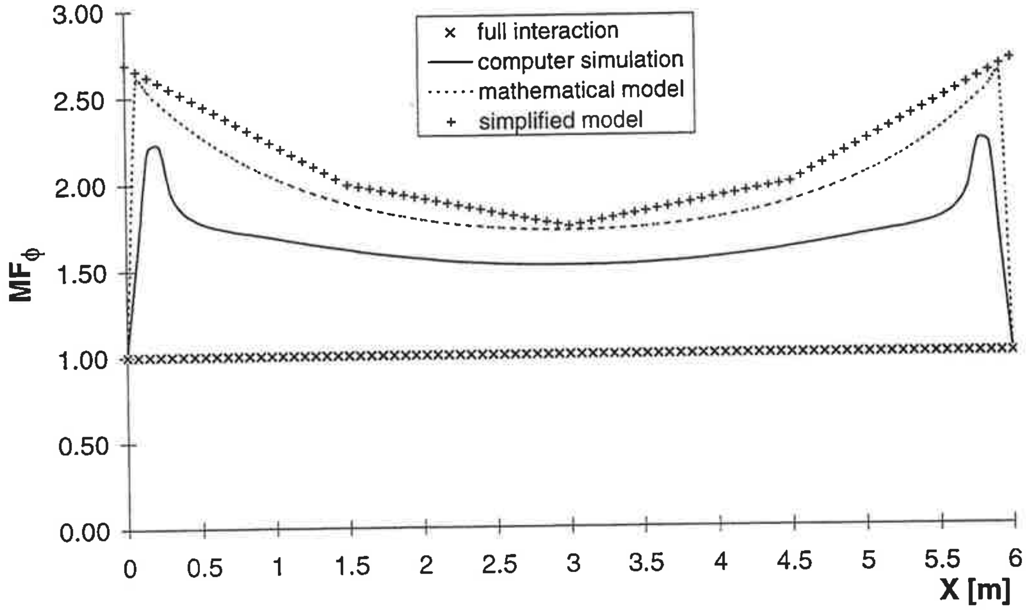

Figure 3.23: Comparison of MF_ϕ for the 6 m long beam.

3.7 PARTIAL-INTERACTION FOCAL POINTS

The previous section developed a procedure for predicting the partial-interaction curvature from the full-interaction curvature. However, in order to determine the partial-interaction strain distribution, so that the corresponding flexural stresses can be calculated, the position of the strain profile at the known curvature must be determined. This section develops a means of locating the partial-interaction strain distribution by quantifying the focal points already described.

It was shown in Fig. 3.18 that the two bounds to the strain distributions, resulting from a full-interaction and no-interaction approach, intersect at the locations that have been referred to as the focal points, $PIFP_c$ and $PIFP_s$. It is significant to note that the point does not necessarily lie within the corresponding component, as is the case with $PIFP_c$ in Fig. 3.18. As the boundary distributions intersect at these points, it is logical to question whether any strain distribution at that section must also pass through the same two points, thereby defining the additional points necessary to locate the partial-interaction curvatures and, hence, strain distributions.

The following analyses show that two focal points exist, that all partial-interaction strain distributions pass through these points, and that the location of the focal points are independent of the connector stiffness. Simple expressions are then developed to locate the focal points. The first step is to prove that only one strain distribution can exist that results in equilibrium at a section. This is accomplished by investigating the strain distributions at a section of a composite beam that is made up of two components of equal size and stiffness, as shown in Fig. 3.24, where the magnitude of the externally applied axial load N is equal to zero.

A full-interaction analysis yields the strain distribution given by line A in Fig. 3.24 where the centroid of the composite section is at mid-height of the composite section. The no-interaction analysis distribution is given by line B where the centroid of each component is located at mid-height of the component. The question that is posed is: "Given a partial-interaction strain distribution, line C, which passes through the focal points, is there another distribution that can be defined with the same curvature but offset from the focal points by an amount $\Delta\varepsilon$, line D, such that equilibrium is maintained?"

By defining the strain at the top of component *1* as $-\varepsilon$, the strain at the bottom of component *2* must be ε by symmetry, where negative is taken as compression. The partial-interaction curvature ϕ_{pi} is the same in both components assuming that there is no separation at the interface. It needs to be shown that the shift $\Delta\varepsilon$ must maintain zero total axial load, $N = 0$, in the composite member. Simplifying the calculations somewhat by assuming that the width b, depth h, and stiffness E are equal to unity, the net axial force in component *1* at the shift $\Delta\varepsilon$ is given by

$$N_1 = \frac{\phi_{pi}}{2} - \varepsilon - \Delta\varepsilon \tag{3.52}$$

and the net axial force in component 2 is

$$N_2 = -\frac{\phi_{pi}}{2} + \varepsilon - \Delta\varepsilon \tag{3.53}$$

Summing Eqs 3.52 and 3.53, and equating the result to zero to enforce the equilibrium condition of zero total axial load, it is found that

$$\Delta\varepsilon = 0 \tag{3.54}$$

proving that only one partial-interaction strain distribution exists at a section for a given moment.

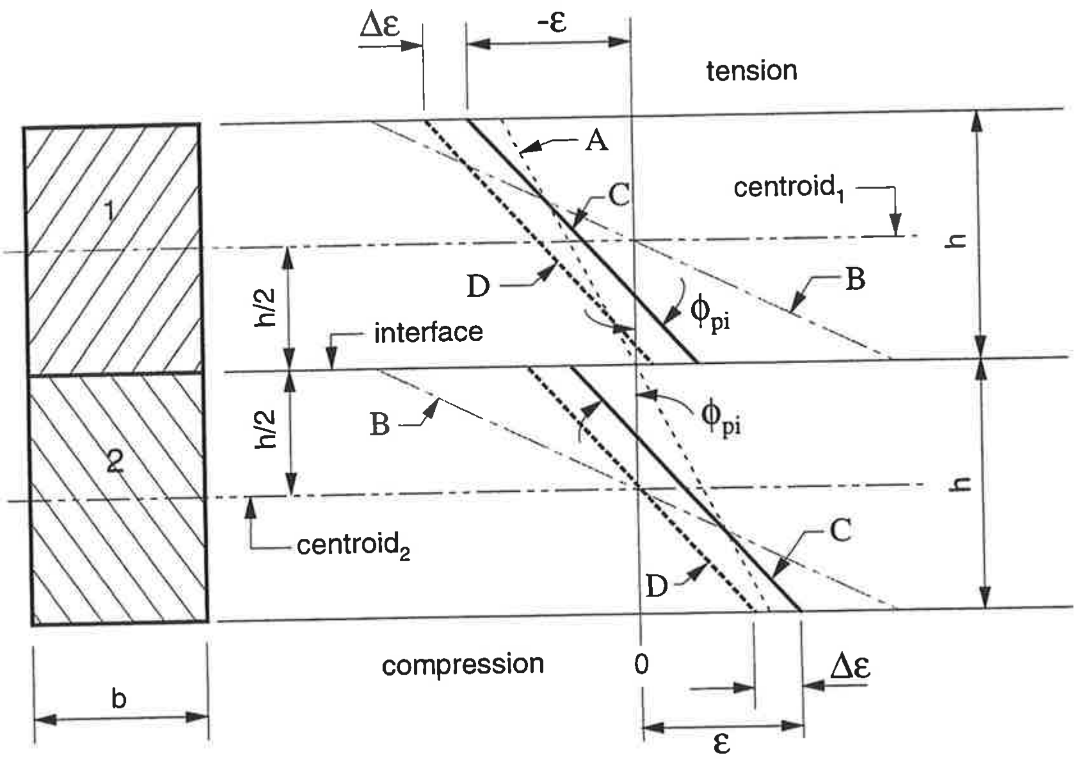

Figure 3.24: Simple partial-interaction distribution.

It is now shown that the partial-interaction focal points exist for a general composite section, and that the partial-interaction strain distribution must pass through the focal points, so that these two points can be used to locate the distribution.

A general composite bridge beam cross-section is defined in Fig. 3.25, where the variable h is used to define the depth, t the thickness and w the width of the various elements; the subscripts c and s represent the concrete and steel components respectively, tf the top flange, bf the bottom flange and w the web. Therefore, the area of concrete $A_c = h_c w_c$, the area of the top flange $A_{tf} = w_{tf} t_{tf}$ and similarly, the area of the bottom flange $A_{bf} = w_{bf} t_{bf}$. The variables y_s and y_c are distances to points within the steel and concrete components respectively measured from the steel-concrete interface, where positive is taken as the direction shown in Fig. 3.25.

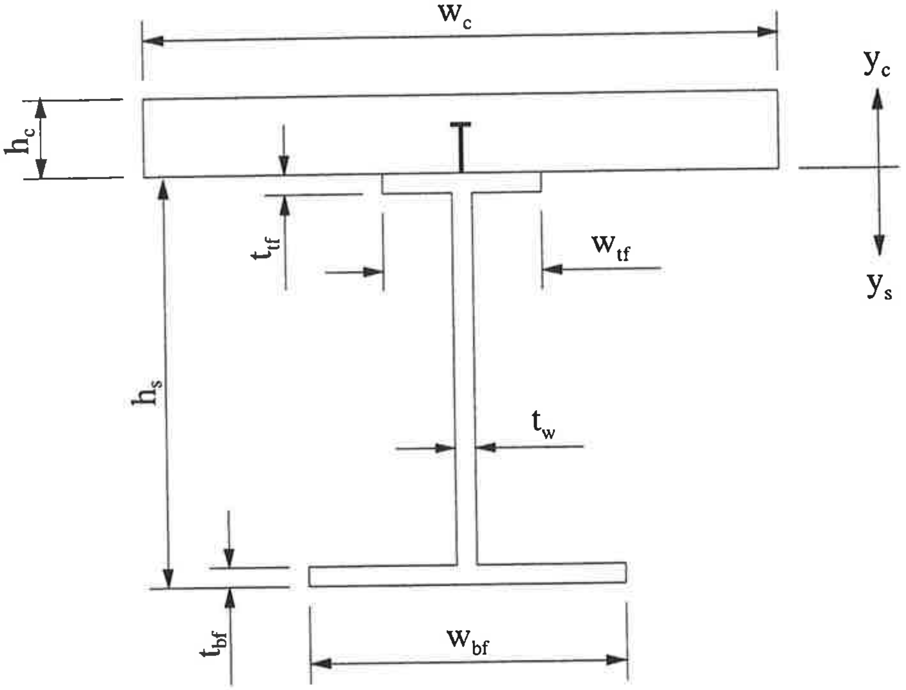

Figure 3.25: Definition of variables.

An arbitrary yet compatible partial-interaction strain distribution is defined in Fig. 3.26 where the vertical dimension is exaggerated for clarity. The distribution is defined by the strain at the top of the steel component $(\varepsilon_s)_{top}$, the partial-interaction curvature ϕ_{pi} (Eq. 3.41) and the slip strain given by the following expression obtained by substituting Eqs 3.6 and 3.7 into Eq. 3.5 to give

$$\frac{ds}{dx} = \alpha\beta P\left[\cosh(\alpha l_1) - \sinh(\alpha l_1)\coth(\alpha L)\right]\sinh(\alpha x) \tag{3.55}$$

The magnitude of the reference strain $(\varepsilon_s)_{top}$ is then determined by ensuring that the equilibrium condition of no axial force is satisfied by first calculating the net axial force in the concrete

$$N_c = E_c A_c \left[\left(\frac{ds}{dx} - \frac{h_c \phi_{pi}}{2}\right) - (\varepsilon_s)_{top}\right] \tag{3.56}$$

and the net axial force in the steel component

$$\begin{aligned} N_s = {} & E_s(\varepsilon_s)_{top}\left[-A_{tf} + (t_{tf} + t_{bf} - h_s)t_w - A_{bf}\right] + \\ & \frac{1}{2}E_s\phi_{pi}\left[t_{tf}A_{tf} + \left(-t_{tf}^2 + h_s^2 - 2h_s t_{bf} + t_{bf}^2\right)t_w + (2h_s - t_{bf})A_{bf}\right] \end{aligned} \tag{3.57}$$

By summing Eqs 3.56 and 3.57, equating to zero and solving for the strain at the top of the steel component, the following expression is obtained

$$(\varepsilon_s)_{top} = \frac{-\dfrac{A_c}{n}\left(\dfrac{ds}{dx} - \dfrac{h_c \phi_{pi}}{2}\right) - \dfrac{\phi_{pi}}{2}(A_s h_s)_{n/s}}{-\dfrac{A_c}{n} - A_s} \tag{3.58}$$

where

$$(A_s h_s)_{n/s} = t_{tf} + \left(-t_{tf}^2 + h_s^2 - 2h_s t_{bf} + t_{bf}\right)t_w + (2h_s - t_{bf})A_{bf} \tag{3.59}$$

For the case when the steel component is doubly symmetrical, Eq. 3.58 can be simplified to the following

$$(\varepsilon_s)_{top} = \frac{-\frac{A_c}{n}\left(\frac{ds}{dx}-\frac{h_c\phi_{pi}}{2}\right)-\frac{\phi_{pi}}{2}(A_s h_s)}{-\frac{A_c}{n}-A_s} \tag{3.60}$$

Having defined $(\varepsilon_s)_{top}$, the following equations can be used to calculate the strain at any depth along the cross-section

$$(\varepsilon_s)_{pi} = \phi_{pi} y_s - (\varepsilon_s)_{top} \tag{3.61}$$

and

$$(\varepsilon_c)_{pi} = -\phi_{pi} y_c - (\varepsilon_s)_{top} + \frac{ds}{dx} \tag{3.62}$$

where $(\varepsilon_s)_{pi}$ and $(\varepsilon_c)_{pi}$ are the partial-interaction strains in the steel and concrete respectively.

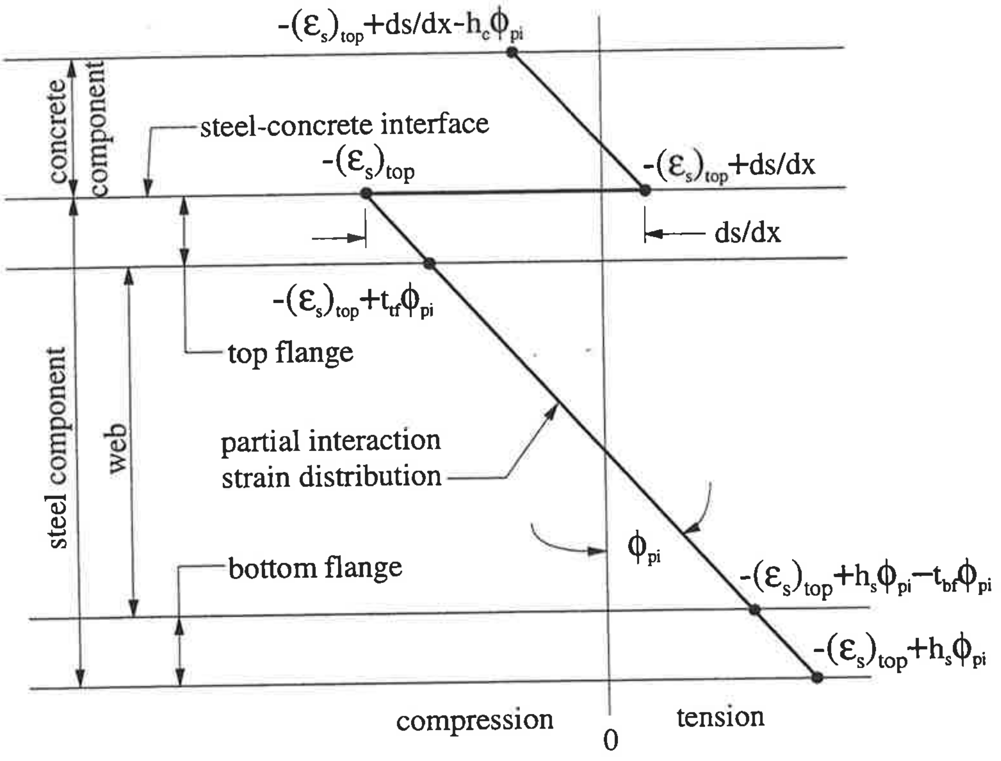

Figure 3.26: General partial-interaction strain distribution.

If the assumption that the partial-interaction strain distribution passes through the two partial-interaction focal points is true, the strain at the focal points for a given moment at a section must be constant regardless of the stiffness of the connection. Similarly, the distance of the focal points from the steel-concrete interface must also be constant and independent of the connection stiffness. It must therefore be shown that

$$\frac{d(\varepsilon_s)_{pi}}{dk}=0 \tag{3.63}$$

at the focal point in the steel component and that $(y_s)_{fp}$, which is the distance of the focal point in the steel component measured from the interface, is not a function of k. Similarly for the concrete strains, it must be shown that

$$\frac{d(\varepsilon_c)_{pi}}{dk}=0 \tag{3.64}$$

at the focal point in the concrete component and that $(y_c)_{fp}$, which is the distance of the focal point in the concrete component measured from the interface, is also not a function of k.

Differentiating Eq. 3.61 with respect to k, where y_s = $(y_s)_{fp}$ and ϕ_{pi} is a function of k, and solving for the location of PIFP$_s$ results in the following expression

$$(y_s)_{fp}=\frac{\frac{A_c}{n}\left(-\frac{1}{d_c A'}+\frac{h_c}{2}\right)-\frac{A_s h_s}{2}}{-\frac{A_c}{n}-A_s} \tag{3.65}$$

where the $A_s h_s$ term is replaced by $(A_s h_s)_{n/s}$ in Eq. 3.59 if a non-symmetrical steel component is used. Similarly, Eq. 3.62 is differentiated with respect to k, where y_c = $(y_c)_{fp}$, and ϕ_{pi} and ds/dx are a function of k, in order to solve for the location of PIFP$_c$ giving

$$(y_c)_{fp} = \frac{\dfrac{A_c h_c}{2n} + A_s\left(\dfrac{1}{d_c A'} - \dfrac{h_s}{2}\right)}{\dfrac{A_c}{n} + A_s} \tag{3.66}$$

where again the $A_s h_s$ term is replaced with $(A_s h_s)_{n/s}$ in Eq. 3.59 if a non-symmetrical steel component is used.

It has, therefore, been proved that any strain distribution at a section must pass through the partial-interaction focal points regardless of the connection stiffness, as Eqs 3.65 and 3.66 which define the location of the focal points, are not a function of the connector stiffness. The next section develops a simple procedure whereby the partial-interaction strain distribution can be located making use of the partial-interaction focal points.

3.8 PARTIAL-INTERACTION STRAIN DISTRIBUTION

As all strain distributions at a section pass through the two focal points regardless of the connection stiffness, it follows then that the points where the full-interaction and no-interaction strain distributions intersect can be used to define the position of the focal points.

Dealing with the focal point in the steel component first, the strain distribution in the steel under full-interaction and no-interaction can be defined using the following equations respectively

$$(\varepsilon_s)_{fi} = \frac{M}{E_c I_{nc}}(y_s - \bar{y}_{nc}) \tag{3.67}$$

and

$$(\varepsilon_s)_{ni} = \frac{M}{\sum EI}(y_s - \bar{y}_s) \tag{3.68}$$

where by equating Eqs 3.67 and 3.68, $(y_s)_{fp}$ can be found and which is given by the following simple equation

$$(y_s)_{fp} = \frac{\bar{y}_{nc} - \dfrac{E_c I_{nc}}{\sum EI}\bar{y}_s}{1 - \dfrac{E_c I_{nc}}{\Sigma EI}} \tag{3.69}$$

and the corresponding strain at PIFP$_s$ can be found by substituting Eq. 3.69 for y_s in Eq. 3.67 to give

$$(\varepsilon_s)_{fp} = \frac{M}{E_c I_{nc}}\left((y_s)_{fp} - \bar{y}_{nc}\right) \tag{3.70}$$

Similarly for the focal point in the concrete component, the strain distribution in the concrete under full- and no-interaction can be defined using the following equations respectively

$$(\varepsilon_c)_{fi} = \frac{M}{E_c I_{nc}}\left(-y_c - \bar{y}_{nc}\right) \tag{3.71}$$

and

$$(\varepsilon_c)_{ni} = \frac{M}{\sum EI}\left(-y_c + \bar{y}_c\right) \tag{3.72}$$

where by equating Eqs 3.71 and 3.72, $(y_c)_{fp}$ can be found from the following simple expression

$$(y_c)_{fp} = \frac{\bar{y}_{nc} + \dfrac{E_c I_{nc}}{\sum EI}\bar{y}_c}{\dfrac{E_c I_{nc}}{\sum EI} - 1} \tag{3.73}$$

where $(y_c)_{fp}$ may be located outside of the concrete component, and the corresponding strain at PIFP$_c$ can be found by substituting Eq. 3.73 for y_c in Eq. 3.71 to give

$$(\varepsilon_c)_{fp} = \frac{M}{E_c I_{nc}}\left(-(y_c)_{fp} - \bar{y}_{nc}\right) \tag{3.74}$$

3.8.1 Proposed procedure

The following summarizes the proposed procedure for determining the partial-interaction strain distribution so that the corresponding flexural stresses can be found using the relationships developed in this chapter:

1. Calculate the full-interaction curvature ϕ_{fi} at a design point using Eq. 3.40;
2. Determine multiplication factor MF_ϕ using either the mathematical model of Eq. 3.47 or the simplified model of Eqs 3.48, 3.50 and 3.51;
3. Find the partial-interaction curvature ϕ_{pi} by multiplying ϕ_{fi} with MF_ϕ;
4. Define the location of PIFP$_s$ by determining $(y_s)_{fp}$ from Eq. 3.69 and $(\varepsilon_s)_{fp}$ from Eq. 3.70;
5. Repeat step 4 for PIFP$_c$ using $(y_c)_{fp}$ from Eq. 3.73 and $(\varepsilon_c)_{fp}$ from Eq. 3.74;
6. The partial-interaction strain distribution is determined by passing a line with slope ϕ_{pi} through both PIFP$_s$ and PIFP$_c$; and
7. Calculate corresponding flexural stresses as required.

3.9 ILLUSTRATIVE EXAMPLE

The following example is used to illustrate the beneficial effect of partial-interaction on the endurance of the shear connectors and the detrimental effect of partial-interaction on the flexural stresses. The decrease in the shear flow due to partial-interaction is determined by applying the reduction factors to the full-interaction shear flows. The increase in the flexural stresses due to partial-interaction are determined using both the increase in the full-interaction curvature as derived from the multiplication factors and the focal points.

Suppose that the 50.4 m long simply supported composite beam (Fig. 3.1) has been designed using a full-interaction analysis procedure and for a fatigue life of 100 years or 200x10^6 fatigue vehicle traversals. The cross-sectional geometry of the beam is such that I_o = 3.80x10^{10} mm^4 and $(1/A')$ = 2.80x10^6 mm^2, and the standard fatigue vehicle loading was such that R_{fi} = 161 N/mm and P_{fi} = 80.7 N/mm for the design point at the mid-span. The beam was designed for a maximum design overload $Q_{res} = 9xP_{fi}$ = 726 N/mm and the shear flow strength required at the start of the design life was Q_{st} = 1845 N/mm. A uniform distribution of connectors was used consisting of 2 rows of studs at 100 mm centers which resulted in α = 0.635x10^{-3} mm^{-1}. In this example, F_f = (1.0)(161)$^{5.1}$ = 1.82x10^{11} (N/mm)$^{5.1}$ and L_f will be taken as unity.

The condition of the shear connectors after the original design life of 200 million fatigue vehicle traversals can now be assessed. By substituting αL = 32.0 into the relevant expression for the reduction factor of R_{fi} (Eq. 3.39) gives $(RF_R)_c$ = 0.77 so that R_{pi} = (0.77)(161) = 124 N/mm. As the design point under consideration is at the mid-span, the same reduction factor is applied to P_{fi} so that P_{pi} = (0.77)(80.7) = 62.1 N/mm. The force factor must also be revised to F_f = (1.0)(124)$^{5.1}$ = 4.75x10^{10} N/mm, and the maximum design overload becomes Q_{res} = 9x62.1 = 559 N/mm. Substituting these new values for F_f and Q_{res} into the fatigue damage equation in assessment mode (Eq. 2.60) gives the following expression

$$T_2 = \frac{1318(1845)^{5.1}\left(1-\dfrac{559}{1845}\right)-200\times10^6\left(4.75\times10^{10}\right)(1.0)}{4.75\times10^{10}(1.0)} \tag{3.75}$$

where the last term in the numerator of the right hand side represents the fatigue damage that has occurred, and the denominator is the fatigue damage that can still occur. Solving for the remaining endurance gives T_2 = 677x10^6, that is, 677 million fatigue vehicles. Assuming that 2 million fatigue vehicles occur annually, as used in the initial design, the remaining life of the shear connectors is another 338 years. It is worth noting that the remaining endurance of 677x10^6 vehicles is reduced to 563x10^6 vehicles when the reduction in the peak shear load P_{fi} due to partial-interaction is ignored. Therefore, the reduction in R_{fi} alone accounted for 83% of the increase in the remaining life of the shear connection.

The changes in the flexural stresses due to partial-interaction at mid-span are investigated next. The full-interaction strain distribution is shown in Fig. 3.27 where the centroid of the full-interaction transformed concrete section $\bar{y}_{nc}$ is located 474 mm below the steel-concrete interface in the steel component. The full-interaction curvature is ϕ_{fi} = 0.159x10^{-6} mm^{-1} where M = 4032 kNm and EI_{fi} = 2.64x10^{16} Nmm^2.

The first step in the analysis is to calculate the multiplication factor for the full-interaction curvature at the mid-span which is given by Eq. 3.50, where the cross-sectional geometry of the beam is such that d_c = 1410 mm, to give $(MF_\phi)_m$ = 1.15 so that ϕ_{pi} = (1.15)(0.159x10^{-6}) = 0.183x10^{-6} mm^{-1}. Knowing that the no-interaction flexural stiffness EI_{ni} = 7.60x10^{15} Nmm^2, and $\bar{y}_S$ = 1290 mm and $\bar{y}_C$ = 125 mm, which are both measured from the steel-concrete interface, the location of the partial-interaction focal points may be calculated using Eqs 3.69 and 3.73 to give $(y_s)_{fp}$ = 1620 mm and $(y_c)_{fp}$ = 368 mm respectively, again measured from the steel-concrete interface. The corresponding strains at the PIFP's are now calculated using Eqs 3.70 and 3.74 to give $(\varepsilon_s)_{fp}$ = 0.182x10^{-3} mm/mm and $(\varepsilon_c)_{fp}$ = -0.134x10^{-3} mm/mm respectively. The partial-interaction strain distribution at the mid-span is shown in Fig. 3.27.

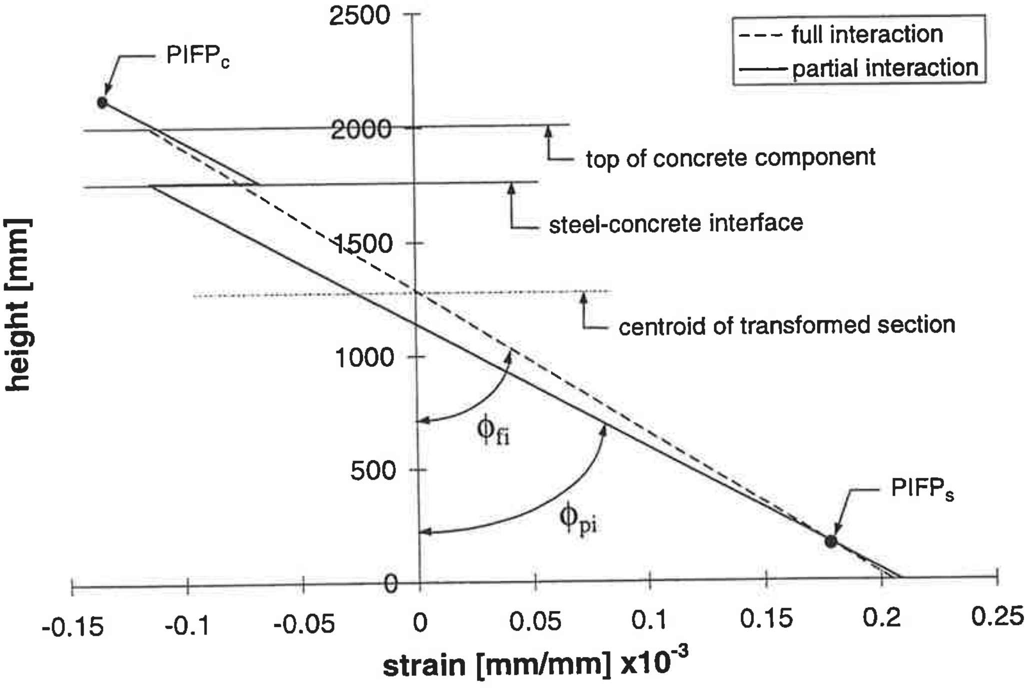

Figure 3.27: Strain distributions at mid-span.

Several conclusions can be drawn from Fig. 3.27. Perhaps the most significant observation is that the partial-interaction focal points are located on the extreme fiber side of the centroids of the corresponding component, therefore, amplifying the effect on the strains and stresses adjacent to the steel-concrete interface. Hence, there is little change in the compressive stress at the top of the concrete component and only a slight increase in the tensile stresses at the bottom of the steel component. The increase in the tensile stress range in the steel component is about 2%. If the fatigue endurance exponent for the steel is taken as 3 then this 2% increase in the stress will reduce the endurance of the component by a factor of $(1.02)^{-3} = 0.94$. Adjacent to the steel-concrete interface, the compressive stress at the top of the steel flange is increased significantly by 52%, which may need to be allowed for in the design for buckling of the flange. Furthermore, the concrete compressive stress adjacent to the interface is reduced by 10% which in this application is beneficial, however, it is noted that if the reduction is great enough tensile stresses may result in the concrete for which account must be taken.

Chapter 4

Non-linear partial-interaction

4.1 INTRODUCTION

The dead load of the concrete structure above the longitudinal steel beams and the downward acting vehicle loads result in a compressive distribution of forces acting normal to the steel-concrete interface. As the coefficient of friction between steel and concrete under cyclic loading varies between $0.70 < \mu < 0.95$ (Section 2.4), frictional forces acting along the steel-concrete interface influence the longitudinal shear forces resisted by the stud shear connectors.

The effect of the frictional resistance and the non-linear load-slip relationship of the stud shear connectors are combined in an iterative non-linear secant stiffness procedure so that the understanding of the behavior of simply supported composite bridge beams can be increased. The physical behavior of the longitudinal shear forces that act along the steel-concrete interface are described first which is then followed by the resulting finite element model used to simulate the behavior. Typical results are presented to qualitatively illustrate the effect of friction on the behavior of composite bridge beams, and finally, a comparison is made with the mathematical model given by Eq. 2.61.

4.2 PHYSICAL BEHAVIOR

The model shown in Fig. 4.1 was developed to determine the magnitude and direction of the forces acting along the steel-concrete interface at a stud. The total longitudinal shear force Q must be resisted by the connectors and, if present, friction f. The change in the longitudinal slip s is a function of the force that is resisted by the connectors q_{dowel}. The force q_{dowel} is related to s by the stiffness of the spring k, which represents the stiffness of the connectors, by the following equation

$$q_{dowel} = ks \tag{4.1}$$

The change in q_{dowel} depends on the magnitude of the frictional resistance available F_{fr} with respect to the other forces as described in subsequent sections 4.2.1 and 4.2.2. The magnitude of F_{fr} is a function of the magnitude of the normal force N acting across the interface as given by the following expression

$$F_{fr} = |\mu N| \tag{4.2}$$

when there is negative uplift, hence, the normal force is orientated such that it is compressive across the steel-concrete interface as shown in Fig. 4.1. In areas of the span where there is positive uplift, and the tendency is for the steel and concrete components to separate, F_{fr} is taken as zero.

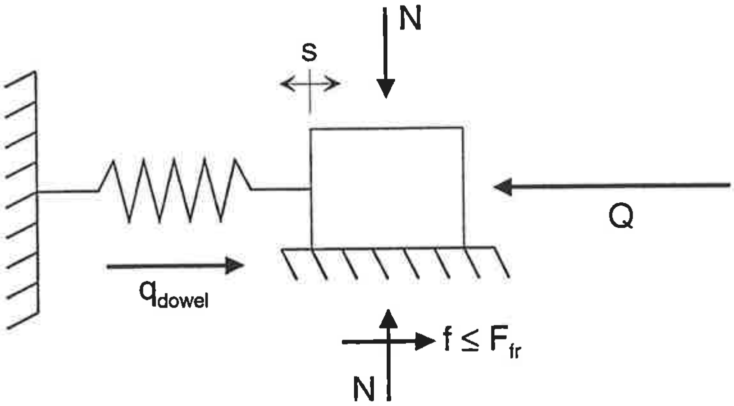

Figure 4.1: Model of the forces acting along the steel-concrete interface.

It is the *change* in F_{fr} and Q at a specific point, as the applied load is moved across the beam, that is important as the change is what determines the magnitude and direction of s, hence, q_{dowel}. This is described in more detail in the following two sections; the first one illustrates the behavior when Q remains uni-directional, and the second section deals with the case when Q reverses direction.

4.2.1 Uni-directional case

This section illustrates possible changes in slip, at a point, as the load is moved a distance dx along the beam, from location i to $i+1$, when the direction of the total longitudinal shear force does not change. The following terms are defined as they are required in the explanation

$$\Delta Q = \left|Q_{i+1} - Q_i\right| \tag{4.3}$$

$$\Delta F_{fr} = \left|\left(F_{fr}\right)_{i+1} - \left(F_{fr}\right)_i\right| \tag{4.4}$$

$$\Delta s = \left|s_{i+1} - s_i\right| \tag{4.5}$$

$$\Delta q_{dowel} = \left|\left(q_{dowel}\right)_{i+1} - \left(q_{dowel}\right)_i\right| \tag{4.6}$$

where the prefix Δ represents the change in the magnitude of the variable. The discussion also makes use of the following equality, required for horizontal equilibrium, as shown in Fig. 4.1

$$Q = f + q_{dowel} \tag{4.7}$$

In order to determine possible load-slip paths, two general categories have been identified; the first category is when $Q_{i+1} > Q_i$, and the second is when the opposite occurs and $Q_{i+1} < Q_i$. Each of the categories are in turn subdivided into a number of sub-categories depending on the relative magnitudes of F_{fr} and Q.

Numerous scenarios exist for each of the sub-categories, the qualitative examples that follow are used to give a feel for the possible load-slip paths. All of the examples presented are valid when $(F_{fr})_i = Q_i$. Figure 4.2 illustrates three general load-slip paths for a point along the steel-concrete interface, which are possible when Q_{i+1} is greater than Q_i, where the vertical axis is the total longitudinal shear force, the horizontal axis is the slip and the solid arrow indicates how the slip will change as Q increases. Figure 4.2a illustrates the case when F_{fr} has increased and the increase in the total longitudinal shear force is less than the increase in the maximum frictional resistance. As not all of ΔF_{fr} is utilized while maintaining equilibrium, there is no change in q_{dowel}, hence, s. This case illustrates the point that f is not necessarily equal to F_{fr}, however, it is necessary that F_{fr} be exceeded before there is a change in q_{dowel}.

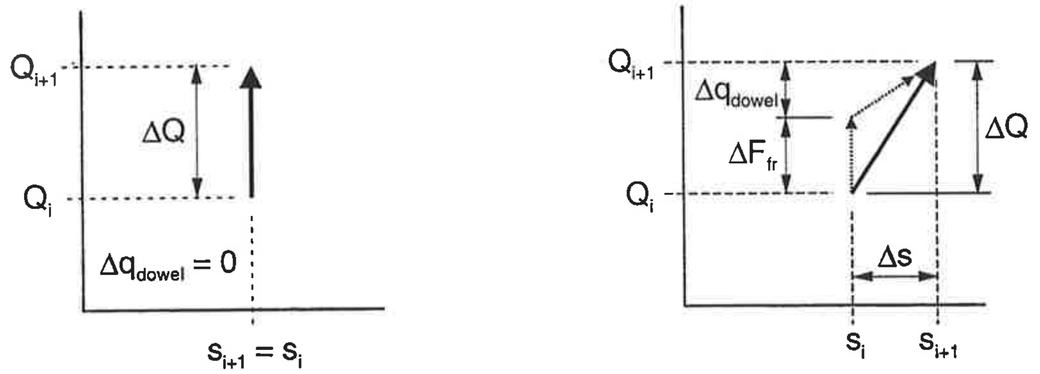

a) $(F_{fr})_{i+1} > (F_{fr})_i$ and $\Delta Q < \Delta F_{fr}$

b) $(F_{fr})_{i+1} > (F_{fr})_i$ and $\Delta Q > \Delta F_{fr}$

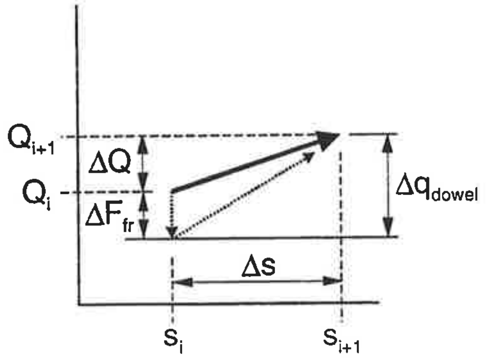

c) $(F_{fr})_{i+1} < (F_{fr})_i$

Figure 4.2: Possible load-slip diagrams when $Q_{i+1} > Q_i$.

Figure 4.2b illustrates the scenario when F_{fr} again increases, however, the increase in the total longitudinal shear flow is greater than the increase in the maximum frictional resistance. In this case, all of the F_{fr} is utilized and, hence, q_{dowel} must increase in order to maintain horizontal equilibrium (Fig. 4.1). The increase in the longitudinal shear force resisted by the connectors, Δq_{dowel}, must be equal to (ΔQ - ΔF_{fr}), which results in the increase in slip Δs.

The load-slip path when the maximum frictional resistance reduces and the total longitudinal shear force increases is shown in Fig. 4.2c. Again, all of the F_{fr} is utilized and there must be an increase in q_{dowel} in order to maintain equilibrium. Under these conditions, however, Δq_{dowel} must equal (ΔQ+ΔF_{fr}) resulting in a corresponding increase in slip, Δs.

The second category that can occur is when there is a decrease in the total longitudinal shear force at a point, defined by the inequality $Q_{i+1} < Q_i$, when the load is moved along the beam. Two general load-slip paths are presented in Fig. 4.3 that are used to explain various scenarios.

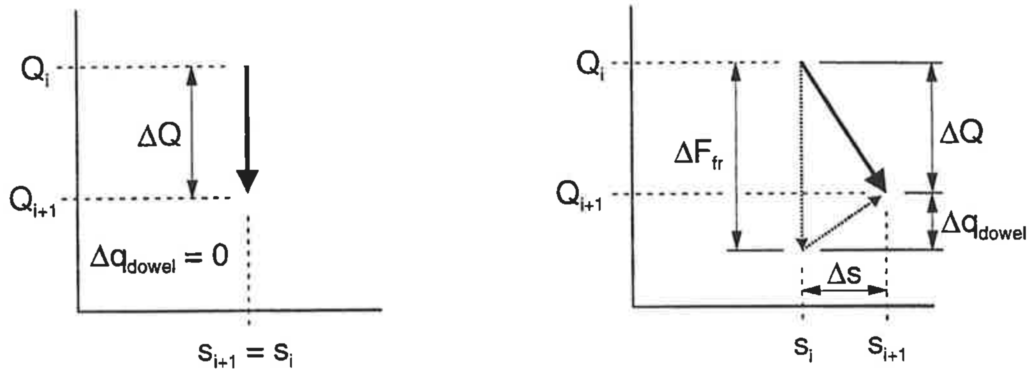

a) $(F_{fr})_{i+1} > (F_{fr})_i$ *or* $(F_{fr})_{i+1} < (F_{fr})_i$ and $\Delta Q > \Delta F_{fr}$

b) $(F_{fr})_{i+1} < (F_{fr})_i$ and $\Delta Q < \Delta F_{fr}$

Figure 4.3: Possible load-slip diagrams when $Q_{i+1} < Q_i$.

The scenario illustrated in Fig. 4.3a, which shows that there is no change in the slip at a point even though the total longitudinal shear force has reduced, occurs under two different conditions. The first condition is when the maximum frictional resistance increases as the total longitudinal shear force decreases. In this situation, the frictional force required to maintain horizontal equilibrium f is less than F_{fr} and, hence, there can be no change in q_{dowel} and therefore, $\Delta s = 0$. The second condition Fig. 4.3a represents is when the maximum frictional resistance reduces, but to a lesser extent than the reduction in the total longitudinal shear force. Again F_{fr} remains larger than that required for equilibrium such that $(F_{fr})_{i+1} > f_{i+1} = Q_{i+1} - (q_{dowel})_i$ and so, $\Delta q_{dowel} = \Delta s = 0$.

When the maximum frictional resistance at a point is reduced more than the total longitudinal shear force, the load-slip path shown in Fig. 4.3b occurs. In this case, all of maximum frictional resistance is required such that $f_{i+1} = (F_{fr})_{i+1}$ and, hence, in order to maintain horizontal equilibrium, q_{dowel} must *increase* by $\Delta q_{dowel} = \Delta F_{fr} - \Delta Q$. It can be seen, therefore, that it is also possible for the slip to increase even though the total longitudinal shear force has decreased and that the influence of friction along the steel-concrete interface contributes significantly to the load-slip behavior of the shear connection.

4.2.2 Reverse case

The situation will arise when the total longitudinal shear force at a point changes direction as the load is moved along the beam. A general load-slip path is presented in Fig. 4.4, which also includes a simple numerical example down the right side of the figure to aid in the discussion. The initial conditions are given by point A in Fig. 4.4 where the slip is s_i and the total longitudinal shear force is $Q_i = 10$. It is assumed that all of the maximum frictional resistance is utilized at point A so that $f_i = (F_{fr})_i$, which in this example is equal to 5, therefore, for horizontal equilibrium, $(q_{dowel})_i = Q_i - (F_{fr})_i = 5$ and is in the same direction as the frictional force. The final condition at G in Fig. 4.4, after the load has moved, is that $Q_{i+1} = 9$ and in the opposite direction of Q_i, and that $(F_{fr})_{i+1} = 8$, which of course can act in any direction as required. Using this simple numerical example, the remainder of this section describes the load slip path taken as the total longitudinal shear force changes from Q_i to Q_{i+1}.

As the total longitudinal shear force reduces from Q_i (point A in Fig. 4.4), the frictional force required for equilibrium f reduces proportionately from $(F_{fr})_i$ until point B is reached. At point B, the total longitudinal shear force has reduced to $(q_{dowel})_i$, hence, the frictional force f required to maintain equilibrium is zero. Further reduction of Q results in an increase in f, in the direction *opposite* that at point A, to maintain equilibrium such that $f = (q_{dowel})_i - Q$. At point C, $Q = 0$ and $f = (q_{dowel})_i$, which has yet to exceed $(F_{fr})_{i+1}$ and require a change in q_{dowel}, which is why the slip has not changed from s_i. Beyond point C, the total longitudinal shear force begins to increase in magnitude in the opposite direction of Q_i, f continues to increase and is equal to $(q_{dowel})_i + Q$ until point D is reached. At D, the frictional force required for equilibrium is equal to $(F_{fr})_{i+1}$. As f can not exceed $(F_{fr})_{i+1}$ any further increase in Q must be equilibrated by a change in q_{dowel}, which will result in a change in the slip as can be seen by the load path beyond point D in Fig. 4.4. In fact, the unloading path D-E-F-G in Fig. 4.4 is the same as A-B-O-C in Fig. 2.6. After point D is reached, q_{dowel} reduces in order to maintain equilibrium and is equal to $(F_{fr})_{i+1} - Q$, until point E is reached where $Q = (F_{fr})_{i+1}$ and therefore q_{dowel}

= 0 and all of the slip is recovered at point F. Finally, as Q continues to increase to Q_{i+1}, q_{dowel} increases in the opposite direction of $(q_{dowel})_i$ until point G is reached where $(q_{dowel})_{i+1} = Q_{i+1} - (F_{fr})_{i+1}$ and the slip increases proportionately in the opposite direction to the final value of s_{i+1}.

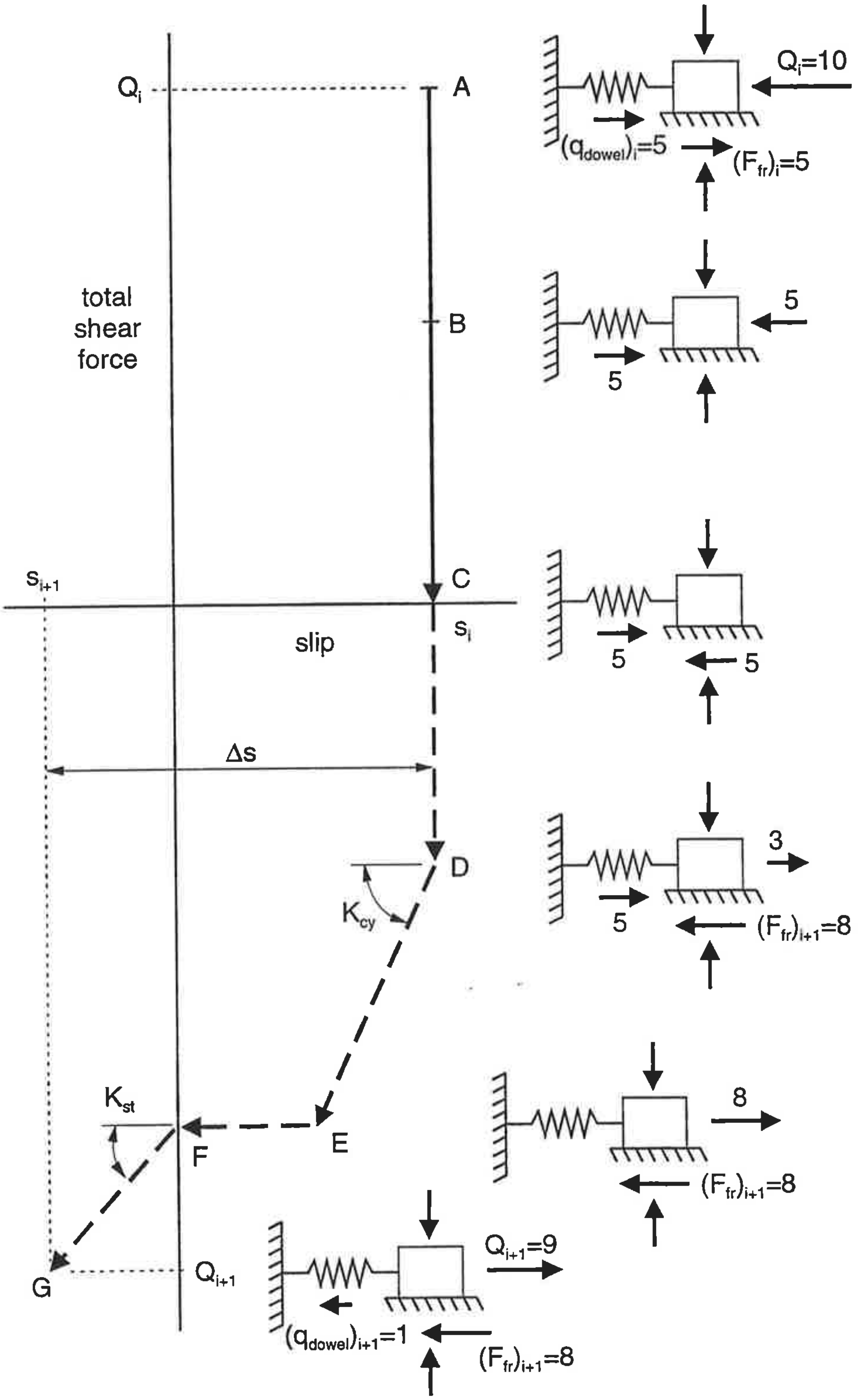

Figure 4.4: General load-slip path when Q reverses direction.

Load-slip paths other than that shown in Fig 4.4 are of course possible. Potential differences include the location of point D along the unloading path, where $(F_{fr})_{i+1}$ is first exceeded (if friction is at all present) and q_{dowel} begins to unload and eventually reverse direction (assuming Q_{i+1} is large enough).

4.3 FINITE ELEMENT MODEL

The linear-elastic finite element formulation was discussed in Section 2.7. This section deals with the non-linear secant stiffness approach that was developed in order to model effects of friction along with the load-slip characteristics of stud shear connectors. This is accomplished by modeling the shear connection along the steel-concrete interface with a set of three spring elements, which are described in the following section.

4.3.1 Non-linear finite element model of the shear connection

The distribution of stud shear connectors is modeled using a set of three independent spring elements, as shown in Fig. 4.5, connecting each corresponding steel and concrete node along the interface.

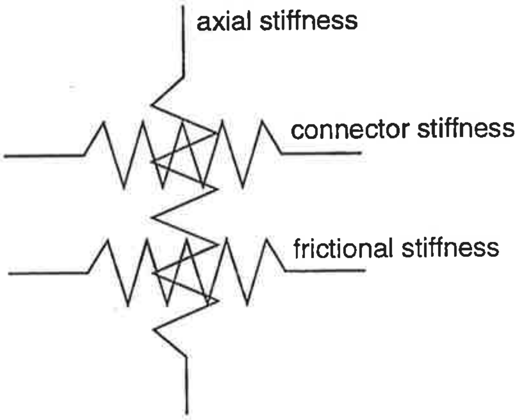

Figure 4.5: Non-linear spring element configuration.

As was the case with the linear finite element formulation (Section 2.7) a single vertical spring is used to represent the axial stiffness of the connectors and the surrounding concrete. The stiffness is assumed to remain constant and is made relatively large as the shear connectors are designed to resist axial loads and prevent separation of the steel and concrete components along the interface.

The two horizontal springs shown in Fig. 4.5 are used to model the combined effect of friction and the non-linear load-slip relationship of the connectors. The effects have been separated in order to avoid the possibility of a *negative* secant stiffness as the load-slip path can pass through the second quadrant (Fig. 4.4) when the total longitudinal shear force reverses. The method of determining the stiffness of the two horizontal spring elements is described in the following two sections.

4.3.1.1 *Stiffness of stud shear connectors*

One of the horizontal springs is used to model the shear stiffness of the stud shear connectors where the theoretical load-slip model adopted is that given in Fig. 2.6, ignoring incremental set. The tri-linear finite element model of the load-slip behavior of stud shear connectors used in the computer program is shown in Fig. 4.6. The most significant difference between the finite element model and the theoretical one (Fig. 2.6) is the slope of the unloading portion within the permanent set zone. As preliminary simulations found that a slope of zero caused numerical instabilities in the finite element analysis, subsequent simulations were carried out varying the slope until it was determined that the minimum slope possible is $0.25K_{st}$.

A secant stiffness approach is used in the analysis where the secant stiffness of the connector K_{sec} must be within the bounds $K_{st} \geq K_{sec} \geq 0.25K_{st}$, which requires an iterative approach. If the previous peak load applied to a stud is $(P_{max})_1$ as shown in Fig. 4.6, the cyclic curve A-B-O would be defined. Subsequently, if the load acting on the connector is $Q_i < (P_{max})_1$, the secant stiffness of the connector would be defined by the line passing through O-G where G is the point along A-B-O that corresponds to load Q_i. Alternatively, if a load $(P_{max})_2 > (P_{max})_1$ is applied, $K_{sec} = K_{st}$ and a new cyclic curve is defined as given by C-D-O in Fig. 4.6.

As it is assumed that the behavior of stud shear connectors is the same when the load is reversed, the load-slip curve is also extended into the third quadrant, as shown in Fig. 4.6. If the peak load in the reverse direction is given as $(P_{max})_3$, the cyclic curve in the reverse direction will be defined as E-F-O.

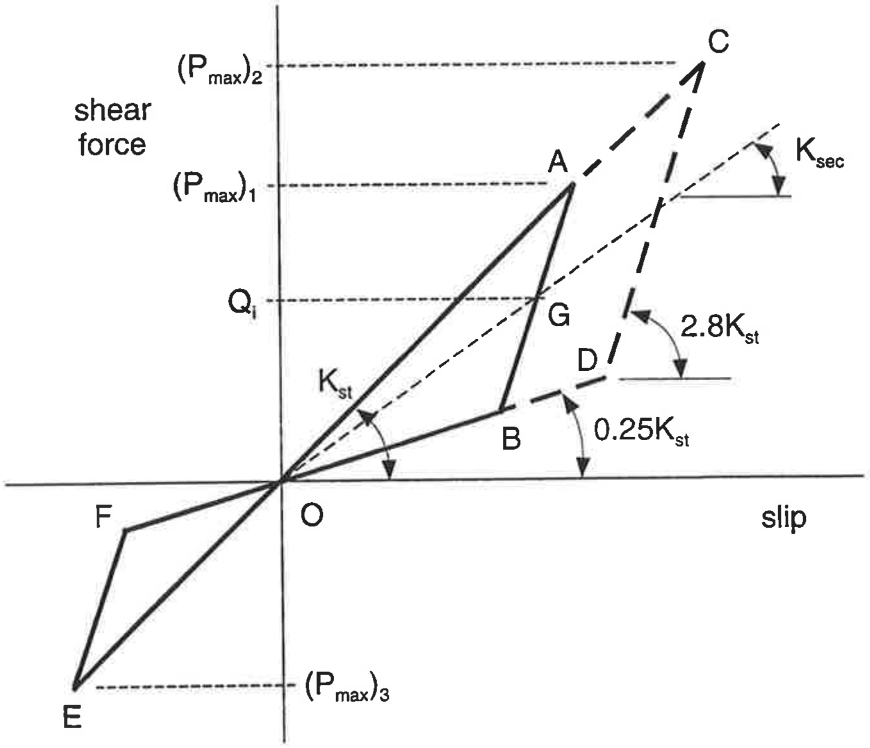

Figure 4.6: Finite element load-slip model of a stud shear connector.

4.3.1.2 *Frictional stiffness model*

The second horizontal spring is used to represent the effect of friction along the steel-concrete interface. The theoretical friction model is shown in Fig. 4.7a where slip can not occur until the shear force exceeds F_{fr}, after which, slip is permitted and there can not be any increase in the frictional resistance.

The infinitely stiff spring that would be required to prevent slip along the interface, within regions of the beam where $Q < F_{fr}$, would have caused numerical instabilities in the finite element simulation. Hence, trial simulations were undertaken to determine the maximum frictional stiffness K_f possible. It was determined that a maximum stiffness of $3K_{st}$, as shown in Fig. 4.7b, which is the model used in the finite element formulation, was suitable to make the slip sufficiently small. Conversely, if Q is greater than F_{fr}, slip would occur and K_f would be determined by the slope of the line defined by O-B in Fig. 4.7b, where point B is dependent on the magnitude of the slip at the connector.

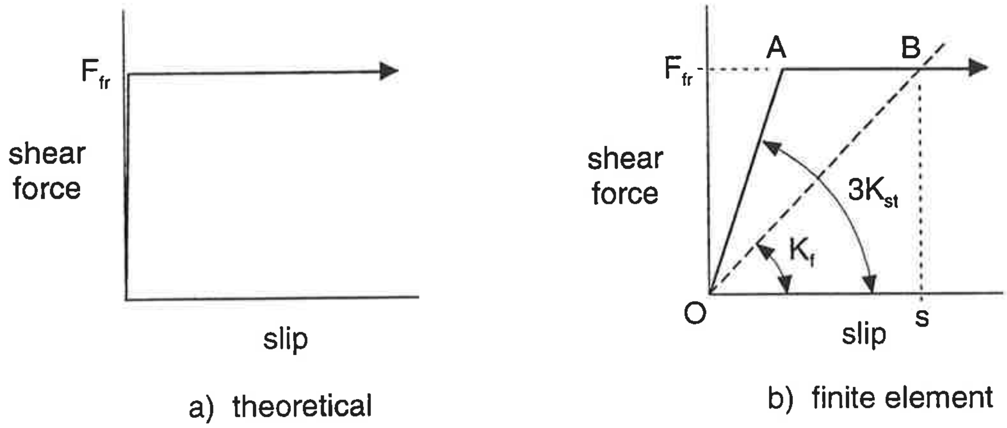

Figure 4.7: Friction model.

If the normal force across the interface at a pair of nodes is such that positive uplift is induced, $F_{fr} = 0$ and, hence, $K_f = 0$ so that the horizontal stiffness of the connection at the nodes is based solely on the stiffness of the connector as defined in the previous section.

4.3.2 Convergence of the non-linear analysis procedure

As was the case with the linear analysis approach described in Section 2.7, a finite element analysis is performed each time the applied load is moved along the length of the beam from the initial node to the adjacent one, known as a load stage, simulating the traversal of a vehicle. With the linear analysis approach, the solution is obtained after the first iteration as the stiffnesses of all the components are assumed to be constant. However, with the non-linear analysis approach presented in this chapter, several iterations are generally required to produce converged results. This is because the stiffness of the shear connection is dependent on the magnitude and orientation of the forces at the interface, all of which are not known at the start of each load stage. Consequently, a method is required to determine when the results have converged so that the iterative procedure may be stopped and the next load stage commenced. The convergence criteria used is based on the total stiffness K_t of each set of horizontal springs located at each node along the interface, where K_t is the sum of the connector stiffness K_{sec} (Section 4.3.1.1) and the frictional stiffness K_f (Section 4.3.1.2). The criteria is in the form of a ratio, which compares K_t of the current iteration i with

K_t of the previous iteration i-1 for the same set of springs, as given by the following equation

$$\text{convergence ratio} = 1 + \left| \frac{(K_t)_{i-1} - (K_t)_i}{(K_t)_i} \right| \tag{4.8}$$

The convergence ratio for each set of springs at every node along the interface is then compared with a convergence limit that is input by the user. When each convergence ratio is less than the prescribed limit, all of the stiffnesses are deemed to have converged and the next load stage can commence. Trial simulations have shown that a convergence limit of 1.001 yields adequately converged results, typically in less than 30 iterations.

4.4 RESULTS OF COMPUTER SIMULATIONS

This section presents a qualitative description of the effect of friction on the range of load resisted by the stud shear connectors using the non-linear finite element procedure developed in this chapter. The results of a finite element simulation are also compared with the simple mathematical model given by Eq. 2.61 that takes into account the effect of friction.

Figure 4.8 shows two distributions of normal force across the interface for a single concentrated load of 320 kN acting at the quarter-span of the 50.4 m long simply supported composite beam (Fig. 3.1). Consistent with the convention adopted, a positive normal force indicates a tensile force across the interface. The broken line represents the distribution resulting from the concentrated load alone, while the solid line is the distribution obtained when the dead load of the concrete is also taken into consideration.

As one might expect, there are large compressive forces in the vicinity of the concentrated load and the supports whether or not the dead load is considered. If, however, the dead load of the slab is ignored (broken line in Fig. 4.8), the normal force across most of the span is negligible, and is in fact tensile in the regions adjacent to the large compressive forces. This suggests that the frictional forces act only locally around load points. When the concrete dead load is taken into account (solid line in Fig. 4.8), the entire distribution becomes compressive and, hence, frictional forces act over the entire span.

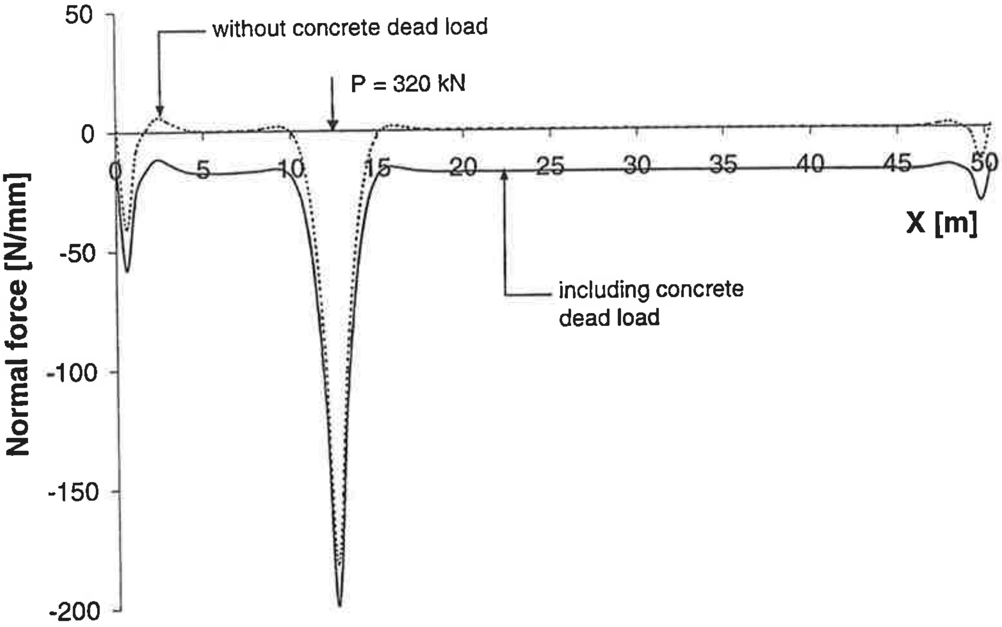

Figure 4.8: Normal force distribution along the steel-concrete interface.

Figure 4.9 shows various shear flow distributions obtained from both linear and non-linear computer simulations of the 50.4 m beam with a concentrated load of 320 kN acting at the quarter-span. The results of the non-linear analyses also take into account the dead load of the concrete component. Considering the total longitudinal shear flow force distribution from the non-linear analysis Q, it can be seen in Fig. 4.9 that the distribution increases locally near the supports and under the load location. In fact, these local increases coincide with the high compressive normal forces shown in Fig. 4.8. As the maximum frictional resistance is large in areas of high normal compression, the frictional stiffness is expected to be very large (Fig. 4.7b). Therefore, it can be concluded that the large shear stiffnesses along the interface, in the areas of high normal compression, attract a greater portion of the total longitudinal shear force. The longitudinal shear force distribution that is resisted by the connectors based on a non-linear analysis q_{dowel} is also shown in Fig. 4.9. The difference between the distributions of Q and q_{dowel} is in fact the frictional force distribution f that is required to maintain horizontal equilibrium along the interface as given by Eq. 4.7. The distribution of q_{dowel} is smooth and continuous throughout the length of the beam except in the vicinity of the concentrated load (Fig. 4.9) where it is equal to zero. As the longitudinal shear force is typically small and the maximum frictional resistance very high near a load point, it may well have been expected that $q_{dowel} = 0$ in the vicinity of a concentrated load.

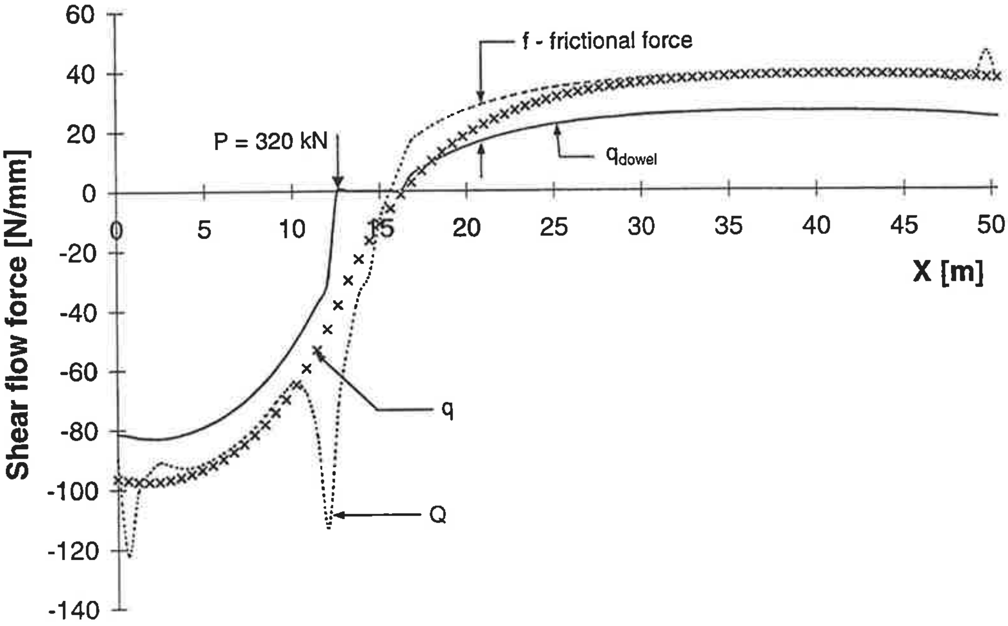

Figure 4.9: Shear flow force distribution along the steel-concrete interface.

Superimposed on the non-linear analysis distributions of Q and q_{dowel} in Fig. 4.9 is the result of a linear analysis q, which is the same distribution shown in Fig. 3.6. The comparison to be made is between the distributions given by q and q_{dowel}, as they predict the magnitude of the shear force acting on the connectors themselves based on the two different analysis approaches. It can be seen that the difference between the q and q_{dowel} distributions is relatively constant over most of the beam. It can therefore be concluded that although the frictional forces are highly concentrated in the vicinity of concentrated loads, the effect on the longitudinal shear force is distributed over the entire span.

To investigate the effect of the non-linear model on the total range, the shear flow force envelope is constructed using the same technique presented in Section 3.2.1.1. Figure 4.10 shows the shear force envelopes for a number of analysis techniques, where the distributions shown for the full-interaction and the linear partial-interaction analyses are the same as those shown in Fig. 3.4. The difference between the full-interaction and linear partial-interaction envelopes shown in Fig. 4.10 has already been quantified in Chapter 3 and consequently, will not be discussed further in this chapter. The primary concern in Fig. 4.10 is the additional reduction in the partial-interaction envelope when the non-linear analysis is performed.

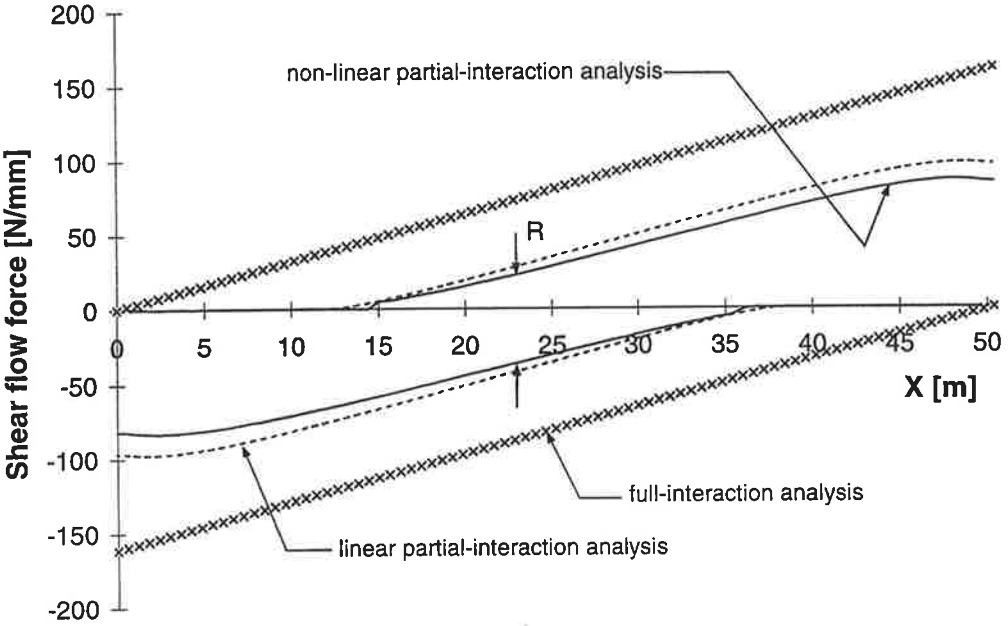

Figure 4.10: Shear flow force envelopes.

Figure 4.10 shows that allowing for the non-linear behavior of the shear connection slightly increases the length of the span subjected to uni-directional ranges. If incremental set were included in the non-linear analysis procedure (Section 2.5.2.2), further redistribution would take place as the number of cycles increases until almost all of the connectors would be subjected to uni-directional ranges as shown in Fig. 2.13. Although the difference between the two sets of partial-interaction envelopes appears to be small, the change in *R* is actually substantial.

Figure 4.11 shows the distribution of *R* resisted by the connectors for various analysis approaches. As was the case in Fig 4.10, the distribution for the full-interaction and linear partial-interaction analyses were previously determined and quantified in Section 3.3.2.1. The difference to note in Fig. 4.11 is the substantial reduction in R from the linear analysis when the non-linear analysis is performed. It is again seen that the difference between the linear and non-linear partial-interaction analysis distributions is almost constant along the span, signifying once again that the effect of friction is global. Although the reduction is not formally quantified, it is worthwhile noting that in this example, the 19% reduction of the non-linear distribution of R, with respect to the linear partial-interaction distribution, increases the fatigue life of the connectors by a factor of approximately $(1.0 - 0.19)^{-5.1} \cong 3$.

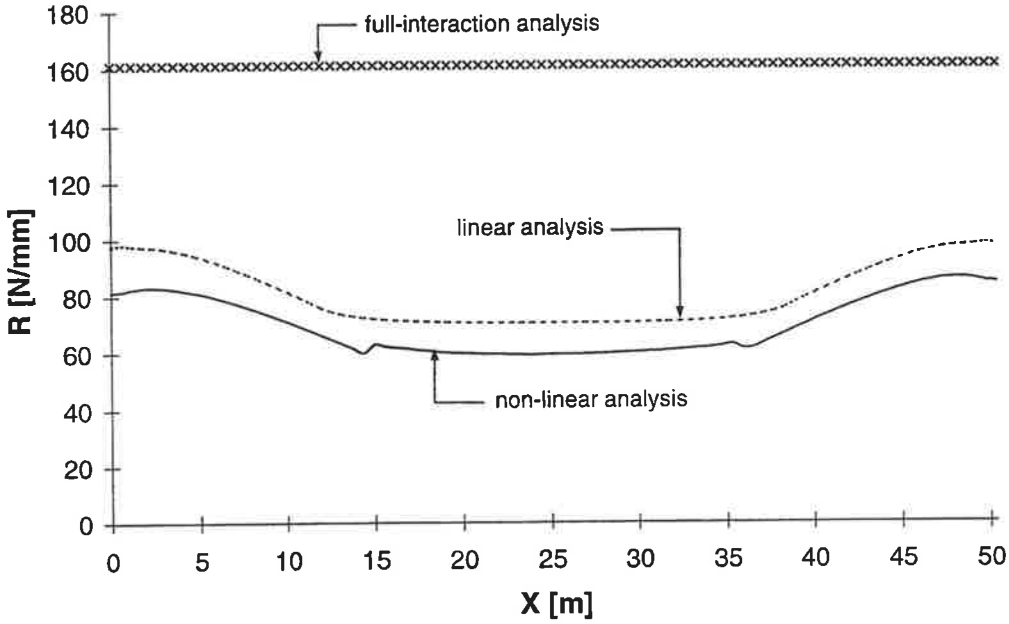

Figure 4.11: Distribution of range.

4.4.1 Comparison with the mathematical model

The following section compares the result of the computer simulations shown in Fig. 4.11 with that of the simple mathematical model given by Eq. 2.61. In the comparison the coefficient of friction is taken as 0.70, which is the minimum of the range given in Section 2.4 and, hence, will result in conservative predictions with respect to the magnitude of R. Furthermore, to simplify the calculations of the mathematical model, the effect of the dead load of the concrete component was ignored

Figure 4.12 superimposes the predictions of the mathematical model (Eq. 2.61) with the results of the computer simulations given in Fig. 4.11. The distribution given by the mathematical model is considerably different to that given by the computer simulations because the former is a full-interaction analysis and the latter are partial-interaction analyses. The mathematical model is conservative over the full length of the beam. The decrease in the range using the mathematical model, with respect to the full-interaction results, is greatest near the supports, which is expected based on the formulation of the model. As the normal forces across the interface are highest and the shear span lengths the shortest when the load is near the supports, the frictional resistance is assumed to be very large resulting in the significant reduction in the range resisted by the connectors.

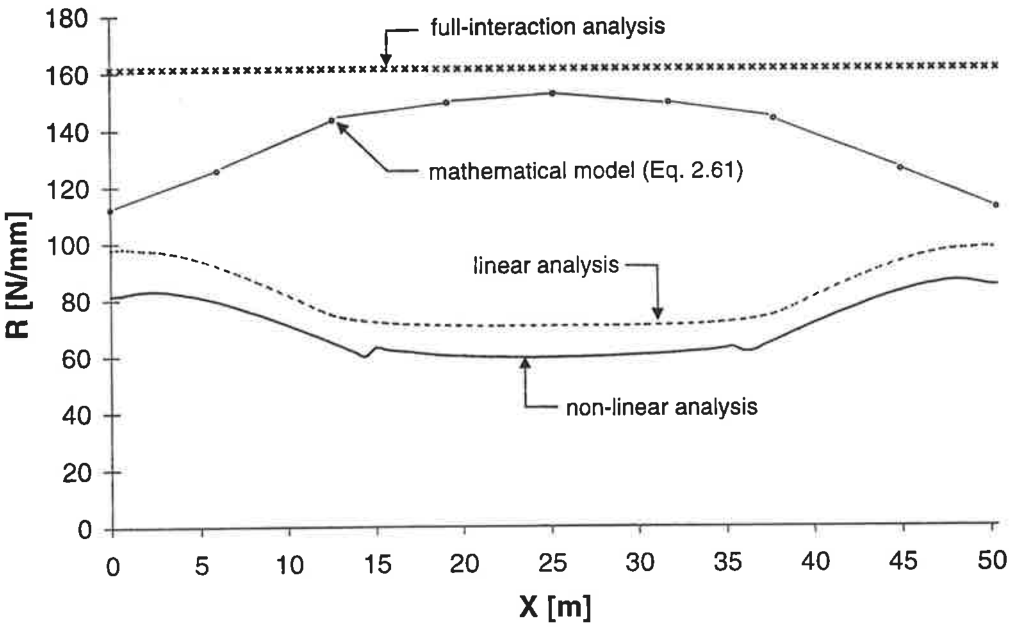

Figure 4.12: Reduction in R using the mathematical model.

To summarize the results of Chapters 3 and 4, there are now four analysis options available for use when predicting the remaining strength and/or endurance of a composite bridge beam, each with a varying degree of complexity and accuracy. Initially, a full-interaction analysis could be preformed, the simplest type of analysis, which would give a safe endurance with respect to the fatigue life of the shear connection. Increasing the level of accuracy somewhat, a full-interaction analysis could be performed taking into account the effect of friction, with little increase in the amount of work required. If a more refined and accurate analysis is required, a linear-elastic partial-interaction analysis could be performed, which would give a much more realistic representation of the distribution of R along the length of the beam. Finally, a non-linear partial-interaction analysis could be performed taking into account friction. This analysis approach could be used to consider the influence of the dead load of the concrete deck, and the weight of the vehicles on the distribution of R resisted by the shear connection.

Chapter 5

Experimental Investigation

5.1 INTRODUCTION

An experimental programme was developed to further investigate the behavior of stud shear connectors subjected to reverse-cycle fatigue loading. In the current investigation, a simple specimen was desired so the manufacturing cost could be kept low and, hence, twenty specimens were cast and tested so that a wide range of load conditions could be applied. It was also decided to subject the specimens to a large number of cycles and, hence, low load ranges, as the shear connection in composite bridges are typically subjected to millions of cycles over the life of the structure.

5.2 EXPERIMENTAL SET-UP

As it is very difficult to simulate the load conditions surrounding the shear connectors in a composite beam using push-out specimens, a simple specimen was designed to allow for a relatively large number of tests so that a reasonable comparison could be made. The variation between various push-out tests, however, can be allowed for by using the ratio R/P_{st}, as suggested in Section 2.5.3.2. Therefore, to apply the results of push-out tests to beams, all what is required is P_{st} for the beam as given by Eq. 2.40.

A top view of the experimental set-up, and a longitudinal section, is shown in Fig. 5.1. A 1900x1400x25 mm thick steel plate was fastened to the strong floor by four tie rods. The plate was used to standardize the placing and removal of specimens. The specimen itself was held in place by four supports located at each corner of the concrete block. The supports were designed to prevent horizontal movement due to the pushing and pulling of the reverse-cycle load as well as vertical movement of the concrete block due to the uplift forces resulting from the eccentric loading.

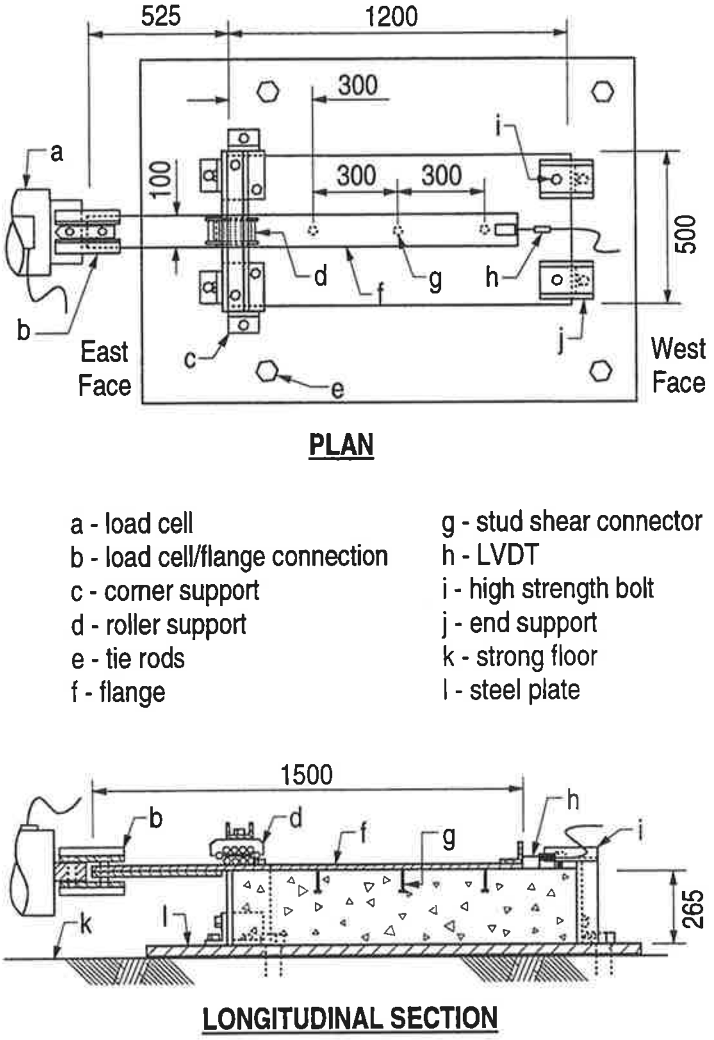

Figure 5.1: Experimental set-up.

The dimensions of the concrete block, 1200x500x265 mm, were primarily governed by the restrictions imposed by the minimum height of the INSTRON hydraulic actuator and the location of the supports on the strong floor. It was determined (Oehlers and Bradford 1995) that no reinforcement was required to prevent splitting of the concrete, however, a nominal amount was included to provide anchorage for the lifting hooks used to move the specimens. No reinforcement was placed in the vicinity of the connectors to ensure that the fatigue strength would not be affected.

Three stud shear connectors, 75x12.7 mm diameter, were supplied and welded onto a steel plate (flange) at 300 mm spacing by a local contractor and embedded in the concrete. It was decided to use more than one stud to reduce the scatter of results; three studs were used, which was limited by the capacity of the load cell. The 1500x100x10 mm thick flange extended approximately 525 mm beyond the East face of the concrete block to provide the connection between the load cell and the specimen.

An additional 500x100x12 mm thick plate was welded to the under-side of the protruding flange in order to stiffen the connection and to lower the line of action of the applied force so that the eccentricity could be minimized. The eccentricity, e, shown in Fig. 5.2, is due to the line of action of the resultant bearing forces acting on the studs, δQ, being offset from the line of action of the applied load, Q. The resulting moment due to the eccentricity is in turn resisted by a set of tensile and compressive forces, F_T and F_C respectively, acting on the end studs. The orientation of the forces depending on whether the applied load is pushing or pulling. In an attempt to minimize the uplift of the flange, a roller was placed over it near the East face of the specimen as shown in Fig. 5.1.

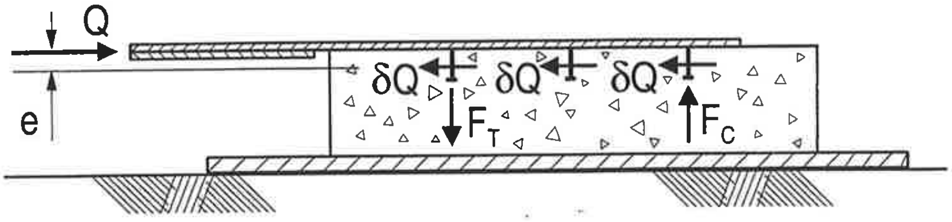

Figure 5.2: Uplift forces due to eccentric loading.

The flange was attached to the load cell with two 25 mm diameter high strength aluminium pins and was isolated from the load cell by a spherical bearing. The bearing was used to prevent the transfer of any vertical and rotational movement of the flange to the actuator, which could damage the seals. As the pins were machined to produce a tight fit, in order to minimize any play in the horizontal direction, it was necessary to replace the pin after lengthy fatigue tests due to wear of the pin.

The load cell was fastened to the face of the actuator which was in turn connected to a stiff reaction frame that can be can be seen on the left side of Fig. 5.3 which shows an overall view of the experimental set-up.

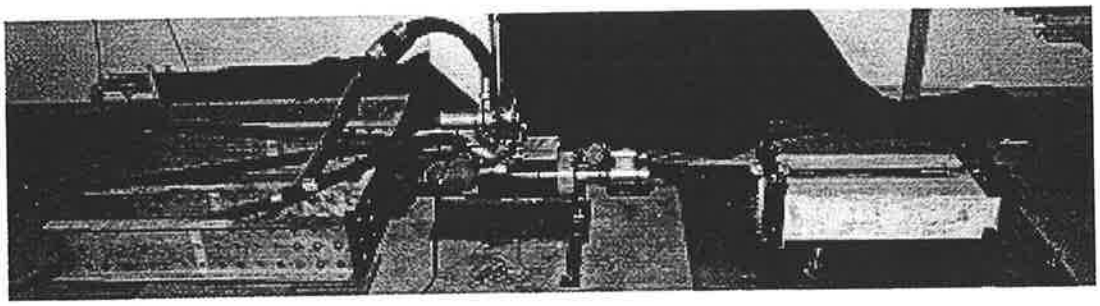

Figure 5.3: Overall view of experimental set-up.

A Linear Variable Displacement Transducer (LVDT) was glued to the concrete near the West end of the flange (Fig. 5.1) so that the relative movement between the steel and concrete, or slip, could be measured as the cyclic or static loads were applied. The data acquisition system used Visual Designer to convert the analogue data from the load cell and the LVDT to digital format which was saved in a PC file.

5.2.1 Casting procedure

Figure 5.4 is a photograph of a section of the formwork ready for casting. Two concrete pours were required to produce the twenty specimens, ten in each pour. The specimens were cast with the steel flange on the bottom and the studs orientated vertically upwards as is the case with composite bridge beams. This was done to ensure that the concrete surrounding the studs could be adequately compacted as the quality of the concrete in the area influences the strength of the connection significantly (Johnson 1994). The specimens were rotated to the orientation shown in Fig. 5.1, as required for testing, using four lifting hooks and a crane. A layer of 10 mm thick styrofoam was placed in the formwork around the flange so that when orientated in the testing position, the top of the concrete would not extend above the bottom of the flange. The face of the flange on the steel-concrete interface was coated with a thin layer of grease to prevent chemical bonding with the concrete and reduce frictional forces along the interface that may be present during testing. The formwork was coated with oil to ease the stripping of the specimens and permit the use of the same formwork for the second pour.

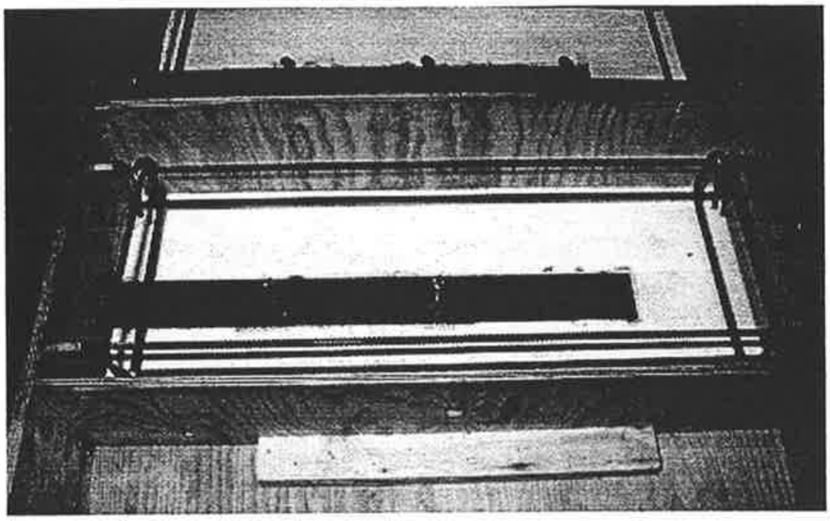

Figure 5.4: Formwork ready for concrete pour.

5.2.2 Material properties

The shank of four studs was machined to produce tensile coupons so that the ultimate strength could be determined. The coupons were tested by applying a monotonically increasing tensile force until failure. The maximum loads were recorded and are shown in Table 5.1 where the average ultimate strength f_u is 432.9 MPa. The flanges were center-punched to mark the location of the studs and the surrounding surface was cleaned from any oil and dust so that the studs could be welded onto the flange. A local contractor welded the studs, and the quality of the welds was tested by hammering five studs that were welded on sample steel plates as shown in Fig. 5.5. As none of the studs 'popped-off', it was concluded that the welds were adequate.

Table 5.1: Results of tension tests on stud shear connectors.

Specimen	f_u [MPa]
1	427.9
2	429.3
3	435.5
4	438.7

a) prior to hammer test

b) after hammer test

Figure 5.5: Evaluation of weld quality.

A 25 MPa concrete strength was specified for the two pours with a maximum aggregate size of 10 mm and a slump of 80 mm, which was purchased from a local ready-mix supplier. The concrete was vibrated using a hand held pneumatic vibrator and the surface of the concrete was hand finished. Twenty five 200x100 mm diameter cylinders were also cast at the same time. The specimens were then covered with plastic sheets for approximately 24 hours, after which the cylinders were stripped, labeled and moved into a fog room. The specimens were stripped approximately one week after casting in order to allow the concrete to gain enough strength to permit handling. The specimens were labeled and stored until testing. A similar procedure was adopted for the second pour, which took place approximately six weeks later.

All of the specimens from the first pour, P1, were tested first and the age of the specimens, from the casting date, ranged from 92 to 223 days. The age of the specimens at time of testing for the second pour, P2, ranged from 153 to 267 days. At various stages throughout the testing phase, a series of cylinders were tested to determine the concrete compressive and tensile strength. A summary of the results is given in Table 5.2, where the average f_c = 35.2 MPa and f_t = 3.3 MPa for P1 and the average f_c = 40.2 MPa and f_t = 4.3 MPa for P2.

Table 5.2: Concrete properties.

Cylinder	Pour 1			Pour 2		
	age [days]	f_c [MPa]	f_t [MPa]	age [days]	f_c [MPa]	f_t [MPa]
1	92	33.2	3.1	153	N/A	4.1
2	92	32.1	3.3	153	42.5	3.6
3	92	34.6	3.3	153	39.2	4.5
4	92	32.6	-	153	40.1	-
5	223	36.5	2.7	267	N/A	4.8
6	223	37.1	3.7	267	40.2	4.3
7	223	38.6	3.6	267	38.8	4.3
8	223	36.5	-	267	40.2	-

5.2.3 Testing procedure

The cyclic frequency was kept constant at 0.5 Hz throughout the test except when readings were taken. When readings were taken, at regular intervals throughout each test, the frequency was reduced to 0.05 Hz so that a suitable number of data points could be obtained to define the load-slip curve.

A summary of the tests carried out on the various specimens is shown in Table 5.3, where the loads shown are the total loads applied by the actuator. The maximum load shown is the peak load applied, or in the case of the static tests, it represents the static strength of the specimen when pulled monotonically to failure. The range is defined as the difference between the maximum and minimum loads applied, and the last column is the number of cycles that were required to cause failure in the fatigue tests.

5.3 RESULTS

Three specimens were used to test the rig in order to solve any problems that were not accounted for in the initial design. For example, the initial design did not include the spherical bearing in the load cell-flange connection and the roller support over the flange (see Fig. 5.1), which were added in order to eliminate axial tensile forces in the studs that resulted from vertical uplift of the flange.

Table 5.3: Loading pattern.

Specimen	Load type	Maximum Load [kN]	Range [kN]	No. of cycles to failure (x10^3)
F1-P1	Reverse	20	40	938.0
F2-P1	Reverse	25	50	658.3
F3-P1	Reverse	30	60	60.0
F4-P1	Reverse	35	70	19.8
F5-P1	Uni-directional	70	60	15.8
F6-P1	Uni-directional	60	50	86.8
S1-P1	Static	149.0		
S2-P2	Static	151.8		
F7-P2	Uni-directional	50	40	555.2
F8-P2	Reverse	25	50	233.1
F9-P2[1]	Reverse/Static	25/110.0	50	(616.8)
F10-P2	Uni-directional	60	50	95.5
F11-P2	Reverse	37.5	50	698.7
F12-P2	Reverse	37.5	50	197.5
F13-P2	Reverse	25	50	661.5
F14-P2	Reverse	42.5	50	50.0
F15-P2	Reverse	42.5	50	78.2

[1] stopped cycling at 616.8x10^3 cycles then loaded statically to failure at 110.0 kN

5.3.1 Static test results

The load-slip curves of the two static tests, S1-P1 and S2-P2, are shown in Fig. 5.6. These tests involved increasing the load monotonically, under displacement control, until failure. Failure of S1-P1 occurred at a load of 149.0 kN, while S2-P2 failed at a load of 151.8 kN. As the difference between the two static strengths is small, it was concluded that the slightly higher concrete strength of pour two had a minimal effect on the overall behavior. Therefore, the average static strength of the specimens was taken as the average of the two tests, 150.4 kN, which is within 15% of the predicted strength $(P_{st})_{push}$ = 176 kN that was calculated using Eq. 2.39 with n taken as ∞ to give the mean strength.

The static strength of a stud shear connector in a beam can be predicted using Eq. 2.40 where taking n as ∞ gives $(P_{st})_{beam}$ = 143 kN which is less than 5% below the experimental average of 150.4 kN. This suggests that the net axial force acting on the connectors in the current experimental set-up is very nearly zero rather than being compressive which is observed in standard push-out tests.

Unfortunately, the extension of the LVDT used to record the slip was not long enough to record the post-failure behavior, where a softening branch of the curves would have been seen in Fig. 5.6. The ductility of the shear connection is, however, shown by the extent of the yield plateau, both extending well beyond 5 mm.

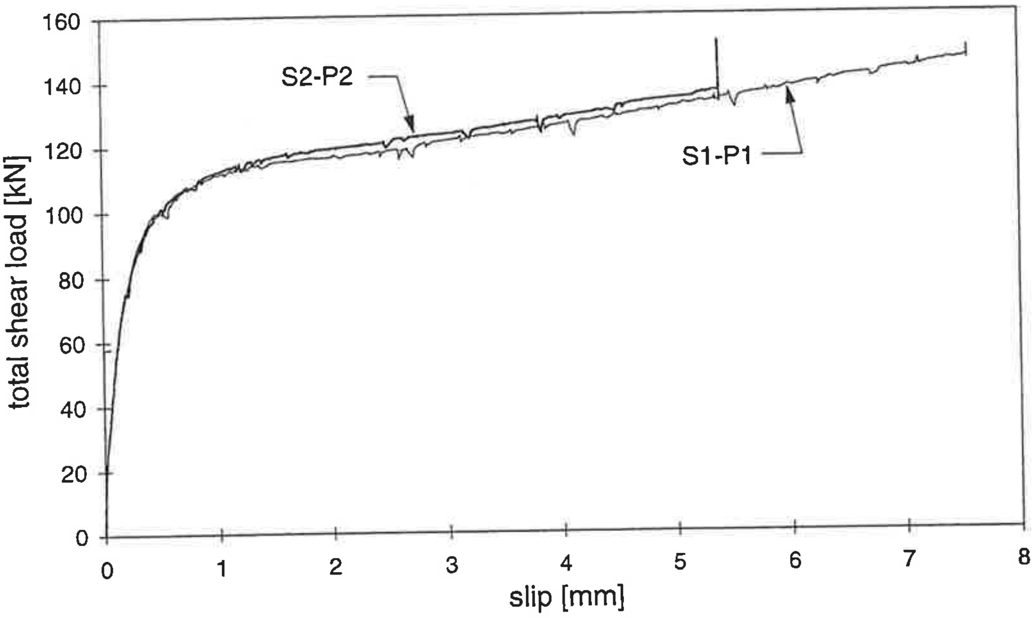

Figure 5.6: Monotonically increasing static load test.

5.3.2 Cyclic test results

A total of 15 cyclic tests were performed, 4 of which were uni-directional. A typical load-slip curve, from specimen F7-P2, is shown in Fig. 5.7. It can be seen that P_{max} was 50 kN for this specimen and R was 40 kN, which is the difference between the maximum and minimum load of the cycle. The slip shown is that of the unloading branch of the cycle, and the numbers above each branch indicate the number of cycles that have elapsed when the reading was taken. Figure 5.7 clearly shows that the slip increases as the number of cycles increase, which is referred to as the incremental set. The initial loading curve from the mean load of 30 kN to the peak load of 50 kN of the first cycle is also shown to illustrate the transition from static loading to cyclic loading.

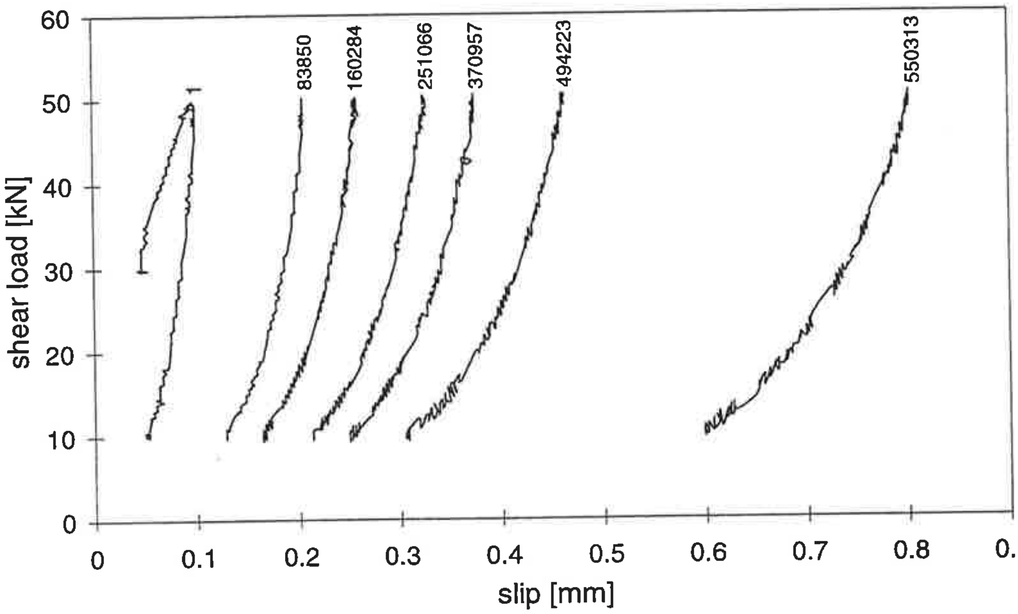

Figure 5.7: Uni-directional load-slip curves of specimen F7-P2.

Another way of representing the data presented in Fig. 5.7 is by plotting the maximum slip against the number of cycles elapsed, N, as shown in Fig. 5.8. Figure 5.8 illustrates that the rate of increase in slip is constant over most of the fatigue life of the shear connection, as indicated by the broken line. There is a rapid increase in the slip at the start of the fatigue life where the initial softening of the connection takes place prior to stabilizing. The damage that occurs involves local crushing or powdering of the concrete in the vicinity of the connector and the initiation and propagation of fatigue cracks within the connector or the steel flange near the weld collar. More significantly, it is evident that the maximum slip, hence, the incremental set and the fatigue damage increase very rapidly near the end of the fatigue life of the connection, providing a reasonable amount of warning of eminent failure. A more detailed analysis of the shape of the slip-N curve is given in Section 5.4.2.

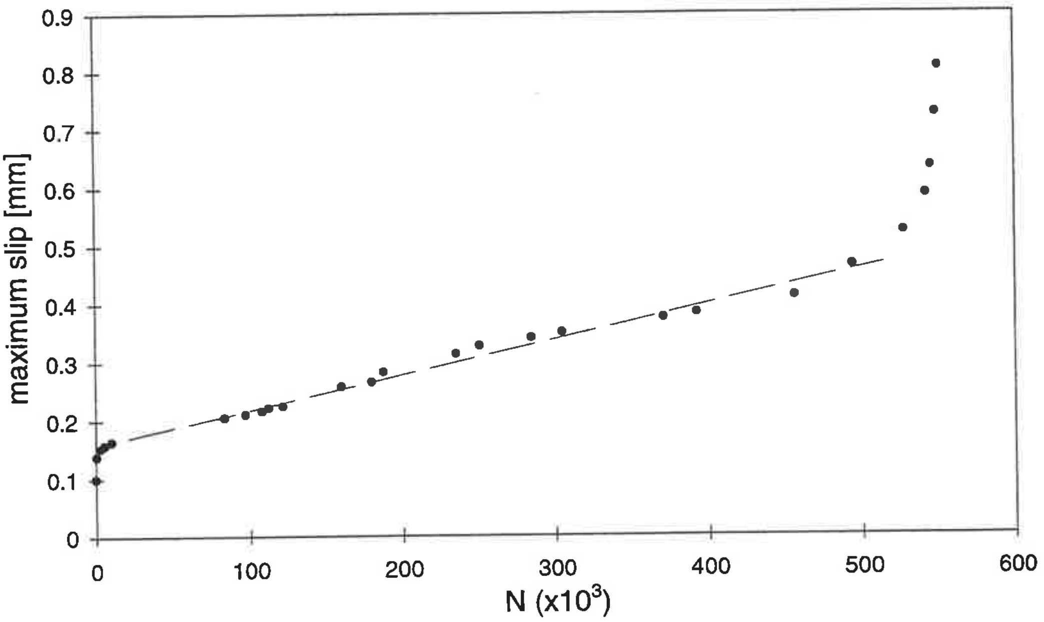

Figure 5.8: Uni-directional slip-N curve of specimen F7-P2.

The results of the remaining three uni-directional cyclic tests are similar to those shown in Figs 5.7 and 5.8 and, hence, are given in Appendices A and B along with the other results not discussed in this section. Figures 5.9 and 5.10 show the curves obtained for the reverse-cycle case using the results of specimen F13-P2. This specimen failed in fatigue after $661.5\text{x}10^3$ cycles and was subjected to a range of 50 kN with a maximum positive load of 25 kN, so that the ratio P_{max}/R was equal to 0.5.

Figure 5.9 shows the load-slip curve where a positive shear load represents the pull branch of the cycle meaning that the load was orientated such that the actuator was pulling on the flange of the specimen. The behavior is similar to that of Fig. 5.7 for the uni-directional case, and the results are again shown for the unloading branch of the cycle in both directions.

Assuming everything being equal, one would expect the slip to be equal in both the push and pull branches of a cycle. However, as Fig. 5.9 clearly shows, the slip was greater in the pull portion of the cycle implying that the fatigue damage was greater on the East side of the connectors. Of the six reverse cycle tests performed where P_{max}/R is 0.5 and in which the fatigue damage is expected to be equal in both directions of a cycle, larger slips were recorded for the pull branch in four of the tests. It may be that the experimental set-up induced somewhat more adverse effects during the pull branch of a cycle. Unfortunately, insufficient tests are available to confirm this hypothesis.

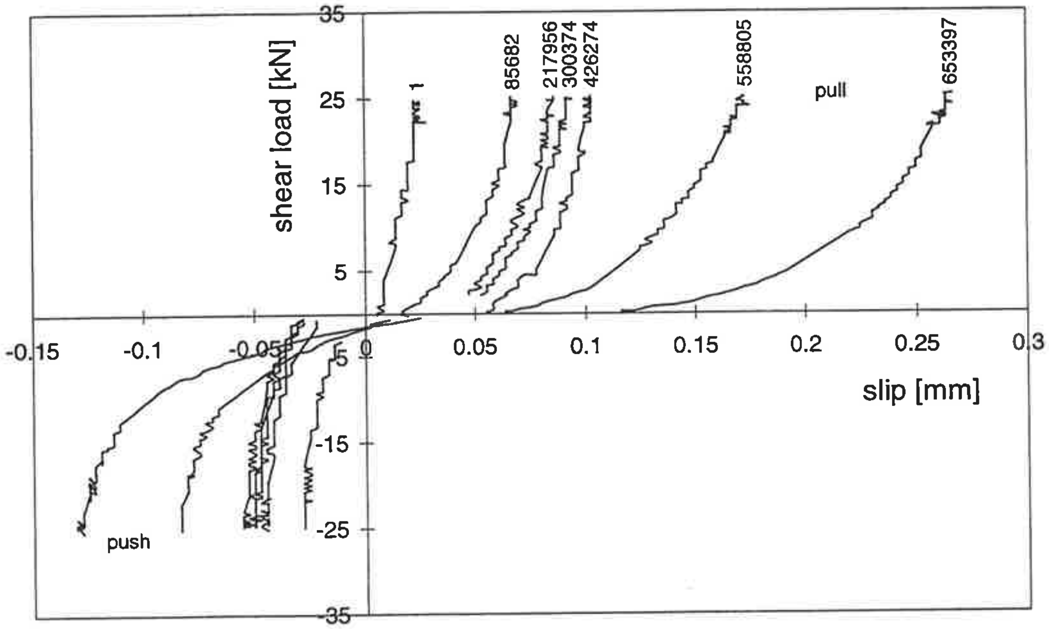

Figure 5.9: Reverse-cycle load-slip curves of specimen F13-P2, $P_{max}/R = 0.5$.

When the maximum positive and negative slips of each cycle are plotted against N, the curves shown in Fig. 5.10 are obtained. The shape of the curve for both the pull and push branches of the cycle is similar to that of the uni-directional case (Fig. 5.8) with a constant rate of increase of slip over most of the fatigue life. As was noted in Fig. 5.9, the slips recorded during the pull branch of the cycle were consistently greater than those of the push branch. However, it is interesting to note that the slip begins to increase rapidly in both of the branches at approximately the same time.

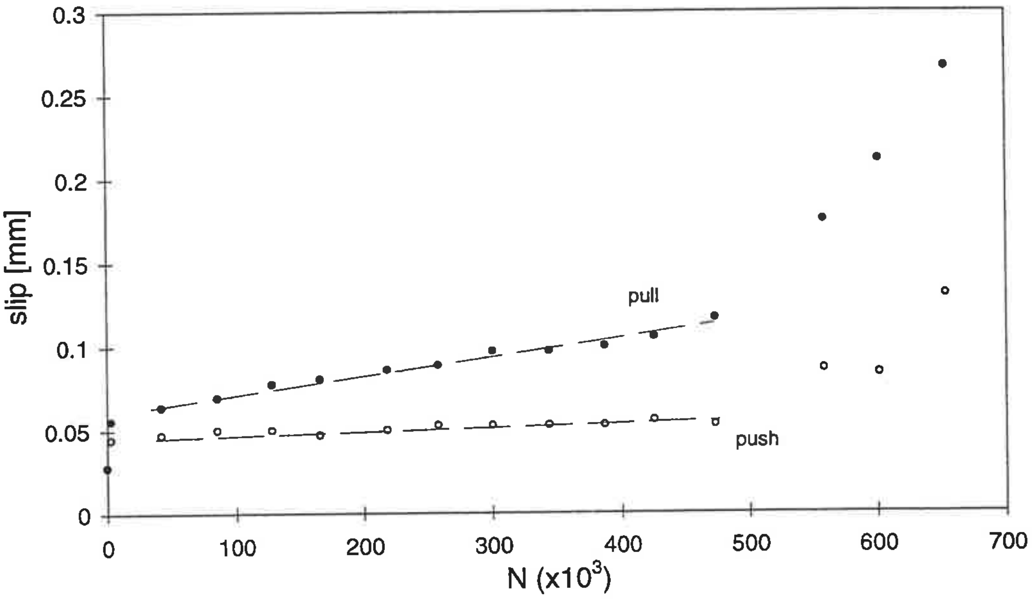

Fig. 5.10: Reverse-cycle slip-N curves of specimen F13-P2, $P_{max}/R = 0.5$.

Figure 5.11 shows the load-slip curve for the unloading branch of the cycle in each direction for specimen F11-P2, where R = 50 kN and P_{max}/R = 0.75. Failure occurred in the pull portion of the cycle, after 698.7x10^3 cycles, as would be expected due to the larger maximum positive load.

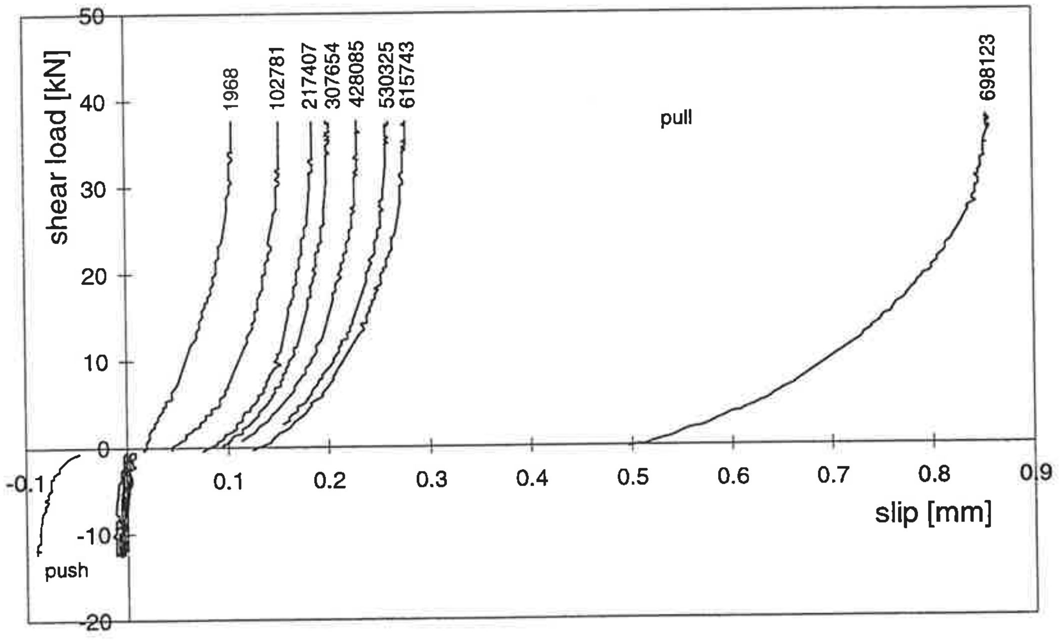

Figure 5.11: Reverse-cycle load-slip curves of specimen F11-P2, $P_{max}/R = 0.75$.

Figure 5.12 shows the maximum slip-N curves for the pull and push cycles of specimen F11-P2, which again exhibits the same behavior as that observed in Figs 5.8 and 5.10 for the uni-directional and $P_{max}/R = 0.5$ cases respectively.

The significant observation to make in Fig. 5.12 is that there is very little fatigue damage occurring in the push branch of the cycle as the slip is very nearly equal to zero throughout the fatigue life. This may lead to the suggestion, that for values of P_{max}/R greater than about 0.75, the fatigue behavior can be considered to be uni-directional.

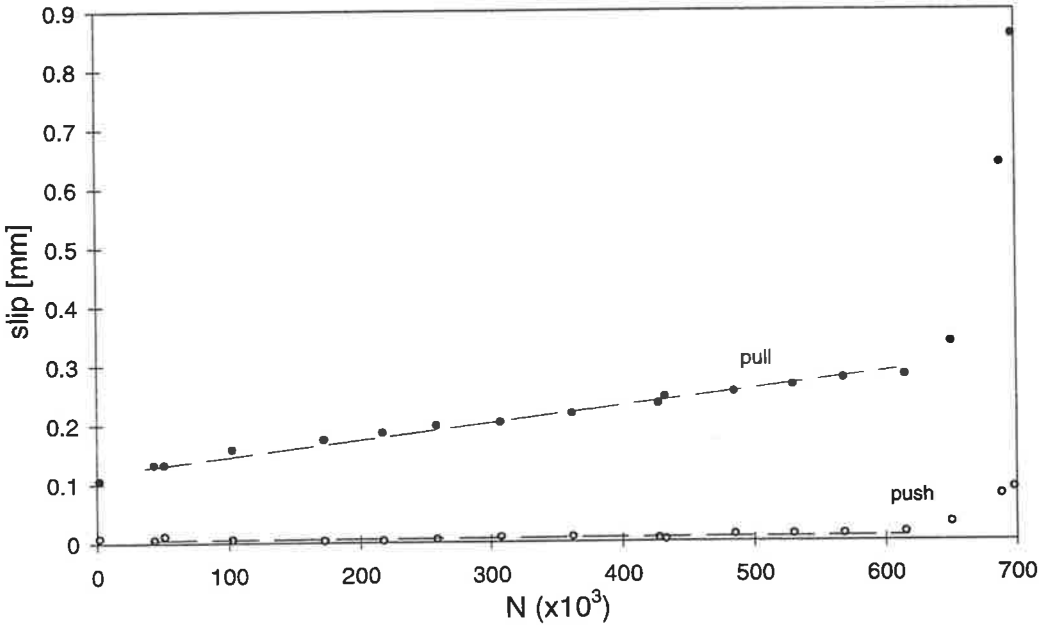

Figure 5.12: Reverse-cycle slip-N curves for specimen F11-P2, $P_{max}/R = 0.75$.

5.4 ANALYSIS OF RESULTS

The results of the current investigation are compared with those obtained by Slutter and Fisher in 1966 and by Mainstone and Menzies in 1967. The parts of the tests that can be compared with the current investigation have been summarized Section 2.6.1.

Unfortunately, static tests of the specimens tested by Slutter and Fisher (1996) were not performed, however, sufficient information was given so that Eq. 2.39 could be used to estimate the static strength of the specimens. For the A- and B-series specimens shown in Table 2.3, a static strength of 439 kN is predicted given that the average $f_u = 410$ MPa and $f_c = 29.0$ MPa, and n was taken as ∞ to obtain the mean strength of the four 19 mm studs that were used in each specimen. As $f_u = 450$ MPa for the 22 mm studs, the static strength for the G- and H-series specimens also shown in Table 2.3 is predicted to be 658 kN using Eq. 2.39, given that the average $f_c = 31.8$ MPa, and again taking n as ∞.

5.4.1 Asymptotic endurance of experimental results

In order to determine E_a, two points along the failure envelope shown in Fig. 2.8 are required so that it can be extrapolated to the horizontal axis, as indicated by the broken portion of the failure envelope.

For the current experimental results, and those taken from Slutter and Fisher and Mainstone and Menzies, the two points along the failure envelope are defined by the static strength of the specimens $(0,P_{st})$, and by the maximum load applied during the fatigue test (N_{exp},P_{max}). The asymptotic endurances determined for the current investigation are determined using the results given in Table 5.3 and are shown in Table 5.4. The asymptotic endurance for the results of the other researchers were determined using Tables 2.3 and 2.4 and are summarized in Table 5.5.

Table 5.4: Asymptotic endurances.

Specimen	Load Type[1]	E_a (x10^3)
F1-P1	R	1081.9
F2-P1	R	789.5
F3-P1	R	75.0
F4-P1	R	25.8
F5-P1	U	29.6
F6-P1	U	144.4
F7-P2	U	831.7
F8-P2	R	279.6
F9-P2	R	2296.2
F10-P2	U	158.9
F11-P2	R	930.8
F12-P2	R	263.1
F13-P2	R	793.4
F14-P2	R	69.7
F15-P2	R	109.0

[1] R - reverse-cycle
U - uni-directional

Table 5.5: Asymptotic endurances for other researchers.

a) Slutter and Fisher

Specimen	Load Type[1]	E_a ($\times 10^3$)
a1A	R	1934.7
b1A	R	2407.3
c1A	R	3117.0
a2A	R	139.7
b2A	R	140.0
c2A	R	228.6
a3B	U	205.7
b3B	U	169.3
c3B	U	294.4
a4B	U	68.5
b4B	U	83.7
c4B	U	96.9
e1G	R	1261.1
e2G	R	283.1
e3H	U	158.9
e4H	U	51.4

[1] R - reverse-cycle
U - uni-directional

b) Mainstone and Menzies

Specimen	Load Type[1]	E_a ($\times 10^3$)
S10	U	4533.3
S12	U	2260.5
S13	R	774.5
S14	R	260.8
S15	R	591.3
S17	R	2629.2
S18	R	135.8
S20	U	2903.5
S21	R	31.2
S23	U	3172.5
S24	U	50.0
S25	U	97.0
S27	U	48.8
S28	U	32.6
S30	U	71.3
S31	U	41.5
S32	U	1203.3
S33	U	660.7
S34	R	23.7

Based on Eq. 2.45, the asymptotic endurance can be plotted against the non-dimensional parameter R/P_{st}. Figure 5.13 plots the $\log(E_a)$ vs $\log(R/P_{st})$ data for the current investigation along with the asymptotic endurances predicted by Eq. 2.45. The mean endurance line is determined using Eq. 2.45 with $n = \infty$, which represents the case when all of the connectors fail as a group. The two characteristic endurance bounds represents the endurance of a single connector, hence, $n = 1$ in Eq. 2.45. The coefficients shown beside the reverse-cycle data points are the P_{max}/R values.

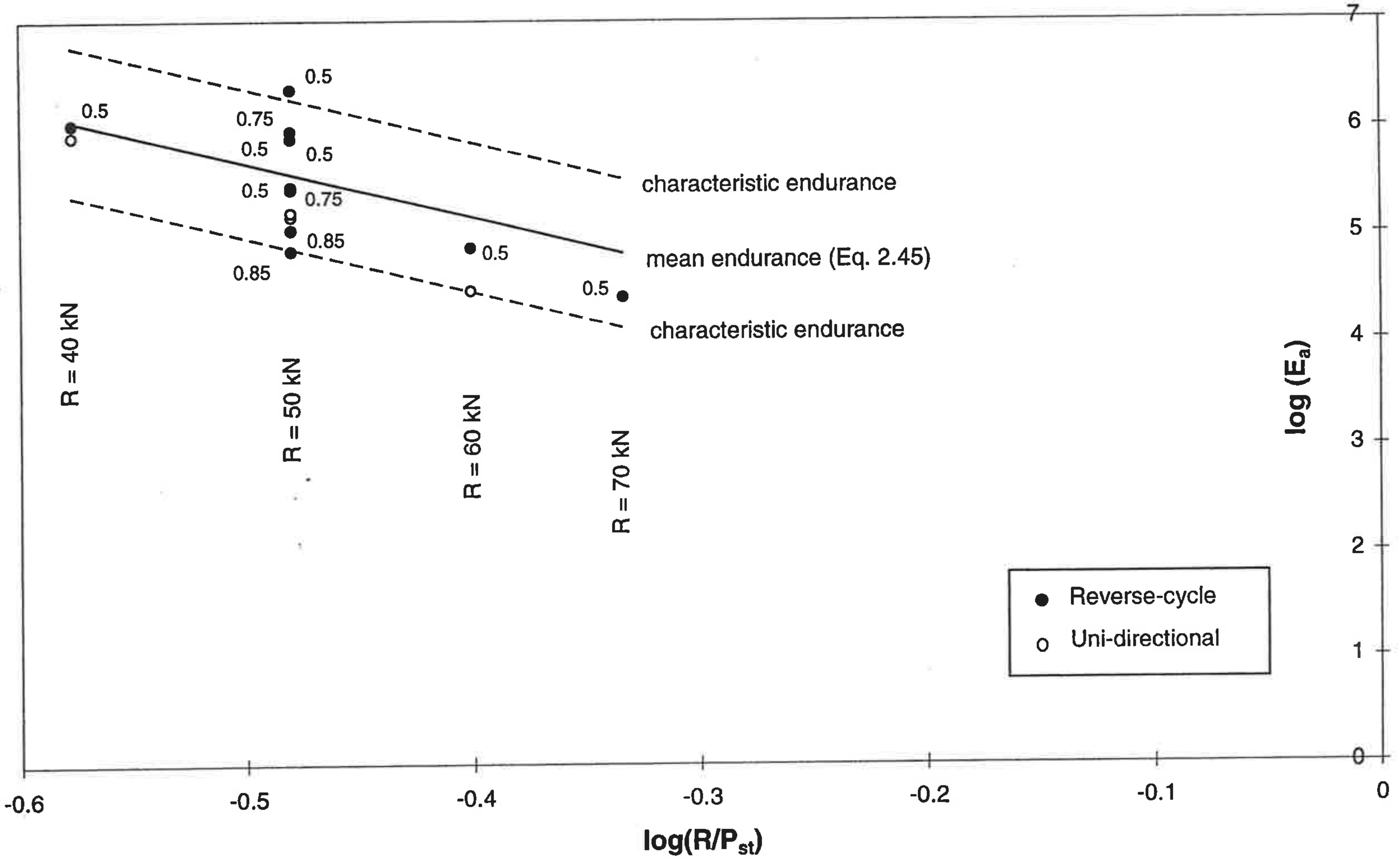

Figure 5.13: Log(E_a) vs log(R/P_{st}) for the current investigation.

The results fall within the bounds defined by the characteristic endurance (Fig. 5.13), with the exception of one test, that of specimen F9-P2 which was loaded monotonically until failure after 616.8x10^3 cycles. It can also be said that all of the reverse-cycle tests have higher endurances than the corresponding uni-directional test with the exception of the two tests where $P_{max}/R = 0.85$.

Figure 5.14 shows the results of Slutter and Fisher and Mainstone and Menzies superimposed on the results of the current investigation (Fig. 5.13). The behavior observed with the other researchers is similar to that of the current investigation where in general, the fatigue life of the reverse-cycle specimens is longer than that of the uni-directional ones. Most of the results from the other researchers also fall within the bounds defined by the characteristic endurance lines, and the scatter is also similar to that observed in Fig. 5.13. This provides some degree of reassurance that the current results obtained are reliable.

In order to give a better feel for the scatter in the test results and the actual increase in the asymptotic endurance under reverse-cycle loading, the increase in E_a is plotted against the ratio R_u/R. This is shown in Fig. 5.15, where R_u is defined as the magnitude of the range in the positive branch of the cycle only. The term R_u is introduced so that the ratio would equal 1.0 for the uni-directional case, opposed to using P_{max} where the ratio P_{max}/R would, in general, be greater than 1.0 for the uni-directional case. The increase in the asymptotic endurance is defined by the ratio, $E_a/(E_{au})_{avg}$, where the denominator is the average asymptotic endurance of all the uni-directional tests performed for the corresponding range. As it is necessary that both the reverse-cycle and uni-directional tests have the same total range, only the results from Slutter and Fisher could be used in this comparison.

Figure 5.15 clearly shows that the endurance of stud shear connectors is increased under reverse-cycle loading compared to the uni-directional case with the same total range. The increase in E_a also appears to increase as R_u/R approaches 0.5. It is also evident that there is a significant amount of scatter in both test results, more so, however, with the current investigation. A certain amount of scatter is inevitable with all forms of testing, however, it is more pronounced with fatigue tests especially in the reverse-cycle case where additional problems are encountered as the cycle passes through zero load.

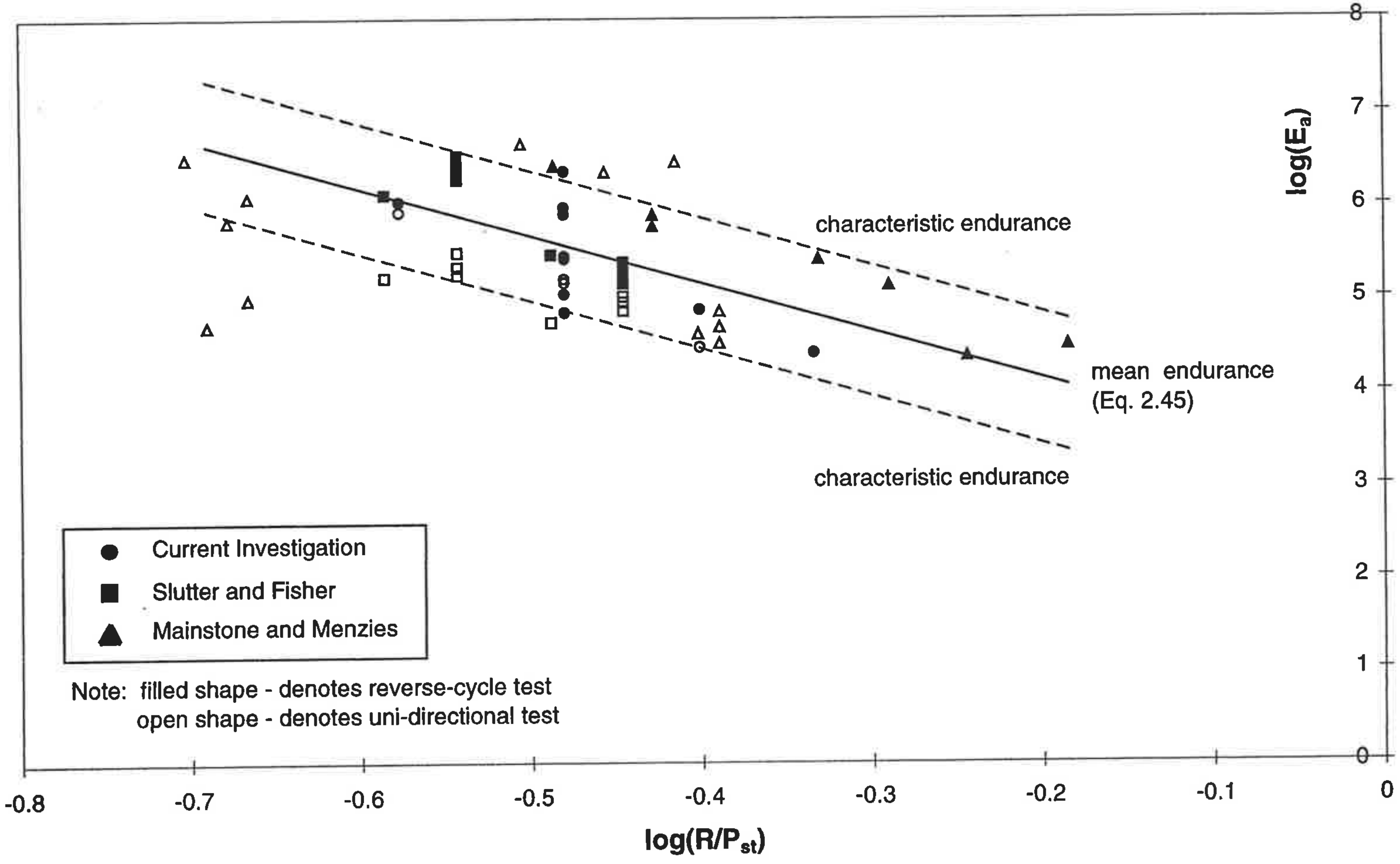

Figure 5.14: Log(E_a) vs log(R/P_{st}).

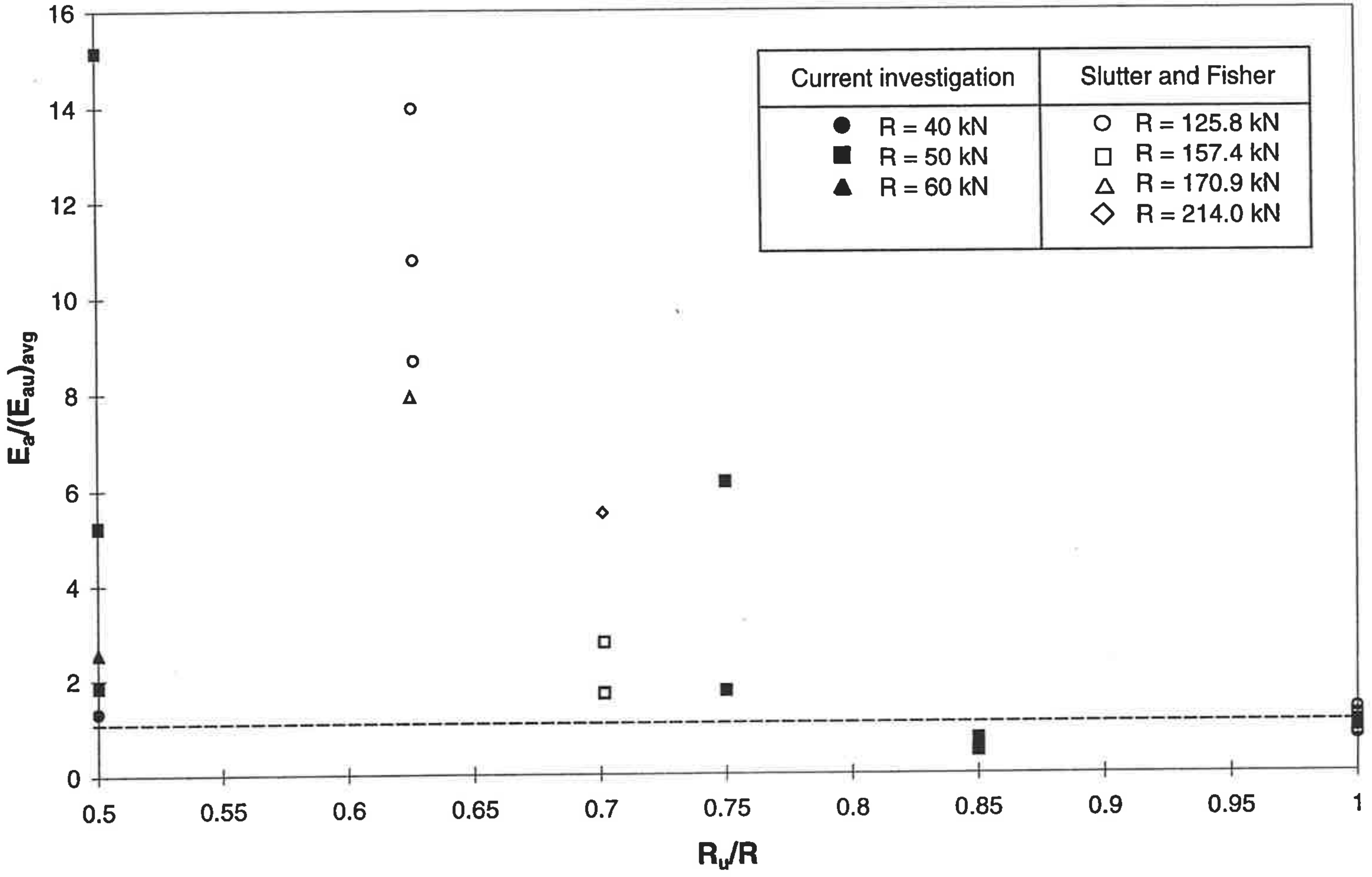

Figure 5.15: Increase in the asymptotic endurance.

Some of the scatter observed during the current series of tests may be attributed to the quality of the welds. Figure 16a shows a photograph of a good weld after fatigue failure has occurred, while Fig. 16b shows a poor weld. There is significant pitting present in the poor welds and there does not appear to be any fatigue cracking associated with failure. Approximately 1/3 of the welds appeared to be poor, however, there does not appear to be any correlation between the number of poor welds in a specimen and the endurance. The only exceptions being specimens F14-P2 and F15-P2, both of which had P_{max}/R = 0.85 and endurances less than the uni-directional case, where all three of the welds in each specimen appeared to be poor.

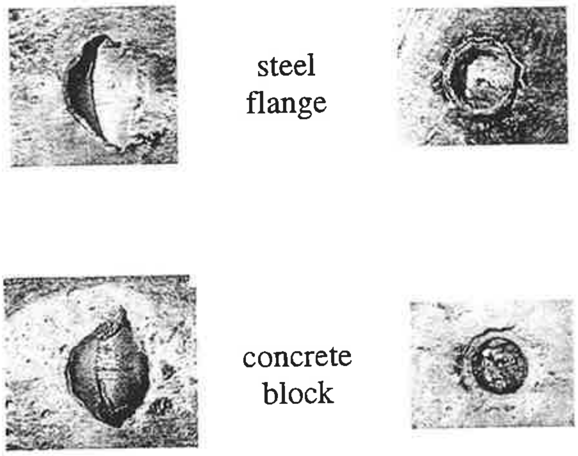

a) good weld b) poor weld

Figure 5.16: Welds after failure.

5.4.2 Slip-N characteristics

The shape of the slip-N curves for all of the tests where sufficient data points were collected is well defined. A bi-linear distribution is used to idealize the slip-N curve as shown in Fig. 5.17. The first part of the distribution represents the gradual increase in slip that occurs at a constant rate of $[ds/dN]_g$. The slip increases gradually over most of the design life, defined by the slip s_g at the onset of cyclic loading and the point (N_r, s_r) which represents the point where the slip begins to increase rapidly as failure approaches. The slip s_g is related to the initial slip s_i, as will be shown later in the section, which can be determined by estimating the initial stiffness of the shear connection in the composite beam. After N_r cycles, the slip increases exponentially, however, this portion of the distribution is also idealized linearly with a constant slope of $[ds/dN]_r$. The constant slope of the rapidly increasing portion of the distribution is defined once again by (N_r,s_r) and the point (N_{exp},s_u) at failure. As it was not possible to record the maximum slip just prior to failure, the ultimate static slip s_u (Eq, 2.41) is used as an approximation.

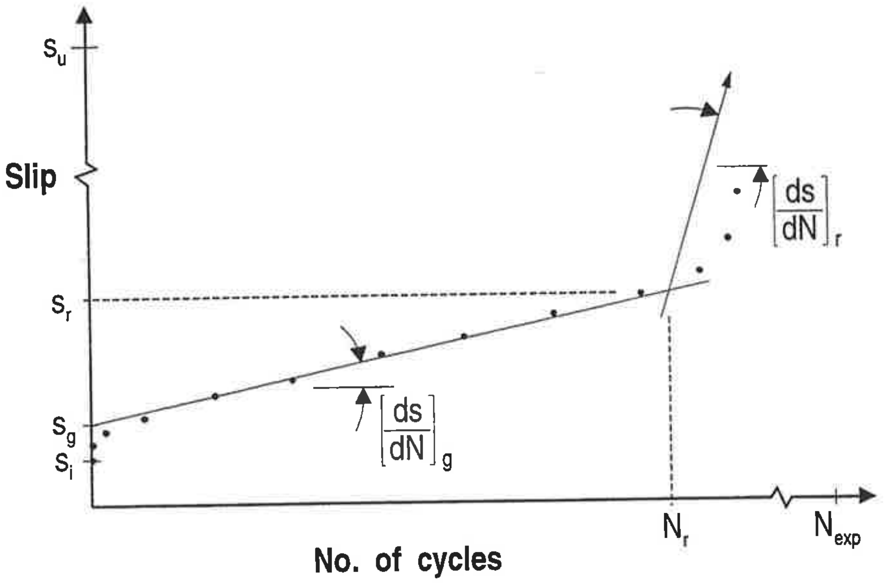

Figure 5.17: Slip-N characteristics.

A summary of the numerical analysis that was performed is given in Table 5.6. The first row in each of the reverse-cycle specimens represents the results from the push branch of the cycle while the second row is that of the pull branch. All of the values were taken or derived from the experimental data with the exception of s_u, which was calculated using Eq. 2.41. It is also noted that the magnitude of N_r is subject to some error as judgement was required in determining when the slip begins to increase rapidly. The cells that have been left blank indicate that insufficient data was available to confidently predict the parameter in question. Where appropriate, the average value of the various parameters is given. In order to determine whether or not there is a noticeable difference between the reverse-cycle and uni-directional cases, the results are given separately and then an overall average is calculated where applicable.

Table 5.6: Analysis of slip-N curves.

Load type	Specimen	s_g/s_i	s_r/s_i	N_r/E_a	N_r/N_{exp}	$[ds/dN]_g$ $(x10^{-6})$	$[ds/dN]_r$ $(x10^{-6})$
Reverse	F2-P1	1.468	2.280	0.570	0.684	0.06	19.3
		1.468	2.280	0.570	0.684	0.06	19.3
	F3-P1	1.080	-	-	-	6	-
		1.418	-	-	-	6	-
	F4-P1	1.602	-	-	-	10	-
		1.392	-	-	-	9	-
	F8-P2	1.678	-	0.358	0.429	-	30.4
		2.250	2.192	0.358	0.429	0.2	30.4
	F9-P2	2.104	-	-	-	0.01	-
		1.940	-	-	-	0.02	-
	F11-P2	-	-	0.662	0.881	-	45.9
		1.197	2.949	0.662	0.881	0.3	45.9
	F12-P2	-	-	-	-	-	-
		2.316	-	-	-	1	-
	F13-P2	1.671	2.014	0.599	0.718	0.02	21.3
		2.140	3.851	0.599	0.718	0.1	21.3
Average		1.695	2.594	0.547	0.678	N/A	N/A
Uni-dir.	F5-P1	1.552	2.957	0.395	0.741	20	870
	F6-P1	1.227	4.544	0.548	0.912	5	468
	F7-P2	1.603	4.569	0.594	0.890	0.6	59
	F10-P2	1.584	3.546	0.514	0.855	4	253
Average		1.492	3.904	0.513	0.850	N/A	N/A
Over-all Average		1.650	3.118	0.530	0.764	N/A	N/A

All of the parameters calculated in Table 5.6 are related to the magnitude of R to varying degrees. This implies that for parameters which are very sensitive to R, an average value, based on all the tests performed, has no meaning. For this reason, no average values are given for the parameters $[ds/dN]_g$ and $[ds/dN]_r$ which are similar to the incremental set relationship given by Eq. 2.43.

Although Eq. 2.43 was derived assuming a linear relationship, it is compared to the $[ds/dN]_g$ results of the current proposal in Fig. 5.18. A linear regression of the experimental data points resulted in the equation given in Fig. 5.18, which is also represented graphically by the solid line, where the factor 6.678 is comparable to the exponent 4.5 of Eq. 2.43.

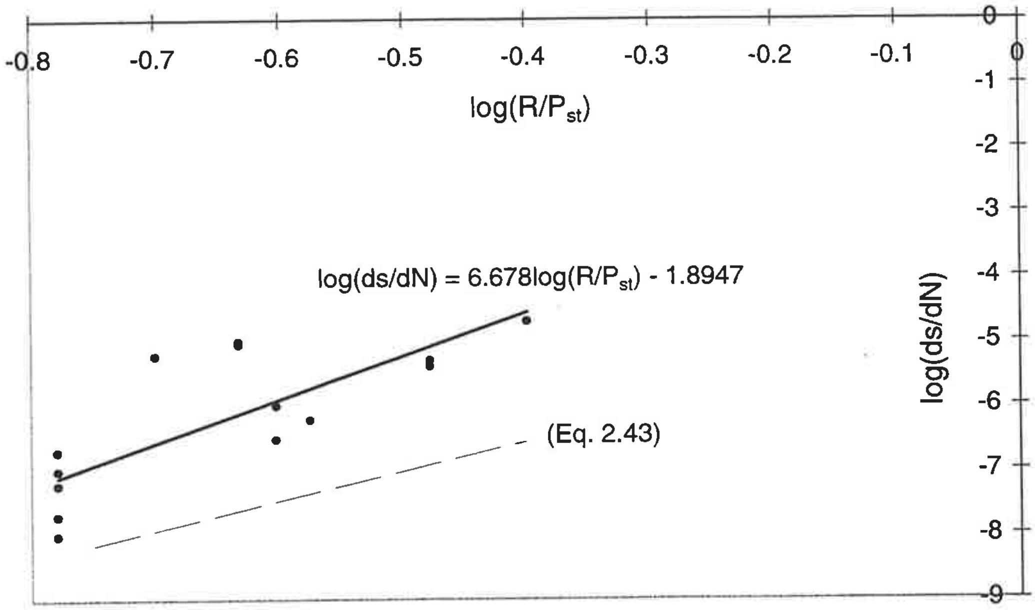

Figure 5.18: Incremental set comparison.

The remaining parameters presented in Table 5.6 do not appear to be as sensitive to R as the corresponding averages for the reverse-cycle and uni-directional tests are reasonably close. It is noted that there are too few test results to suggest a numerical model for the bi-linear slip-N curve proposed, however, the general shape can certainly be described. In particular, attention is drawn to the s_r/s_i parameter where the average value indicates that the slip begins to increase rapidly once the maximum slip is about 3 times the initial slip at the start of the design life. Alternatively, it could also be said that the slip begins to increase rapidly after 50% of the asymptotic endurance is reached as given by the parameter N_r/E_a. This is significant as it can be used to predict the remaining life of a structure.

Chapter 6

Conclusions and Recommendations

6.1 CONCLUSIONS

The following section presents the conclusions the have been made from the original work associated with this research project, which is divided into three main categories; linear-elastic partial-interaction (Chapter 3), non-linear partial-interaction (Chapter 4) and experimental investigation (Chapter 5). Finally, suggestion are given for future directions in the area.

6.1.1 Linear-elastic partial-interaction analyses

Simple procedures have been developed that can be used to more realistically assess the residual strength and residual endurance of simply supported steel-concrete composite bridge beams. The procedures take into account the change in the shear flow forces along the steel-concrete interface and the change in the flexural stresses by allowing for partial-interaction, using simple reduction and multiplication factors. It has been shown that the simple procedures, developed using linear-elastic theory, agree very well with linear finite element partial-interaction computer simulations, validating the approach.

The beneficial effect of partial-interaction is that the reduced shear flow force increases the fatigue life of the shear connectors significantly with respect to current full-interaction procedures. The detrimental effect is that the steel and concrete flexural stresses increase, especially in the vicinity of the steel-concrete interface, due to the location of the partial-interaction focal points. The stresses at the bottom face of the concrete component may be tensile causing accelerated cracking and fatigue problems in the concrete, which are not anticipated with full-interaction analyses. In the steel component, increased compressive stresses near the interface may potentially result in unexpected buckling problems, and the increased tensile stresses near the bottom flange will reduce the fatigue life in the area.

6.1.2 Non-linear partial-interaction analyses

The complex interaction between friction along the steel-concrete interface and the non-linear load-slip behavior of the stud shear connectors was qualitatively described using a simple physical model, which led to the development of a non-linear finite element program suitable for modeling the behavior.

Computer simulations showed that the normal compressive forces acting across the steel-concrete interface are concentrated around the load locations. However, it was observed that the longitudinal shear force resisted by the connectors was reduced relatively uniformly along the span. It followed, therefore, that the total range resisted by the connectors was also reduced, further increasing the anticipated fatigue life of the shear connection with respect to the linear partial-interaction analyses.

A comparison between the computer simulation and an existing mathematical model showed that the predictions of the model are conservative over the length of the beam. The model is a simple hand procedure based on full-interaction results.

6.1.3 Experimental conclusions

Several conclusions can be drawn from the results of the experimental programme and the comparisons made with the results from other researchers.

It is clear that the strength and stiffness of the shear connection is constantly reducing throughout the fatigue life from initial application of cyclic loads. This is evident by the constant increase in slip measured as the number of cycles increased. This information can be useful when trying to establish the remaining fatigue life of existing composite bridges as the rate of increase in slip remains constant until approximately 50% of the asymptotic endurance remains, which would provide adequate warning of failure.

The second significant conclusion that can be made is that the fatigue life of a shear connection subjected to reverse-cycle loading is longer than one subjected to uni-directional cyclic loading of the same total range. As the scatter for both the current investigation and that of the other researchers is quite large, the increase in the endurance can not be quantified. However, the increase in endurance is substantial, ranging from about 1.5 to 15 times the uni-directional asymptotic endurance.

A desirable realization of this study is the fact that current design procedures are conservative as the fatigue endurance of connectors subjected to reverse-cycle loading are predicted using relationships obtained from uni-directional tests.

6.2 RECOMMENDATIONS

It would be beneficial to extend the linear-elastic theory and develop simple reduction and multiplication factors, similar to those given in Chapter 3, for two-span continuous beams. As the partial-interaction focal points are located near the extreme fibers of the cross-section, the effect of partial-interaction is amplified near the steel-concrete interface. This observation may be even more important in the negative moment regions of the beam over the internal supports where the tensile stresses in the top steel flange may be significantly greater than that predicted by full-interaction analyses. It is also suggested that the theory be developed for other practical load conditions, in particular, uniformly distributed loads that could, amongst other things, be used to predict the behavior of beams cast using propped construction.

Quantifying the additional reduction in the range resisted by the shear connectors due to friction and the non-linear load-slip path of the connectors for the simply supported case would be advantageous. The effects of incremental set could also be included and again, the extension of the theory to continuous beams is suggested.

An experimental investigation of two-span continuous beams under cyclic loading would be beneficial to determine the strains in the steel section, especially in the negative moment region, and slip along the interface in order to validate the theoretical models and computer simulations. Additional testing of reverse-cycle push-out specimens would be required to reduce the observed scatter so that the increase in the endurance could be quantified. Placing more emphasis on the welding procedure, resulting in a more consistent set of welds may also reduce the scatter. Additional tests would also be required to quantify the slip-N curve more accurately, which could be used in computer simulations to help predict the remaining strength and endurance of existing structures.

References

Adekola, A.O. (1968). "Partial interaction between elastically connected elements of a composite beam." *Int. J. Solids Structures*, Vol. 4, 1125-1135.

BS5400: Part 10. (1980). *Steel, concrete and composite bridges. Code of practice for fatigue*. British Standards Institution, London.

Cheung, Y.K., and Yeo, M.F. (1979). *A practical introduction to finite element analysis*. Pitman Publishing Limited, London.

CP117: Part 2. (1967). *Composite construction in structural steel and concrete: Beams for bridges*. British Standards Institution, London.

Gattesco, N., and Giuriana, E. (1996). "Experimental study on stud shear connectors subjected to cyclic loading." *Journal of Constructional Steel Research*, 38(1), 1-21.

Gattesco, N., Giuriana, E., and Gubana, A. (1997). "Low-cycle fatigue test on stud shear connectors." *Journal of Structural Engineering*, 123(2), 145-150.

Hallam, M.W. (1976). "The behaviour of stud shear connectors under repeated loading." *Research Report No. R281*, School of Civil Engineering, The University of Sydney.

Hayward, A. (1987). "Cheaper composite bridges." *Composite construction in steel and concrete: Proceedings of an Engineering Foundation Conference*, New England College, Henniker, New Hampshire, June 7-12, 450-459.

Johnson, R.P. (1994). *Composite structures of steel and concrete: Volume 1. Beams, slabs, columns, and frames for buildings*. Blackwell Scientific Publications Ltd., Oxford.

Johnson, R.P., and Oehlers, D.J. (1996). "Integrated design of assessment of shear connections for fatigue and static loading." *The Structural Engineer*, 74(14), 236-240.

Mainstone, R.J., and Menzies, J.B. (1967). "Shear connectors in steel-concrete composite beams for bridges. Part 2: Fatigue tests on beams." *Concrete*, 1(10), 351-358.

Miner, M.A. (1945). "Cumulative damage in fatigue." *J. of Mechanics,* 12(3), 159-164.

Newmark, N.M., Siess, C.P., and Viest, I.M. (1951). "Tests and analysis of composite beams with incomplete interaction." *Proceedings Society for Experimental Stress Analysis*, 9(1), 75-92.

Oehlers, D.J. (1995). "Design and assessment of shear connectors in composite bridge beams." *Journal of Structural Engineering*, 121(2), 214-224.

Oehlers, D.J. (1992). "Residual strength of structural components subjected to cyclic loads." *Journal of Structural Engineering*, 118(10), 2645-2659.

Oehlers, D.J. (1990a). "Deterioration in strength of stud shear connectors in composite bridge beams." *Journal of Structural Engineering*, 116(12), 3417-3431.

Oehlers, D.J. (1990b). "Methods of estimating the fatigue endurances of stud shear connections." *International Association of Bridge and Structural Engineers*, Proceedings P-145/90, 65-84.

Oehlers, D.J. (1990c). "Estimating the residual strength of stud shear connections in existing composite bridge beams." *Civil Engineering Transactions* (I.E.Aust.), CE32(2), 61-65.

Oehlers, D.J., and Bradford, M.A. (1999). *Elementary behaviour of composite steel and concrete structural members.* Butterworth-Heinemann, Oxford.

Oehlers, D.J., and Bradford, M.A. (1995). *Composite steel and concrete structural members: Fundamental behaviour.* Pergamon Press, Elesvier Science Ltd., Oxford.

Oehlers, D.J., and Carroll, M.A. (1987). "Simulation of composite beams subjected to traffic loads." *Composite construction in steel and concrete: Proceedings of an Engineering Foundation Conference*, New England College, Henniker, New Hampshire, June 7-12, 450-459.

Oehlers, D.J., and Coughlan, C.G. (1986). "The shear stiffness of stud shear connections in composite beams." *Journal of Constructional Steel Research*, 6, 273-284.

Oehlers, D.J., and Foley, L. (1985). "The fatigue strength of stud shear connections in composite beams." *Proceedings of the Institution of Civil Engineers*, Part 2, 79, 349-364.

Oehlers, D.J., Ghosh, A., and Wahab, M. (1995). "Residual strength approach to fatigue design and analysis." *Journal of Structural Engineering*, 121(9), 1266-1271.

Oehlers, D.J., and Johnson, R.P. (1987). "The strength of stud shear connections in composite beams." *The Structural Engineer*, 65B(2), 44-48.

Oehlers, D.J., and Singleton, W.M. (1986). "The simulation of simply supported composite beams tested under fatigue loads." *Proceedings of the Institution of Civil Engineers*, Part 2, 81, 647-657.

Ogle, M.H. (1980). "The new fatigue loading for highway bridges." *Conference on the new code for the design of steel bridges*, Paper 23 Session 12, Cardiff, September, 433-453.

Ollgaard, J.G., Slutter, R.G, and Fisher, J.W. (1971). "Shear strength of stud connectors in lightweight and normal-weight concrete." *AISC Engineering Journal*, 8, 55-64.

Robinson, H., and Naraine, K.S. (1987). "Slip and uplift effects in composite beams." *Composite construction in steel and concrete: Proceedings of an Engineering Foundation conference*, New England College, Henniker, New Hampshire, June 7-12, 487-497.

Roderick, J.W., and Ansourian, P. (1976). "Repeated loading of composite beams." *Civil Engineering Transactions* (I.E.Aust.), CE18(2), 109-116.

Sinclair, G.M. (1956). "Fatigue strength of ¾-in. welded stud shear connectors." *ACI Journal*, 27, 1442-1445.

Singleton, W.M. (1985). *The transfer of shear in simply supported composite beams subjected to fatigue loads.* Thesis submitted to the National University of Ireland for the degree of Master of Engineering Science.

Slutter, R.G., and Fisher, J.W. (1966). "Fatigue strength of shear connectors." *Highway Research Record* (HRB), 104, 65-88.

Thurlimann, B. (1959). “Fatigue and static strength of stud shear connectors.” *ACI Journal*, 30, 1287-1302.

Toprac, A.A. (1965). “Fatigue strength of 3/4-inch stud shear connectors.” *Highway Research Record* (HRB), 103, 53-77.

Viest, I.M. (1960). “Review of research on composite steel-concrete beams.” *Journal of the Structural Division* (ASCE), 86(ST6), 1-21.

Yazdani, N. and Albrecht, P. (1987). “Risk analysis of fatigue failure of highway steel bridges.” *Journal of Structural Engineering*, 113(3), 483-500.

Appendix A

Load-slip curves

The following Appendix shows the load-slip curves of all of the specimens tested as part of the experimental investigation.

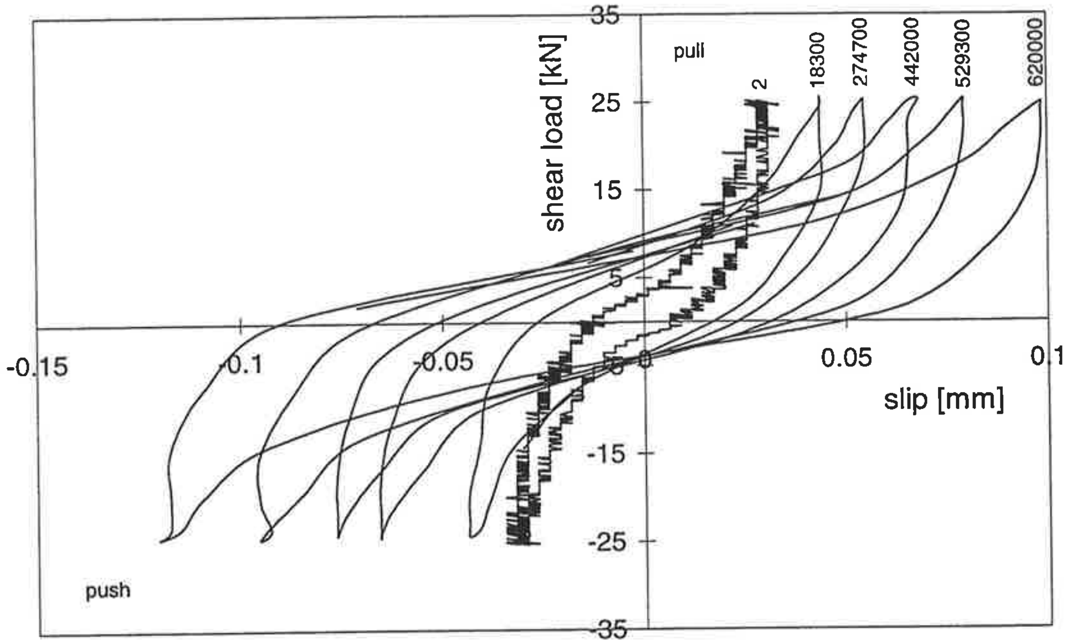

Figure A1: F2-P1

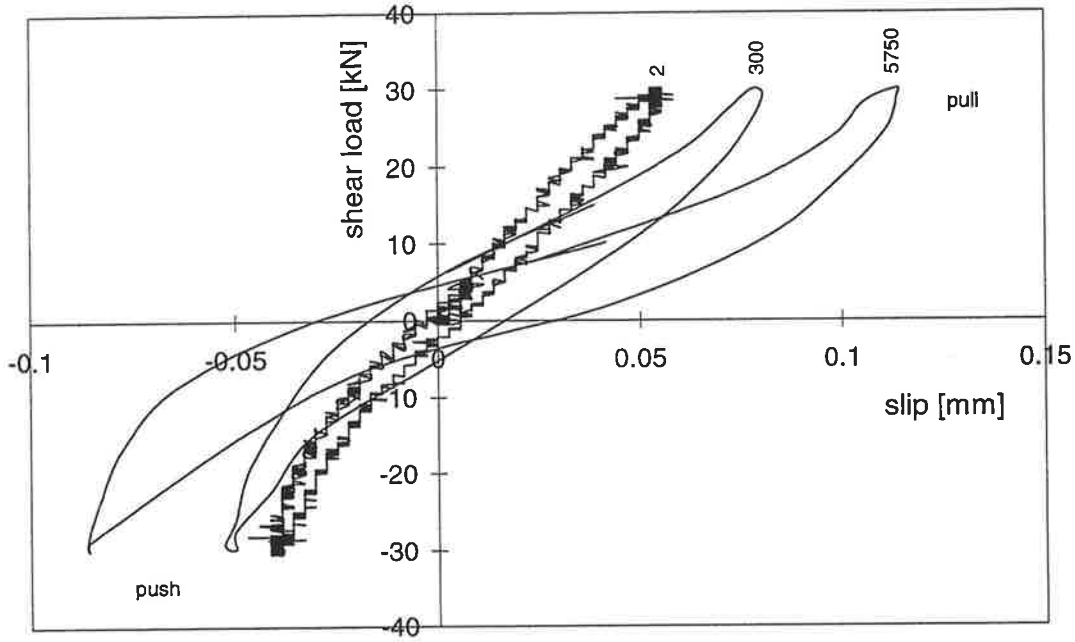

Figure A2: F3-P1

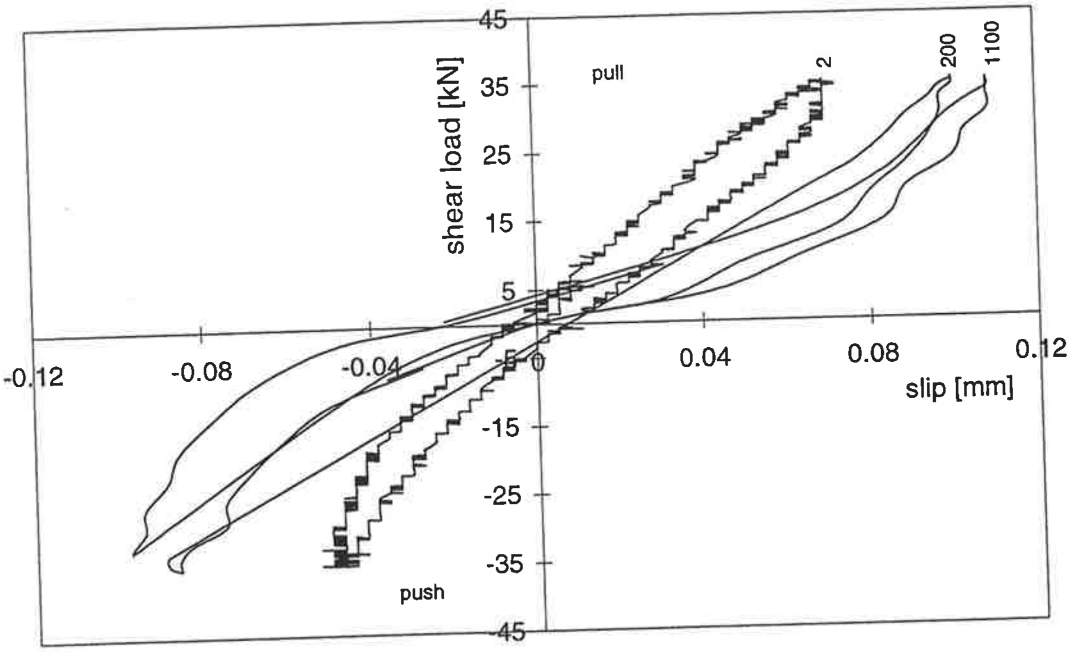

Figure A3: F4-P1

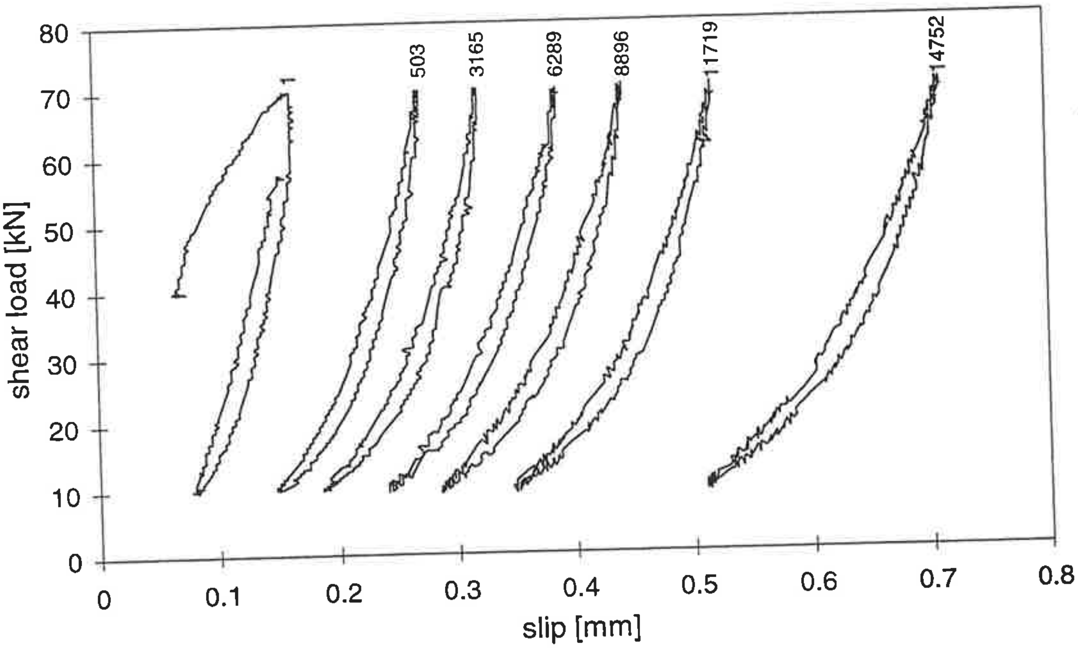

Figure A4: F5-P1

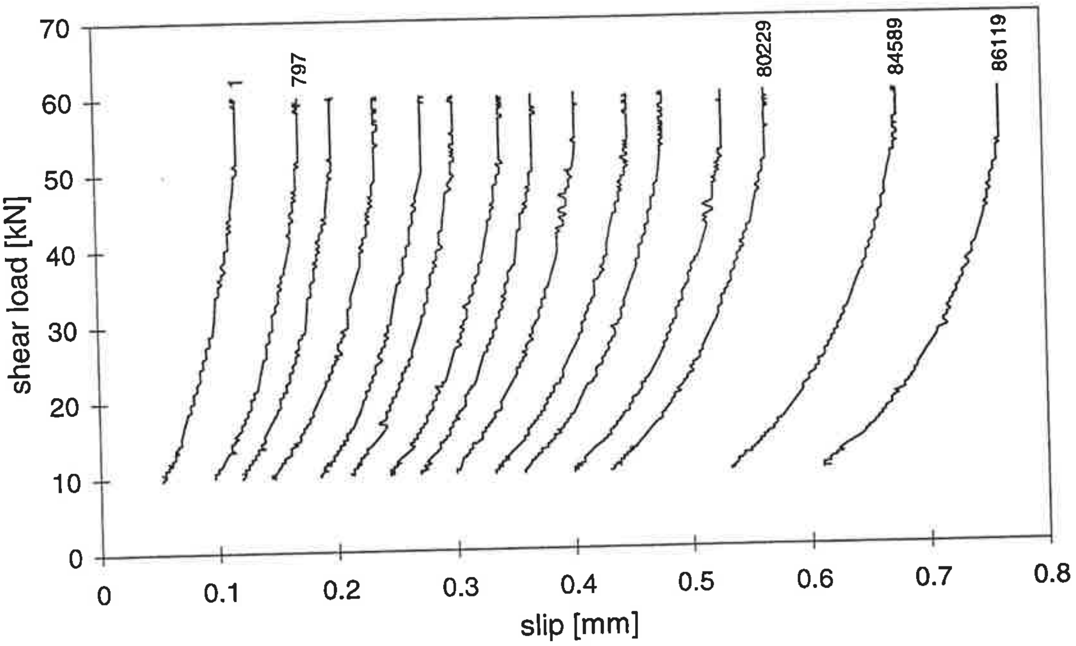

Figure A5: F6-P1

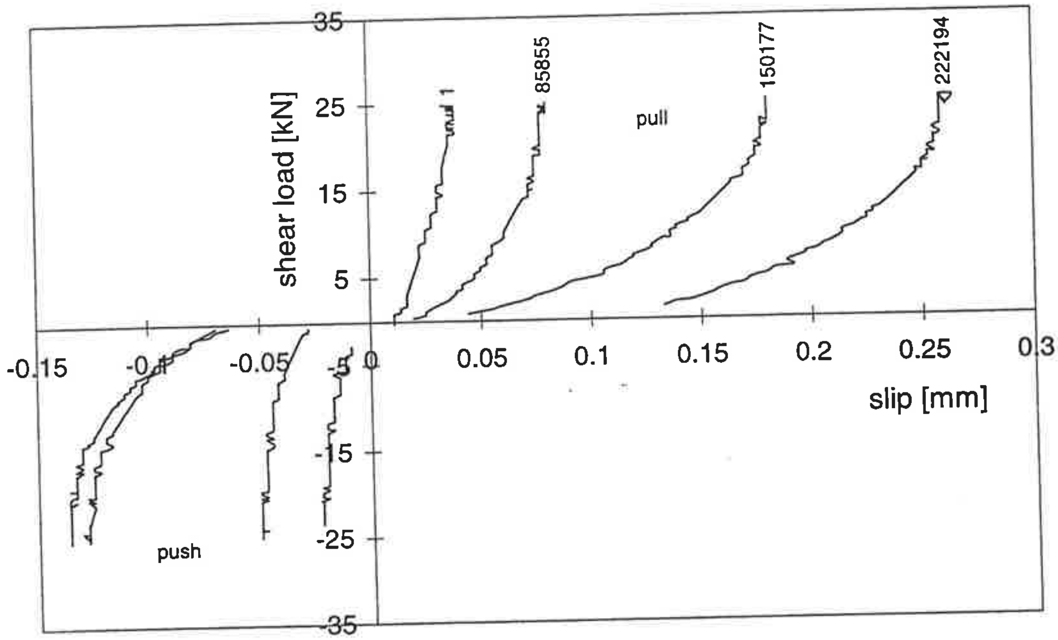

Figure A6: F8-P2

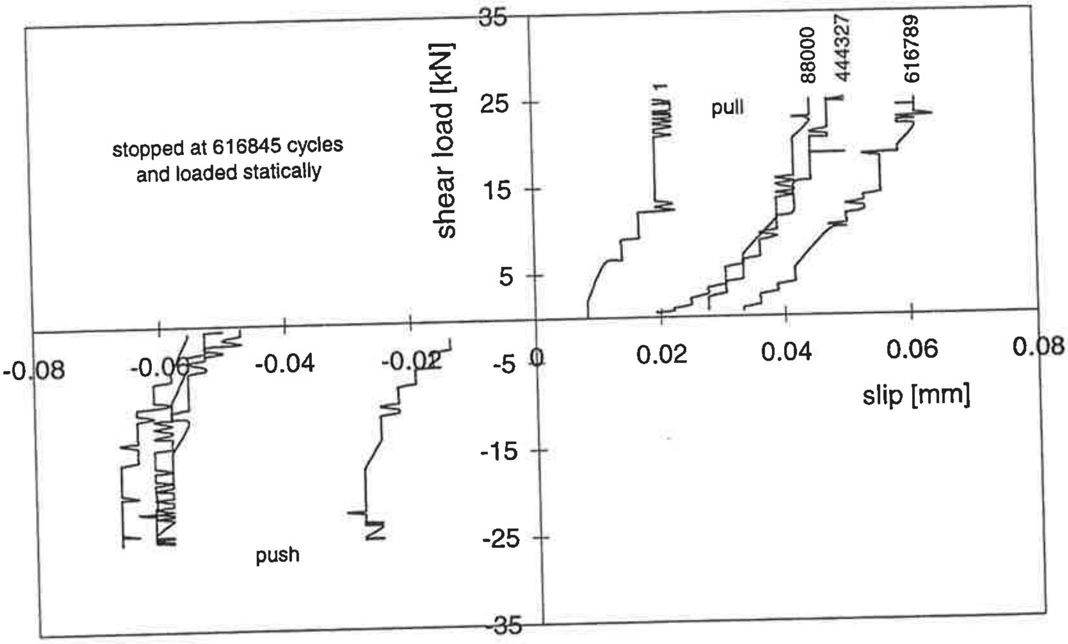

Figure A7: F9-P2

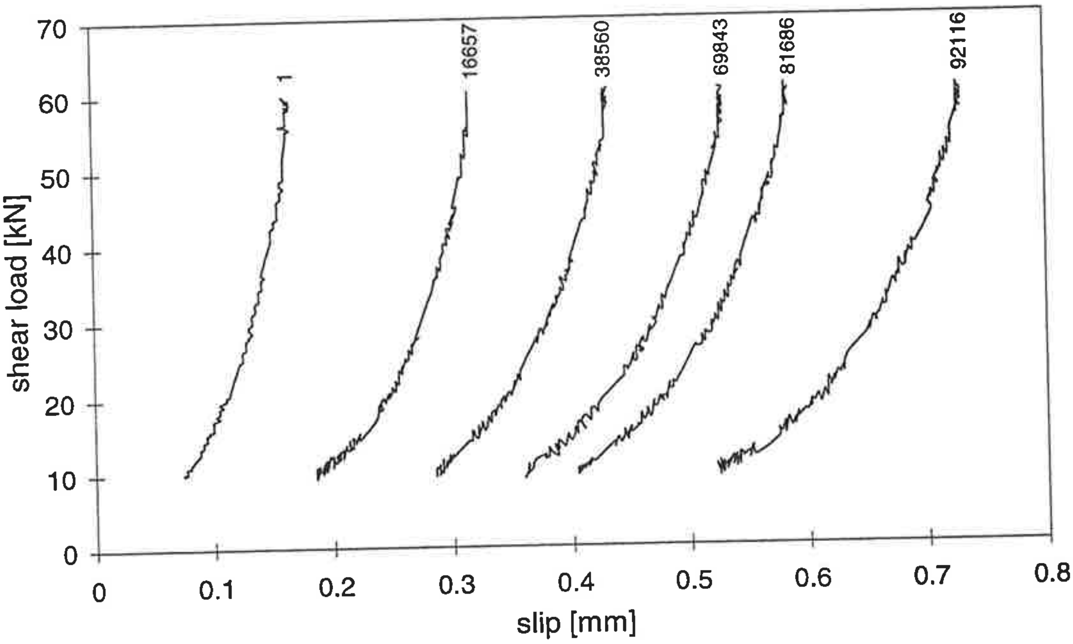

Figure A8: F10-P2

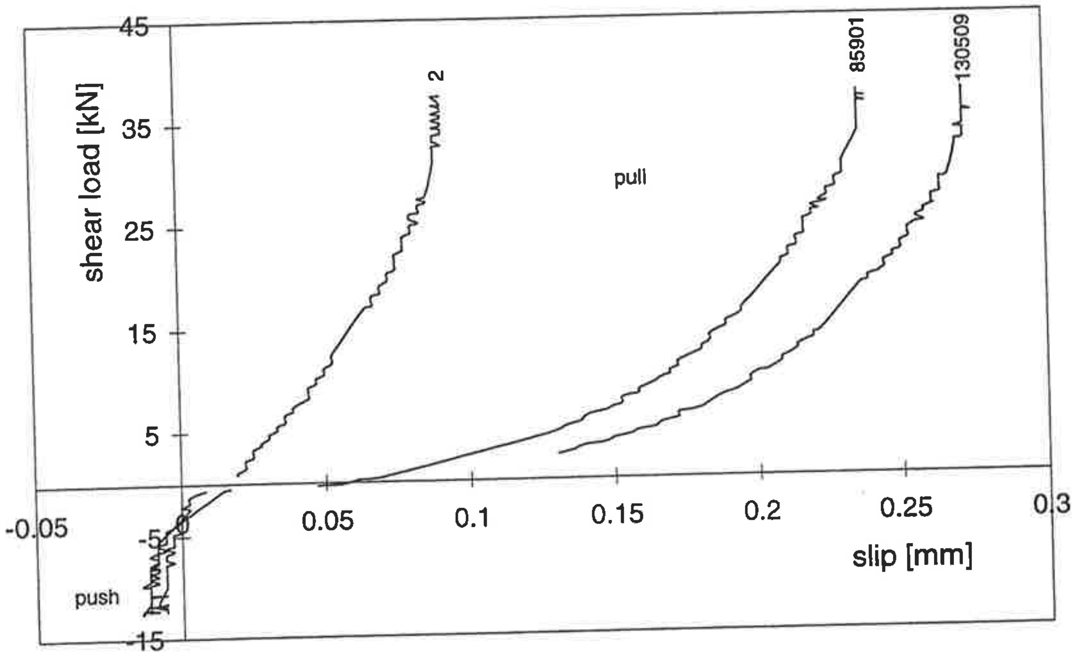

Figure A9: F12-P2

Appendix B

Slip-N curves

The following Appendix shows the slip-N curves of all of the specimens tested as part of the experimental investigation.

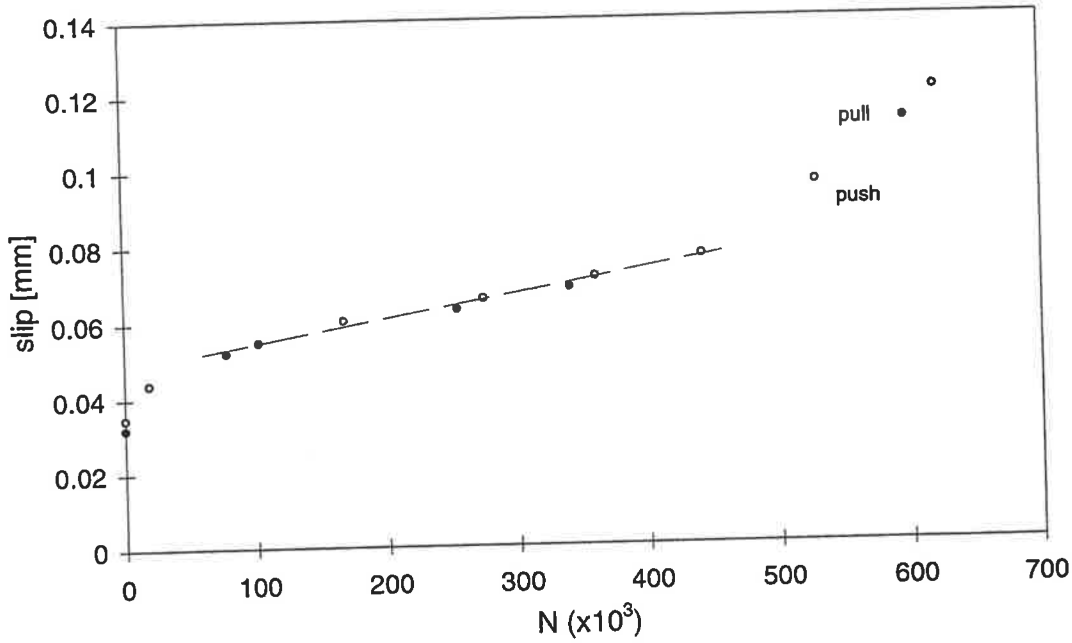

Figure B1: F2-P1

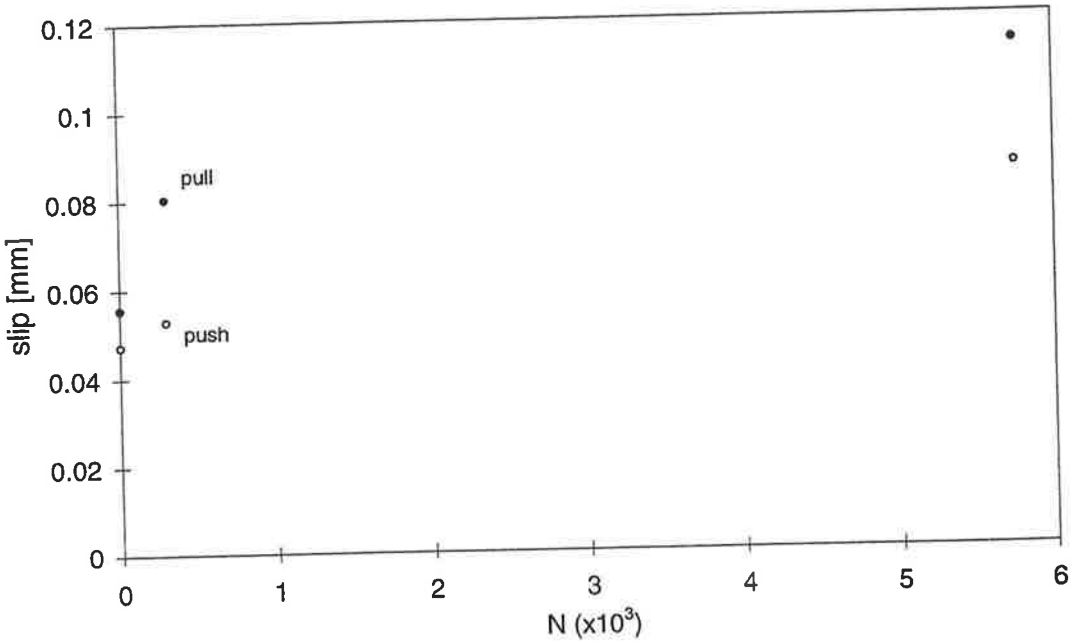

Figure B2: F3-P1

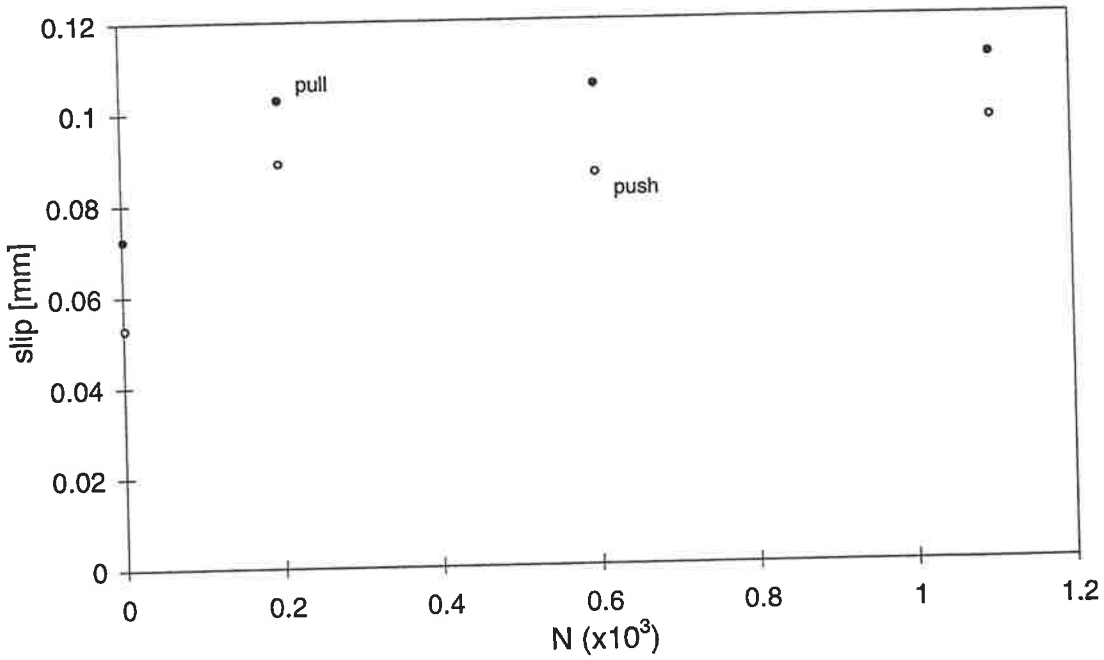

Figure B3: F4-P1

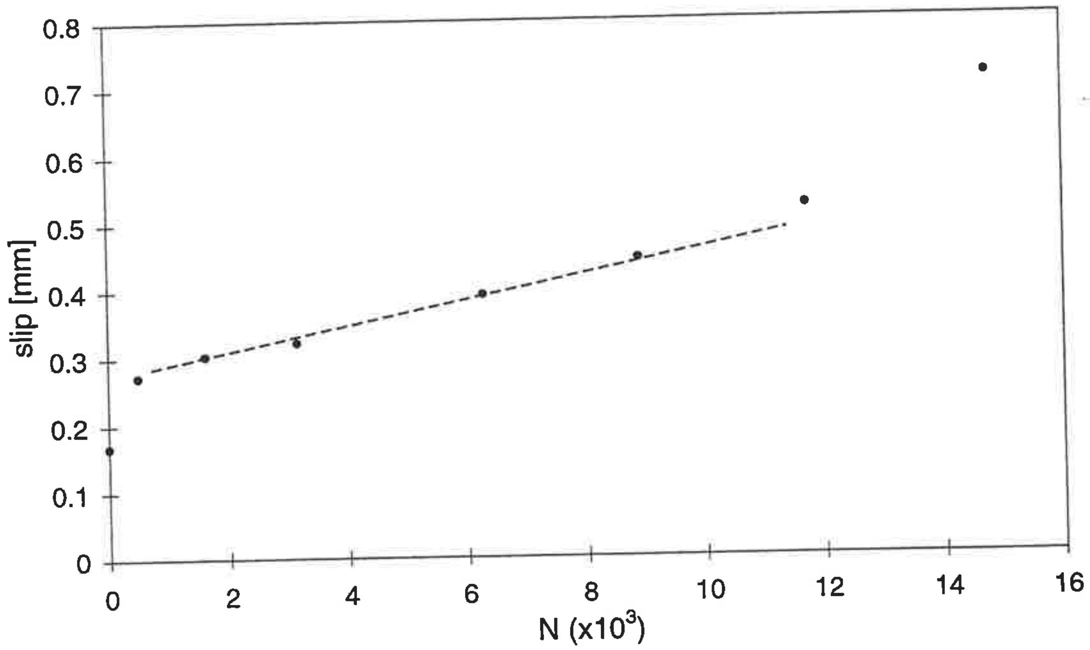

Figure B4: F5-P1

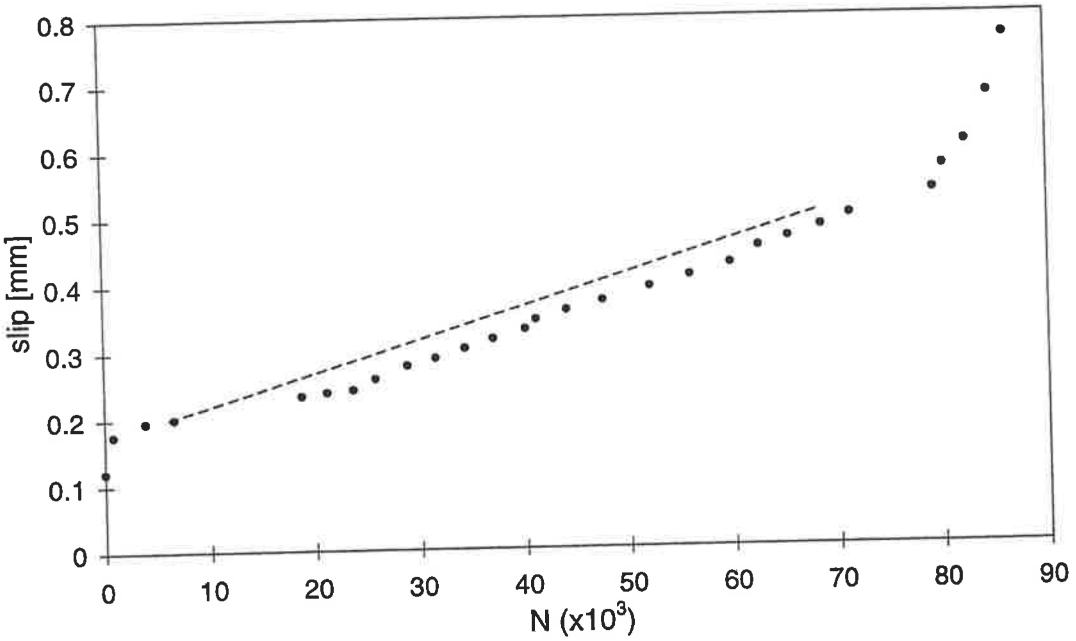

Figure B5: F6-P1

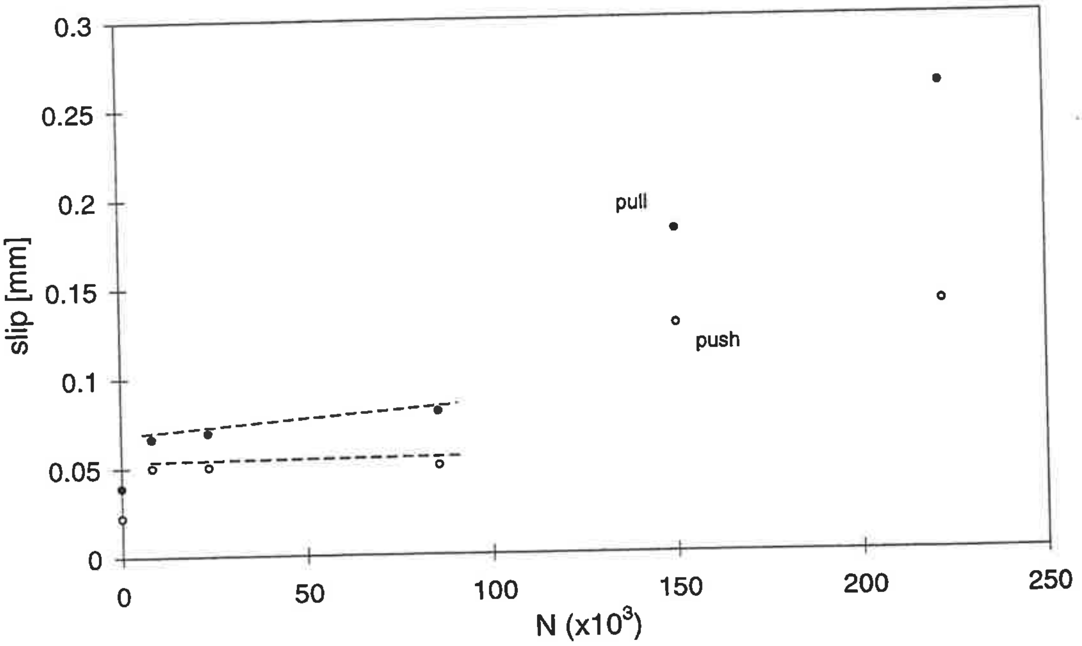

Figure B6: F8-P2

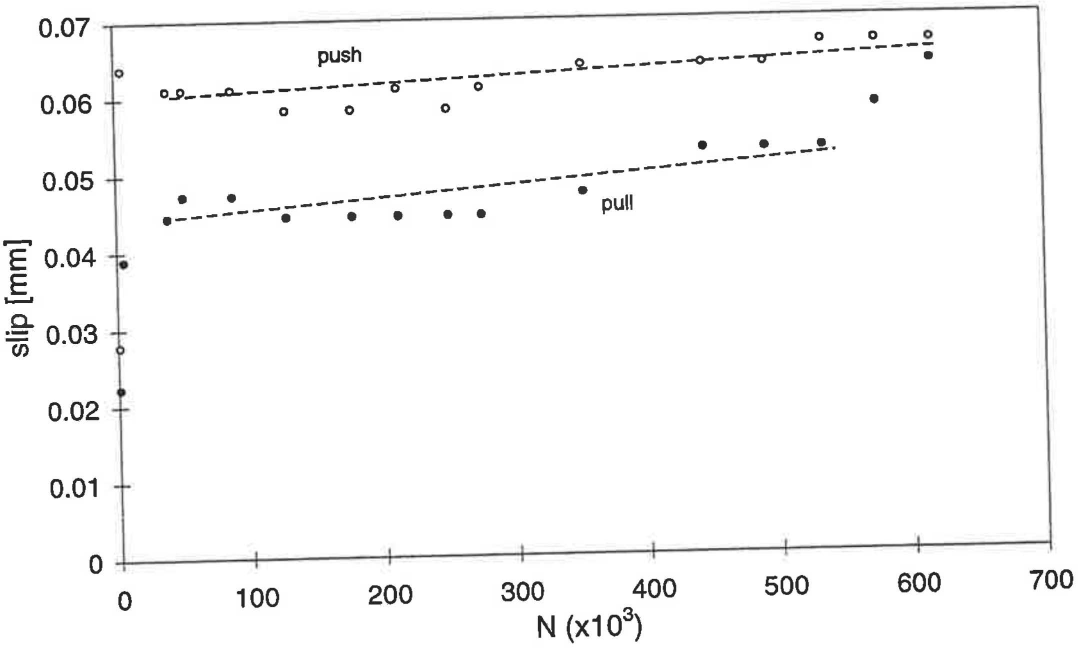

Figure B7: F9-P2

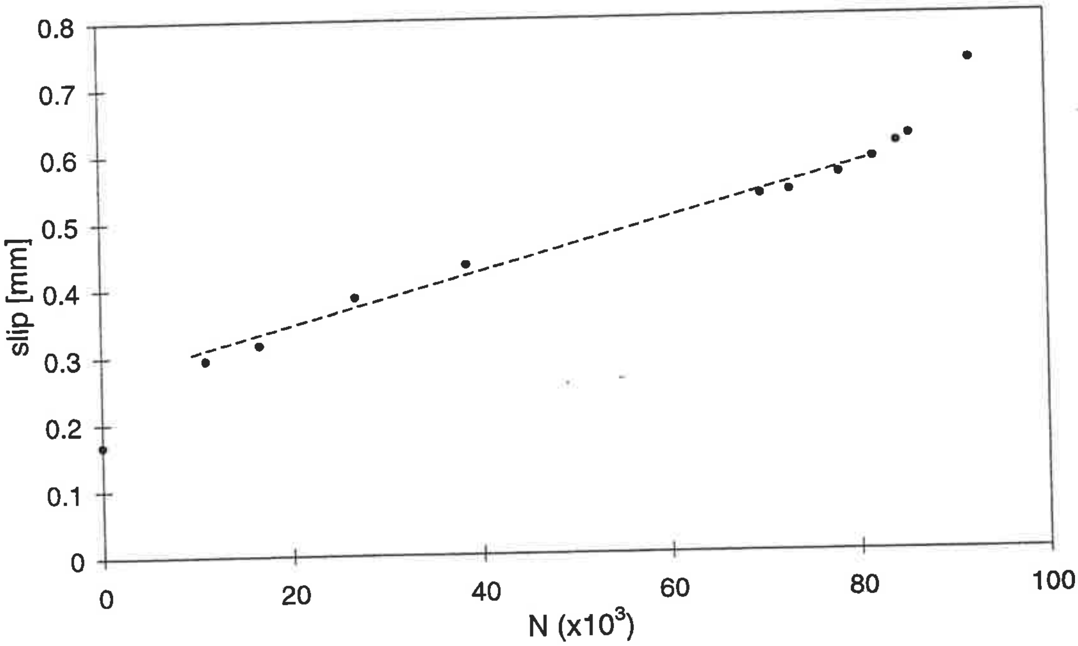

Figure B8: F10-P2

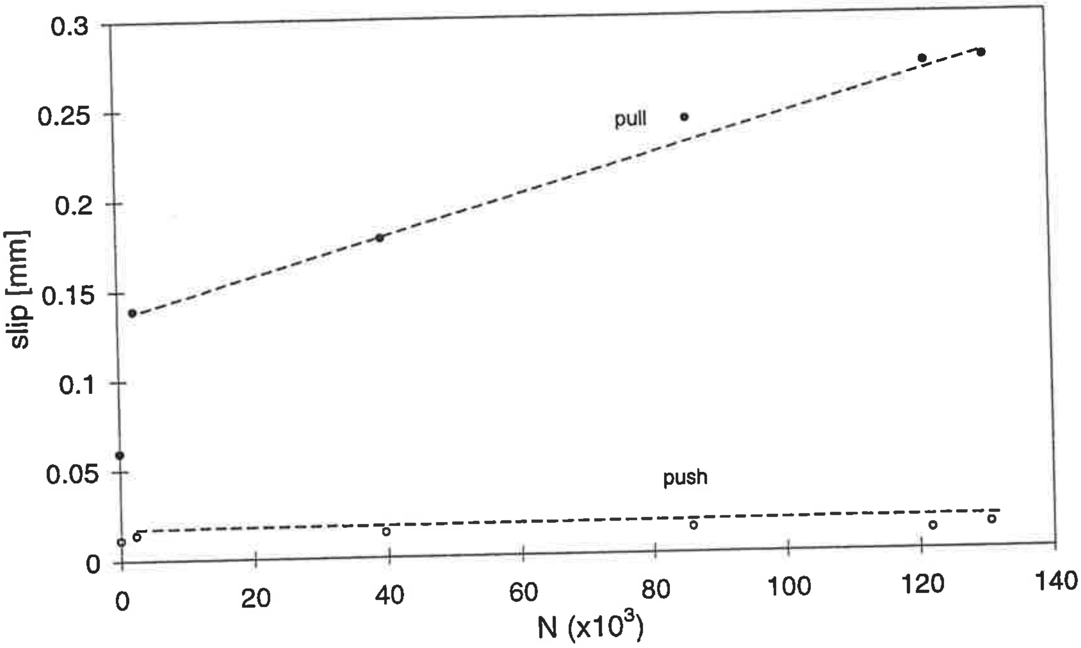

Figure B9: F12-P2